Synthesis and Self-Assembly of Quinoidal Molecules at the Liquid-Solid Interface – An STM Investigation

Yuan Fang

A Thesis

in

The Department

of

Chemistry and Biochemistry

Presented in Partial Fulfillment of the Requirements

for the Degree of Master Science (Chemistry) at

Concordia University

Montréal, Québec, Canada

September 2013

CONCORDIA UNIVERSITY

School of Graduate Studies

This is to certify that the thesis prepared

By: Yuan Fang

Entitled: Synthesis and Self-assembly of Quinoidal Molecules at the Liquid-Solid Interface

- An STM Investigation

and submitted in partial fulfillment of the requirements for the degree of

Master of Science (Chemistry)

complies with the regulations of the University and meets the accepted standards with respect to originality and quality.

Signed by the final examining committee:

Guillaume Lamoureux_____ Chair

Christine DeWolf_____ Examiner

Xavier Ottenwaelder_____ Examiner

Louis Cuccia_____ Supervisor

Approved by

_____
Chair of Department or Graduate Program Director

Sep 19 2013

_____
Dean of Faculty

ABSTRACT

An exploration of the 2D supramolecular self-assembly of benzoquinone derivatives at the liquid-solid interface using scanning tunneling microscopy (STM) is presented. In the 30 years since its discovery, STM has emerged as one of the most powerful and unique surface characterization techniques. We have applied a versatile transamination reaction of 2,4-diaminoresorcinol to synthesize zwitterionic *meta*-diaminobenzoquinones (**Cn*m***) with the ability to form robust charge-assisted hydrogen bonded arrays. Charge-assisted hydrogen bonding, where traditional hydrogen bonding is accompanied by Coulombic interactions, leads to exceptionally strong and inherently flexible interactions between oppositely charged or zwitterionic components. The typical energy of a NH···O charge-assisted hydrogen bond is 4 times as strong as that of normal hydrogen bond. We also have easy access to *para*-aminobenzoquinones (**Cn*p***) which have the ability to form a conventional hydrogen-bond network. Formation and self-assembly of the 2:1 metal complex of **C18*m*** with Ni(II), **(C18*m*)$_2$Ni**, was investigated and conglomerate chiral domains were observed in contrast to the pseudoracemic domains of **C18*m***. In this thesis, synthesis of the above mentioned compounds under both solvent and solvent-free conditions are described. In addition, factors governing morphology, chirality and multilayer formation are discussed, presenting an important foundation for understanding the properties of a large family of related molecules with interesting potential in supramolecular design. Controlling well-defined 2D structures provides important insight into crystallization and is an essential step in the rational design of solid-state materials for interfacial applications.

ACKNOWNOLEDGEMENTS

First and foremost I would like to thank my supervisor, Prof. Louis A. Cuccia, for giving me the opportunity to work in his group, for providing knowledge in a wide variety of interdisciplinary and connected research areas. He has provided me with exceptional intellectual freedom and scientific guidance. He is a most kind and stimulating professor who has transformed me from learning chemistry to loving chemistry. Recalling one of many jokes he said in the lab, "I cannot adopt you as my child," I wish he could, because he cares for us like we were his children and he has made our lab a happy family.

I am also grateful to the different research groups that have contributed to the interdisciplinary work presented in this thesis. In particular, I would to thank Prof. Steven De Feyter (Catholic University of Louvain, Belgium), Prof. Tomislav Friščić (McGill University), Prof. Scott Bohle (McGill University), Prof. Garry Hanan (Université de Montréal), Prof. Olivier Siri (Université de la Méditérranée, France), Prof. Ulrich Ziener (Universität Ulm, Germany), Prof. Todd C. Sutherland (University of Calgary), and all the co-workers in their groups, especially: Mihaela Cibian, Neal Macdonald, Dr. Elke Ghijsens, Dr. Kunal Mali, Dr. Shenlong Lee and Dr. Oleksandr Ivasenko.

Thanks to my committee members, Prof. Christine DeWolf and Prof. Xavier Ottenwaelder, for reading and providing valuable remarks and input to my thesis and research.

Special thanks go to my mentor Dr. Oleksandr Ivasenko (McGill University and Catholic University of Louvain, Belgium) who has guided me into the wonderful world of

scanning tunneling microscopy. He has become my lighthouse, breaking the darkness, guiding me, and directing my passage.

I would like to thank Dr. Rolf Schmidt and Petr Fiurasek for instrument training, and for providing research support. Furthermore I want to thank all members who joined Louis' supramolecular group during the period of my stay at Concordia University: Monica, Carolin, Maria, Eskedar, Phuong, Iris, William, Allan, Cheng, Dylan, Jummy, Nadime, Elliot, Leinjo, Danaly, Dr. Salomon, Sean, Soyoung, Michael, Dr. Simon, Parsram, and Lily. Thanks for the wonderful time we spent together, for your advice, for all knowledge that we exchanged, friendship and fun activities!

Last but not least, I want especially thank my parents who continuously supply me with the most priceless treasure, *love*. I am forever grateful to them.

Table of Contents

List of Figures

List of Tables

List of Equations

List of abbreviations

AFM:	Atomic Force Microscopy
d:	Tip-to-sample spacing
DFT:	Density Functional Theory
E_F:	Fermi level
HOMO:	Highest Occupied Molecular Orbital
HOPG:	Highly Ordered Pyrolytic Graphite
I:	Current
I_t:	Tunneling current
LDOS:	Local Density of States
LUMO:	Lowest Unoccupied Molecular Orbital
STM:	Scanning tunneling microscopy
SPM:	Scanning probe microscopy
TCB:	1,2,4-trichlorobenzene
UHV:	Ultra High Vacuum
V :	Voltage
V_b:	Bias voltage
ϕ:	Work function

Chapter 1. Introduction

1.1. Goal

The ultimate motivation of this research project is to explore the supramolecular self-assembly of amino-substituted quinone derivatives. Quinonoid compounds are ubiquitous in nature. Characteristics such as their charge-transfer properties and biological applications in medicinal chemistry have prompted us to obtain deeper insight into these compounds.

In this thesis we approach this subject *via* two research directions. On the one hand, we report a novel route to synthesize quinonoid compounds in a green-chemistry manner allowing for their synthesis in an environmentally-friendly fashion. In particular, various solvent-free reaction conditions were attempted in the synthesis of diaminobenzoquinones and a diaminobenzoquinone metal complex. On the other hand, our principal goal is to study the self-assembly behavior of quinonoid compounds on graphite using scanning tunneling microscopy (STM) with sub-molecular level resolution. We discuss how the functional groups of the quinonoid molecules influence their self-assembly patterns. The information obtained in this research should not only be beneficial in understanding the early stages of molecular crystal growth, but may have important implications in molecular-based devices and their potential applications.

The breakdown of this thesis is as follows:

Chapter 1 includes: (*i*) a general introduction to scanning tunneling miscroscopy, the main technique used for studying aminoquinone molecular self-assembly described in Chapters 2 and 3; this includes sections on hydrogen bonding, multilayer formation in STM and moiré patterns in STM and (*ii*) a general introduction to mechanochemistry as a prelude to Chapter 4.

Chapter 2 describes charge-assisted hydrogen bond-directed self-assembly of an amphiphilic zwitterionic benzoquinonemonoimine at the liquid-solid interface using STM.

This is a published manuscript authored by Y. Fang, P. Nguyen, O. Ivasenko, M.P. Aviles, E. Kebede, M.S. Askari, X. Ottenwaelder, U. Ziener, O. Siri, and L.A. Cuccia, (*Chem. Commun.,* **2011**, *47*, 11255-11257). The contributions of the co-authors are as follows: S. Ivasenko played an essential role in interpreting STM results. E. Kebede, synthesized some of the *p*-benzoquinonemonoimine (**C18*m***) used in this STM investigation. P. Nguyen, and M.P. Aviles carried out some of the preliminary STM imaging at Concordia University. Some preliminary STM imaging was carried out at the University of Ulm with our collaborator U. Ziener, who also contributed to STM interpretation. M.S. Askari, X and Ottenwaelder collected the x-ray diffraction data and solved/refined the x-ray structure of the *p*-benzoquinonemonoimine that was used to compare with our STM-derived 2D packing models. O. Siri provided us with our first sample of **C18*m*** and helped with the preparation of the manuscript.

Chapter 3 describes the influence of alkyl chain length, hydrogen bonding, constitutional geometry and metal complexation on the 2D and 3D self-assembly of aminoquinone derivatives. This is a manuscript to be submitted to *Langmuir* in October 2013 and is authored by Y. Fang, O. Ivasenko, S. Lee, M. Cibian, G.S. Hanan, O. Siri, and L.A. Cuccia. The contributions of the co-authors are as follows: O. Ivasenko and S. Lee played an essential role in interpreting STM results. M. Cibian and G.S. Hanan played instrumental roles in the synthesis and characterization of the **(C18*m*)$_2$Ni** complex. O. Siri provided us with our first sample of the *p*-benzoquinonemonoimine used in this STM investigation and helped with the preparation of the manuscript.

Chapter 4 describes mechanochemistry and solvent-free methods for the synthesis of aminobenzoquinones and an aminobenzoquinone metal complex. This is a manuscript to be submitted to *Green Chemistry* in October 2013 and is authored by Y. Fang, N.

Salamé, S. Woo, T. Friščić and L.A. Cuccia. The contributions of the co-authors are as follows: N. Salamé aided in the synthesis and characterization of C18*m* and C18*p*, T. Friščić provided essential guidance and suggestions regarding mechanochemistry and helped in the preparation of the manuscript and S. Woo helped with product characterization and with the preparation of the manuscript.

Chapter 5 provides a general summary of the results and a brief conclusion.

1.2. Scanning Tunneling Microscopy (STM)

1.2.1. Introduction

Nanoscience or nanotechnology is the study of matter near or smaller than the nanometer range.[1] This field has attracted a great deal of attention, due to the desire to understand, discover and develop novel properties when things reach the nanoscale, and to eventually apply this science towards novel nanodevices (*e.g.* to replace microelectronics).[2–5] The recent advances in nanotechnology are mainly thanks to the development of scanning probe microscopy (SPM; STM in 1981[6] & AFM in 1986[7] that allows measuring and manipulating molecules or atoms down to the sub-ångström scale.[8] Among the SPM techniques, the pioneering Scanning Tunneling Microscopy (STM) has contributed to many scientific discoveries at the nanoscale and has inspired scientists to develop other scanning probe microscopy techniques including AFM.[9,10] The two scientists who invented the scanning tunneling microscope, Binnig and Rohrer, were honored with the Nobel Prize in Physics in 1986, five years after their seminal research. The Nobel committee said that this discovery opened up, "entirely new fields for the study of the structure of matter."[11]

STM is a microscopy technique, which implies that it can magnify objects to a level that can be seen by the naked eye. However, in the case of STM, it can do much more than this. For example, it can also manipulate atoms on solid surfaces. For example, in 1989 Eigler *et al*. 'wrote' the logo of their research center (IBM) using STM on a single crystal nickel surface,[12] where the 'ink' was 35 individual xenon atoms (**Figure**

1a). STM has revolutionized people's thoughts about atoms and molecules and, for the first time, has allowed them to manipulate materials of their own design at the atomic level. With the ability to position atoms, researchers went one step further; in 1993, Eigler *et al*. positioned 48 iron atoms into a circular ring on a copper (111) surface such that the resulting iron ring confined some copper surface electrons and forced them into quantum states to form standing-waves visualized as ripples within the ring (**Figure 1b**).[13] This STM image shows the dual nature of the electrons where, "[t]he individual iron bumps show the particle-like nature," and, "the wave pattern in the interior shows the wavelike nature."[13]

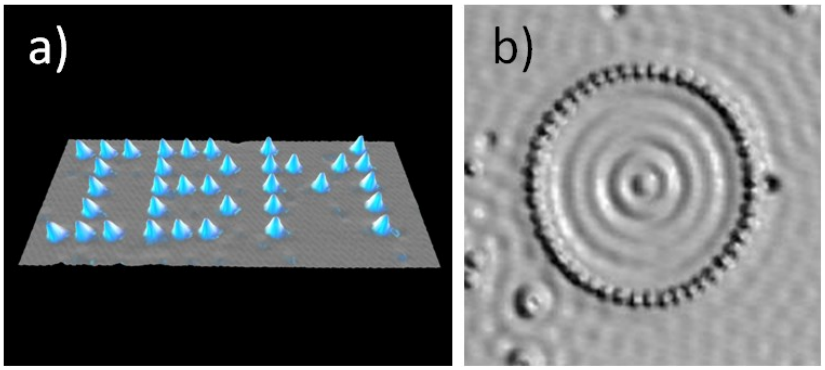

Figure 1. a) Xenon atoms on a nickel (110) surface forming the letters 'IBM'.[12] (b) 48 iron atoms forming a 'quantum corral' on a copper (111) surface.[13]

1.2.2. Basic principles of Scanning Tunneling Microscopy

Scanning tunneling microscopy takes advantage of the phenomenon of quantum tunneling which was known since the early days of quantum mechanics.[14] It is widely used to image surfaces (with or without absorbates) and to even probe single molecules with atomic resolution. Basically, an atomically sharp metallic tip is brought very close to a conductive or semiconductive surface, and a tunneling current can jump either from the tip to the surface or from the surface to the tip depending on the bias voltage applied through a vacuum or a solvent barrier (**Figure 2**).

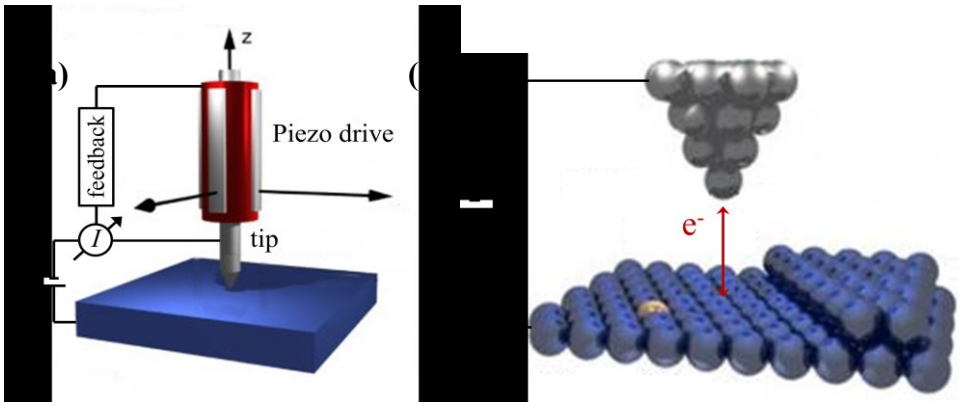

Figure 2. (a & b) Schematic views of the scanning tunneling microscope. A bias voltage, *V*, is applied between the tip and a conducting surface. The tip is brought so close to the surface that a current can tunnel either from the tip to the surface ($V > 0$) or from the surface to the tip ($V < 0$). The tip can scan in all three directions using a piezo drive. A feedback loop system constantly adjusts the tip height or current to reach or to maintain the preset current and bias voltage.[14,15]

The three interdependent parameters of STM: (*i*) tunneling current, *I*, (*ii*) bias voltage, *V*, and the (*iii*) electrode spacing, *d*, are typically 0.01 to 10 nA, -2 to 2V, and 5 to 10 Å, respectively.[1] The major technological breakthrough for the advancement of STM was the development of piezoelectric transducers, which can reach picometer resolution in the *z*-direction.[14] The STM tip functions as a local probe and is scanned over the surface using a piezo scanner. The tip can move in all three directions (*x*, *y* and *z)* and as a result the three dimensional topology of a surface can be obtained. An electronic feedback loop constantly adjusts the current and tip height to reach and maintain the preset current and bias voltage.[15] In STM, the resistance between the tip and surface increases exponentially with increasing tip-to-sample spacing, *d*, and as a result a small change in lateral spacing results in a large change in current, *I* (**Equation 1**),

$$I \propto \frac{CV}{d} e^{-2\kappa d} \qquad \text{Equation 1.}$$

where *C* is a constant, and κ is the inverse decay length.[2]

An atomically sharp tip scanning over a surface probes not only the geometry but also the local density of states (LDOS) of the surface. The LDOS, which is related to the highest occupied molecular orbital (HOMO) and lowest unoccupied molecular orbital

(LUMO), can be defined as the sum of all the energy of orbitals at the STM tip. In the case of STM, the LDOS represents the probability of detecting an electron, with energy near the Fermi level, using the STM tip.[16] For example, the tip can probe the LDOS of molecules adsorbed on a surface, which in most cases is influenced by the underlying surface.

STM is routinely used in the surface-science community and is known for its ability to produce real space imaging of adsorbed molecules on a surface down to atomic resolution.[15] An excellent example was reported by Repp *et al*, who imaged molecular orbitals of individual pentacene molecules (**Figure 3**).[17] The experimentally observed lowest unoccupied orbitals (LUMO) and highest occupied orbitals (HOMO) are similar to calculated results using density functional theory (DFT). The experimentally obtained real-space information gives direct insight into the structure of surface absorbed molecules. Understanding of the electronic properties of individual molecules is essential for building molecular electronics.[18]

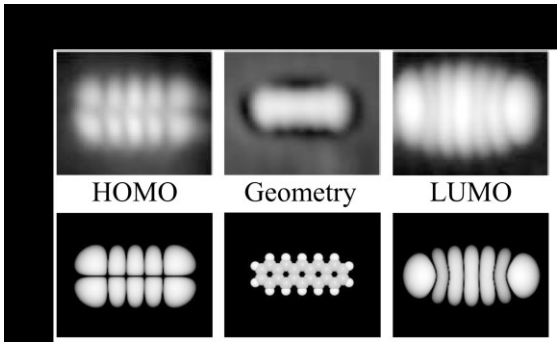

Figure 3. STM image from left to right (top) taken at the HOMO peak, the gap region, and the LUMO peak, respectively. The image taken at the gap region is featureless. The STM images taken at voltages below -2.4 V and above 1.7 V very closely resemble the HOMO and LUMO structures of the free molecule calculated using Density Functional Theory (DFT; bottom left and right). The geometry of the pentacene molecule is shown in the bottom (center).[17]

1.2.3. Operating modes of STM

The presence or absence of a feedback loop leads to the two basic and essential operating modes of the STM instrument: (*i*) constant current and (*ii*) constant voltage, respectively.

***a*. Constant-current imaging (provides 'height' information)**

In this mode, the current is kept constant using an open feedback loop to continually adjust the tip height during the scan (**Figure 4a**). The detector records the height of the tip as a function of position and gives a three-dimensional image of the surface. The height image produced contains both the geometry and information on the local density of states (LDOS). The scan speed is related to the feedback loop bandwidth, and for typical STM imaging it is in the kilohertz range.[14,19]

***b*. Constant-height imaging (provides current information)**

In this mode, the tip is scanned over the surface at a constant height, which means the feedback loop is closed (**Figure 4b**). Changes in the tunneling current can be due to: (*i*) variations in the tip-to-sample spacing and (*ii*) conductivity of functional groups, so recording the current as a function of position gives a surface conductivity map. This mode allows for faster scanning, but the sample surface must be relative flat (not more than a few angstroms in height), without large surface defects or surface steps, to avoid crashing the tip. [14,19]

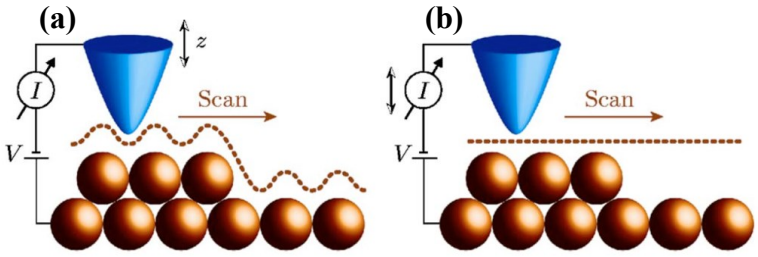

Figure 4. Two basic STM operation modes: (a) constant-current imaging (feedback loop open) and (b) constant-height imaging (feedback loop closed).[14]

Figure 5 is a schematic representation showing the basic principle of elastic tunneling. The tip and sample are separated by a vacuum and the metal tip is assumed to have constant density of states while the sample has featured density of states. The Fermi levels (E_F) for both the sample and the tip lie below the vacuum level by their work function, ϕ. The Fermi level is the term defined as the highest occupied quantum state at an absolute zero temperature. The work function is the minimum energy needed to eject an electron from the Fermi energy level into vacuum. When the tip and sample are in thermodynamic equilibrium, the Fermi levels are equal (**Figure 5a**). Here, when the tip and sample are close enough, electrons may tunnel through the vacuum, but no net tunneling current is established. When a bias voltage is applied, the Fermi level will be shifted upward or downward by the amount of bias voltage, V, depending on the sign of the voltage applied. When the bias voltage is positive, the tunneling current flows from the occupied states of the tip into the unoccupied states of the sample, so the unoccupied states of the sample are imaged (**Figure 5b**). When the bias voltage is negative, the tunneling current flows from the occupied states of the sample into the unoccupied sates of the tip, so the occupied states of the sample are imaged (**Figure 5c**).[20]

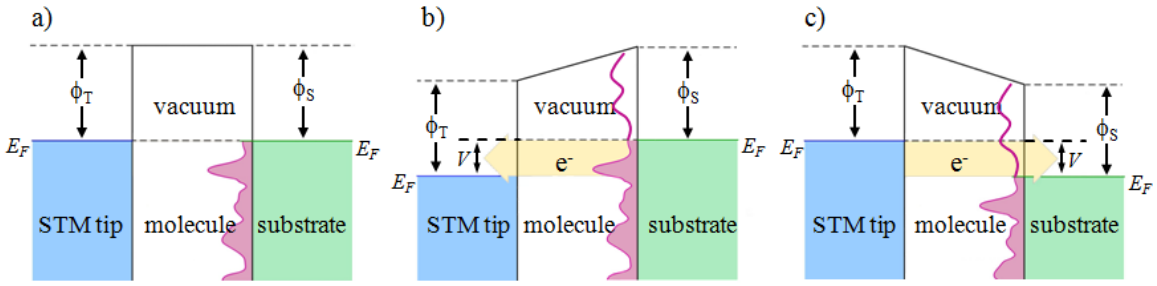

Figure 5. A schematic representation of elastic tunneling: (a) zero bias voltage, no net tunneling (b) positive bias voltage, electron tunneling from STM tip to substrate, and (c) negative bias voltage, electron tunneling from substrate to STM tip, where ϕ_T is the work function for the STM tip, ϕ_S is the work function for the substrate and E_F is the Fermi level.[20]

1.3. Hydrogen bonding

Hydrogen bonding is ubiquitous in nature and has been recognized as one of the most important non-covalent interactions in biological systems. Hydrogen bonding interactions are one of the most studied motifs, due to their relatively strong, selective and directional characteristics, compared to other weaker and less specific noncovalent interactions: van der Waals interactions[21] or dipole–dipole interactions[22], for example. Hydrogen bonding has been shown to be centrally responsible for protein and nucleic acid folding and essential for the stabilization of the DNA double-helix. In order to mimic mother nature and to make various artificial systems, including soft materials, host-guest complexation, molecular networks, *etc.*, hydrogen bonding interactions have been extensively studied in physics, chemistry, and biology.

Hydrogen bonding is defined as a specific attraction between a donor and an acceptor.[23] Specifically, the interaction is between positively polarized hydrogen, which is covalently bonded to an electronegative atom of an H-bond donor molecule, and a negatively polarized atom of an H-bond acceptor molecule. It can occur between different molecules (intermolecular hydrogen bonding) or between different parts within the same molecule (intramolecular hydrogen bonding).

The strength of hydrogen bonding interactions range from 1 to 40 kcal/mol. Based on their strength, hydrogen bonds are typically classified into three categories: (*i*) very strong (15-40 kcal/mol), typically involves a charged H-bond acceptor, *e.g.* $COOH\cdots{}^{-}OOC$, which is also referred to as charge-assisted hydrogen bonding (CAHB), (*ii*) moderate (5-15 kcal/mol), most often observed for neutral H-bond donors and acceptors with N, O as the electronegative atoms, *e.g.* $NH\cdots O$ and, (*iii*) weak (1-5 kcal/mol), where the H is attached to a less electronegative atom, *e.g.* $CH\cdots O$. [24]

Charge-assisted hydrogen bonding (CAHB), where traditional hydrogen bonding is accompanied by Coulombic interactions, leads to exceptionally strong interactions between oppositely charged or zwitterionic components (**Figure 6**).

a)	b)	c)
N—H···O	(δ+)N—H···O(δ–)	(+)N—H···O(–)
N—H···N	(δ+)N—H···N(δ–)	(+)N—H···N(–)
O—H···O	(δ+)O—H···O(δ–)	(+)O—H···O(–)
C—H···O	(δ+)C—H···O(δ–)	(+)C—H···O(–)

Figure 6. a) Normal hydrogen bonding, b) & c) charge assisted hydrogen bonding.

Taking advantage of the strength and directionality of hydrogen bonding, it is up to now the most successful strategy for both 2D and 3D crystal engineering.[25] Predicting crystal structures based on only the chemical structure remains a major challenge in chemistry and biochemistry.[26,27] The introduction of hydrogen bonding simplifies 2D and 3D structure prediction, since it has the potential to override other multiple and weak non-directional collective interactions. Furthermore, enhancing the hydrogen bond strength by ionic charge, (*i.e.* charge assisted hydrogen bonding), can further assist in 2D and 3D molecular design, by making crystal architectures more predictable.

Hydrogen bonding is strong and intrinsically flexible, in as much as there is a high flexibility for a hydrogen bond to bend before it breaks. For the purpose of applications, with these characteristics in mind, their study can inspire solid material design. For example, an advanced material can be made more robust if it can deform while retaining its hydrogen bond connectivities.[28]

2D hydrogen bonding motifs are well studied and there are numerous examples. A classic model system of 2D hydrogen bonding is the trimesic acid (TMA) motif (**Figure 7**).[19,29–33] TMA is a molecule that has three-fold symmetry, with three carboxyl groups arranged around a benzene core. The carboxyl functional group exhibits a dual nature, where the hydroxyl group acts as a hydrogen-bond donor and the oxygen atom acts as a hydrogen-bond acceptor. As a result, two carboxyl groups can interact with one

another and form a dimer. TMA is an excellent example of a "two dimensional tecton" and forms an infinite 2D nanoporous self-assembled network on surfaces under both ultrahigh vacuum conditions and at the liquid-solid interface. It can form one of two polymorphs on HOPG, either a chicken-wire motif or a flower-structure depending on the solvent.[34]

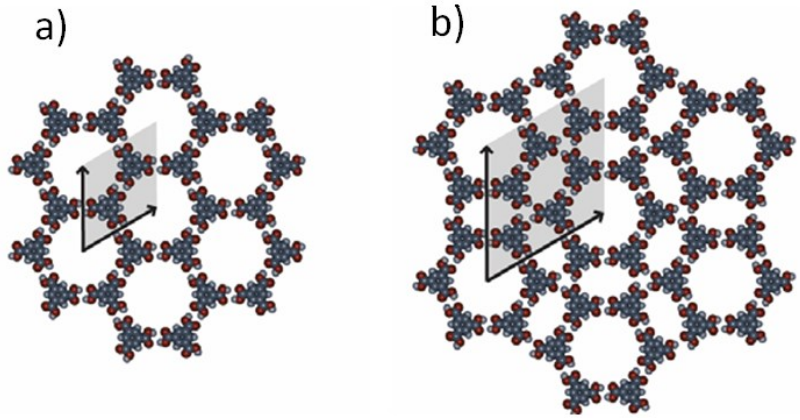

Figure 7. a) Model structures of the TMA chicken-wire (a) and flower motif (b). For each structure, a single unit cell is highlighted in gray. The black arrows indicate the lattice vectors, which have magnitudes of a = 1.66 nm for the chicken-wire structure and a = 2.63 nm for the flower structure. [35]

On the other hand, building CAHB-directed structures on surfaces is in its early development stage with, to our knowledge, only one CAHB surface self-assembly studied thus far.[36] CAHB surface self-assembly will be the focus of chapter 2.

1.4. Moiré pattern

The moiré pattern is well-known in physics and mathematics. It is named after a type of woven fabric which is also called "moiré".[37] It is an interference pattern which can arise when there is a displacement or rotation between two layers of any regular lattice.[38]

1.4.1. HOPG moiré pattern

Highly oriented pyrolytic graphite (HOPG) is extensively used as a substrate for scanning tunneling microscopic (STM) imaging because of its attractive physical properties: (*i*) inertness in air, (*ii*) atomically flat, (*iii*) easily 'cleaned' and (*iv*) high conductivity. A typical STM image of graphite is shown in **Figure 8a**. However, before studying self-assembled monolayers (SAMs) on graphite, it is important to know the structure of HOPG (**Figure 8b**) and be aware of the superlattice phenomena (**Figure 10**), so one does not confuse the superlattice of HOPG to the structure pattern of the SAM of a molecule of interest.[39] Graphite is composed of layered graphene sheets. In each layer, the carbon atoms are arranged in a chicken-wire lattice pattern (**Figure 9a**). Notice, however, instead of a hexagonal pattern, one only observes triangles (**Figure 8a**). Only half of the carbon atoms are typically observed under STM, since the carbon atoms are not all equivalent.[39] The carbon atoms which do not have a carbon atom directly underneath (*i.e.* the red ones in **Figure 8b**) are typically observed under STM.[40]

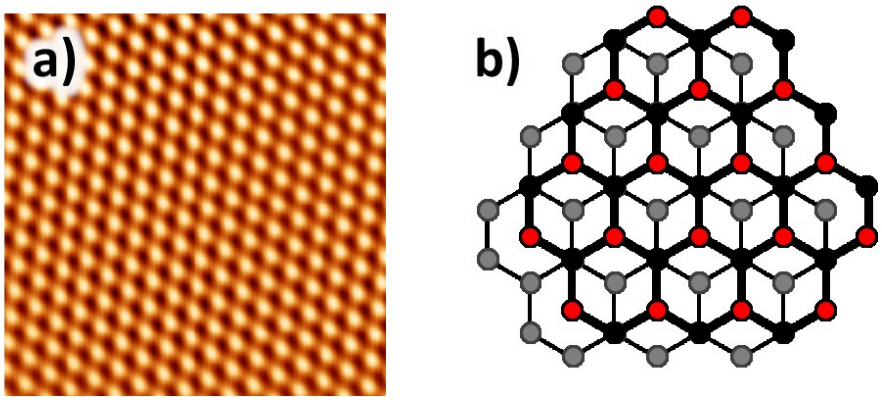

Figure 8. a) STM image of HOPG. 3 nm × 3 nm; I_t = 40 pA, V_b = 50 mV. b) Structure of graphite. Gray carbons represent lower layer, whereas black and red carbons represent upper layer. Only the red carbons are observed under STM.[40]

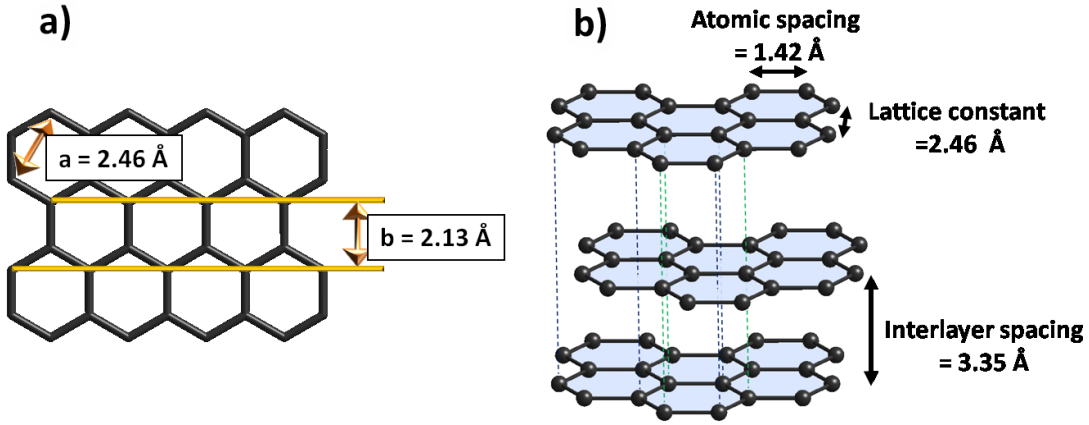

Figure 9. a) Lattice dimensions of graphene.[41] b) Graphite contains layered and shifted sheets of graphene. As a result, there are two non-equivalent carbons. The carbons linked with green dashed lines are eclipsed with carbon atoms of each layer; while the carbons linked by blue dashed lines do not have a carbon immediately underneath or above.

Moiré rotation patterns are widely accepted as one of the explanations for the observation of superlattice phenomena on graphite.[42–44] This results from the rotation of one or more graphene sheets at or near the surface. HOPG has intrinsic defects and sometimes solvent migrates in-between two overlapping graphene layers resulting in shifts or rotation. External force, for example cleavage (a standard cleaning procedure),

can cause dislocations as well. Graphene layers are composed of fused hexagonal rings, with a periodicity of 0.246 nm (**Figure 9a**). Depending on the angle of rotation, the larger periodicity of the resulting hexagonal superstructure can vary (**Figure 10**). In Figure 10a, a superlattice periodicity of 0.857 nm was observed. Base on calculations, this periodicity corresponds to a *ca.*10° shift between two graphene sheets (**Figure 10b**). Larger rotations give smaller superlattice periodicities (**Figure 10c & d**).

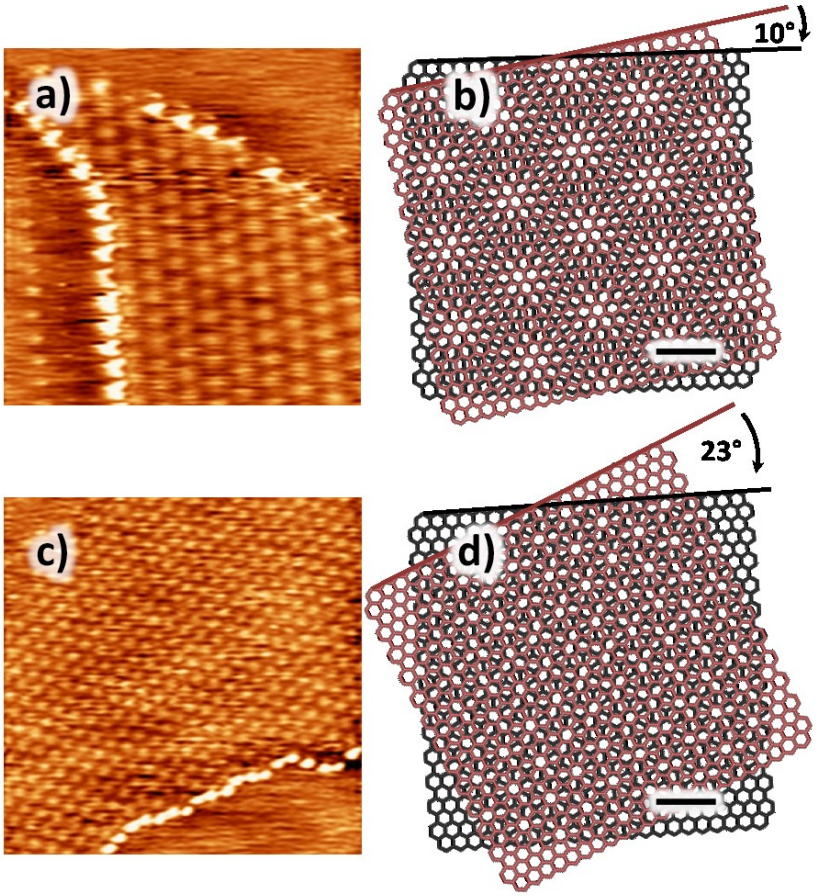

Figure 10. (a & c) STM images of graphite moiré patterns. The superlattice has a hexagonal symmetry with periodicity 0.857 nm and 0.461, respectively. The bright lines of spots outline the top graphite sheet boundary edge (a) 100 nm × 100 nm; I_t = 50 pA, V_b = -665 mV; (c) 100 nm × 100 nm; I_t = 20 pA, V_b = -475 mV. (b and d) Representations of the moiré patterns of the STM images. superlattice periodicities of 0.857 nm and 0.461 nm would require 10° and 23° shifts of the two graphene sheets, respectively. The scale bars in b) and d) represent 1 nm.

1.4.2. Molecular moiré pattern

Rod-like molecules tend to pack in lamella on surfaces (**Figure 11**). The intermolecular distance is the perpendicular distance between the long axes of the molecules. For pure alkanes, when they self-assemble on HOPG forming lamellar structure (**Figure 11**), with the zigzig axis of the carbon skeleton parallel to the graphite, alkyl chains preferably follow one of the three axes of graphite (**Figure 12**). The intermolecular distance is 4.26 Å (**Figure 9a**) which is two graphite lattice unit (b direction in **Figure 9a**). This perfect matching is called commensurate packing (**Figure 11 left**). A typical STM image of an alkane is shown in Figure 13.[45] Only equivalent or very similar adsorption sites give the same tunneling contrast, therefore, there is no moiré pattern in the lamella direction since each alkane sits on the same relative position on graphite.

On the other hand, the methylene groups on alkyl chains are separated 2.54 Å from each other which is slightly longer than the lattice distance of 2.46 Å (**Figure 9a**). This mismatch results in the observed moiré pattern (N.B. change in contrast) along the molecular axis.

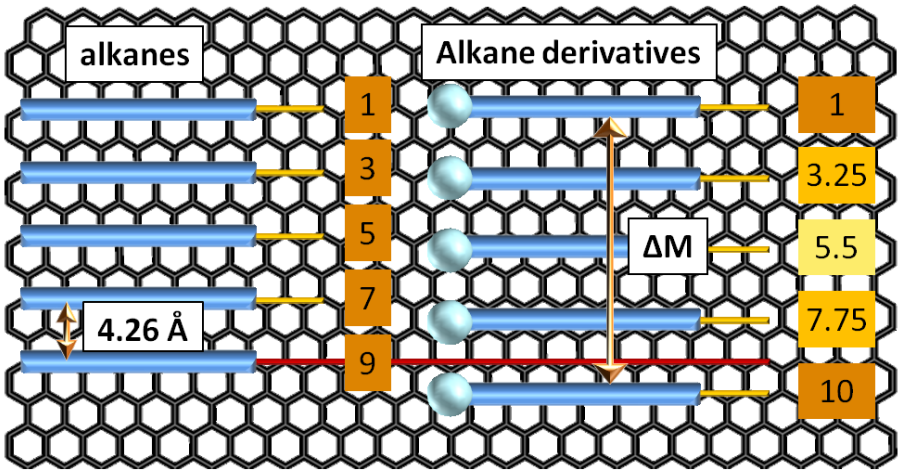

Figure 11. Alkane (left) and alkane derivative (right) packing on graphite. Blue cylinders represent alkyl chains. Alkyl chains all follow one of the principal axes of graphite. Yellow lines highlight the position of alkyl chains, and the relative position of alkyl chains with respect to the HOPG lattice is numbered in yellow boxes. Alkanes form commensurate packing on HOPG (left). If one considers the upper HOPG lattice position as position 1, the next yellow line would be position 3, since one HOPG lattice is skipped (left). Such alkane derivatives often form incommensurate packing on HOPG (right). With different adsorption position of alkyl chains to HOPG (right), the brightness of alkyl chains change due to different electronic interactions. ΔM denotes the moiré period.

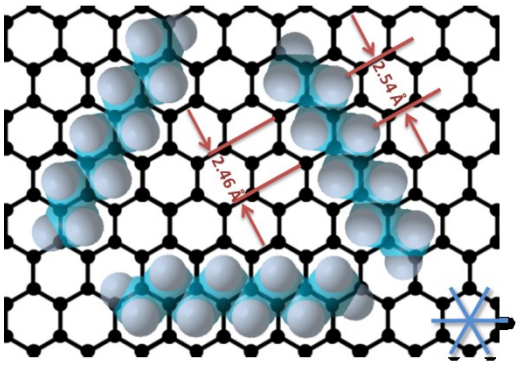

Figure 12. All-*trans* alkyl chains preferably follow one of the three principal axes of graphite. The three main symmetry axes of graphite are indicated by the three blue lines. The separation distance of the two methylene groups of an alkyl chain and the two (‘*meta*’) carbons on graphite is 2.54 Å and 2.46 Å, respectively.

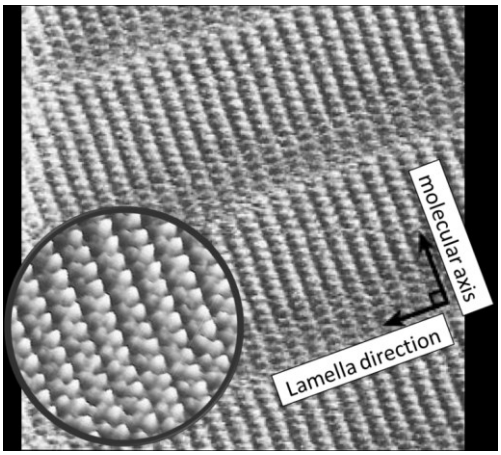

Figure 13. STM image of self-assembled triacontane ($CH_3(CH_2)_{28}CH_3$) forming lamellae on HOPG. The molecular axis is perpendicular to the direction of the lamellae. 10 nm × 10 nm; I_t = 166 pA, V_b = 1235 mV. Inset is the zoomed in image which shows doubling of spots, which demonstrates that the zigzag plane of the alkyl chain lies parallel to the graphite surface as shown in **Figure 12**.[45]

When there is a functional group attached to an alkyl chain, in most cases the alkyl chains will separate further apart to minimize steric repulsion. On the right side of Figure 11, the first alkyl chain sits on the zigzag carbon frame of graphite, while every other alkyl chain is slightly shifted away from the original position (as shown on the left), until the fifth alkane derivative arrives to the same adsorption site as the first one (ΔM; **Figure 11**). Because of this shift or mismatch, under STM the brightness (a measure of the tunneling current) of each alkyl chain can vary. The result of this incommensurate packing is a molecular moiré pattern (**Figure 14**).[35]

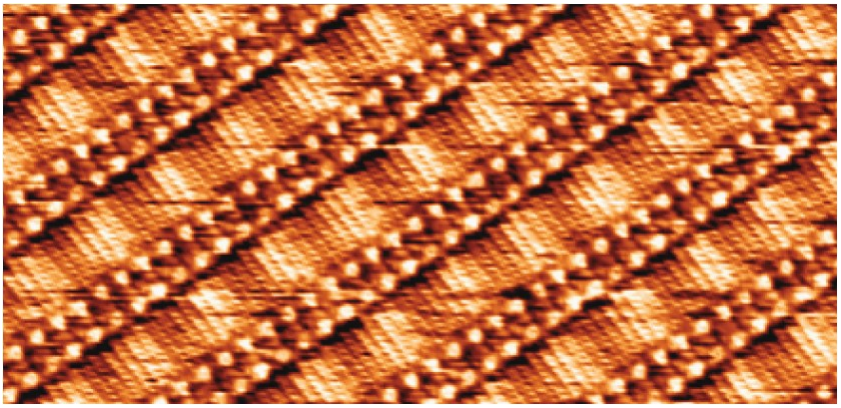

Figure 14. An STM image of TMA/$C_{17}H_{35}OH$ SAM self-assembly on HOPG. 18 nm × 9 nm; I_t = 20 pA, V_b = -800 mV. A wave-like pattern, with periodic changes in brightness is observed in the alkyl chain region.[35]

1.5. Multilayer formation visualized by STM

Conventionally, STM is used to image self-assembled monolayers or sub-monolayers.[46] Gradually, the power of using STM to image multilayers is emerging. A logical and important question that should be addressed is: "what is the maximum number of adlayers that can be imaged by STM?" As computationally calculated by Wawkuschewski *et al*., for a typical non-conducting molecule, as many as three layers of adsorbed overlayers can be imaged.[47] Nevertheless, the answer may vary depending on the conductivity of individual molecules. Magonov *et al*. successfully observed criss-crossed multilayers of long chain alkanes, where the observed STM pattern arises from the most protruded hydrogen atoms of the topmost layer.[48] The angle between the criss-crossed layers was usually 60°, and 90° angles between the overlapping layers were also observed, but with much less frequency. Parallel multilayers can also occur, however they are harder to identify and are often confused with double-tip artefact. Tahara *et al*. carried out MM3 force field molecular mechanics simulations which explained why a 60° interlayer angle is most likely (*vide infra*).[49] By rotating one of the interlayers, and calculating the interaction between the adlayers, they found one global minimum when the interlayer angle was 60°. In addition, they also found local minima when the interlayer angle was 0° or 90°. On the other hand, other authors believe the HOPG substrate, which has three-fold symmetry, still has influence on the growth of a second layer.[49]

Self-assembled monolayers, with the aid of the underlying substrate (*e.g.* HOPG), are ideally 'defect free' due to their dynamic 'self-healing' ability. However, the second adlayer, which is decoupled from the substrate by the first layer, can have more 'mistakes' in self-assembly. Small pores or holes, the size of one or more molecules, may appear in the self-assembled second layer at random locations (**Figure 15**).[50] This phenomenon of 'appearing holes' in adlayers is more likely for molecular self-assembly mediated by only weak interactions (van der Waals or π-π interactions), or, in other words, lacking relatively strong hydrogen bonding or electrostatic interactions.[50–52] This

unique characteristic can, in fact, be used to recognize multilayer assembly, which sometimes can be tricky to identify otherwise.

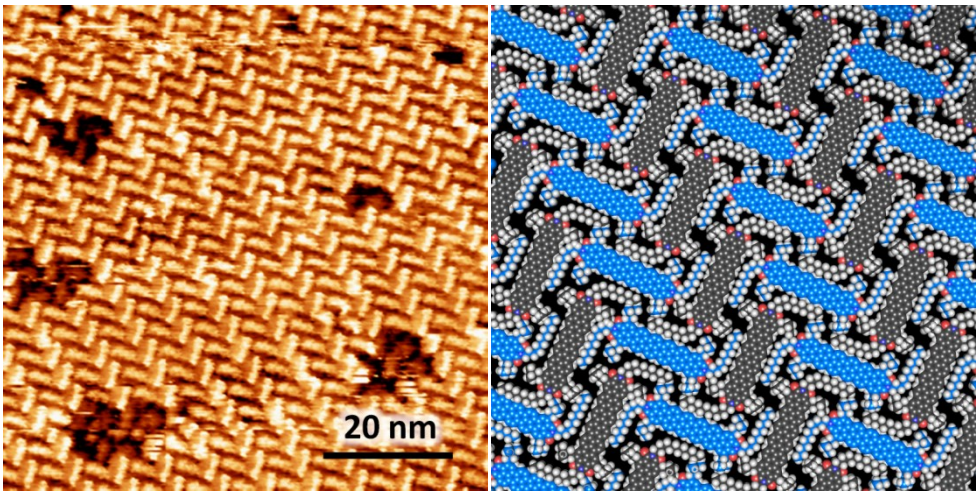

Figure 15. Self-assembled network of a hexarylene diimide (HDI) at the TCB/HOPG interface. a) STM image showing the presence of holes or defect sites, where the lower layer can be observed. b) Molecular model of the herringbone pattern of one layer of HDI. Imaging conditions:, I_t = 85 pA. V_b = 785 mV.[50]

By changing the bias voltage, while keeping the tunneling current constant, Crivillers *et al*. and Samorı *et al*. were able to selectively observe multilayer, monolayer or graphite.[53,54] Recall that in STM imaging there are three variables: (*i*) tip sample separation, (*ii*) tunneling current, and (*iii*) bias voltage. When changing the bias voltage, the tip height has to change in order to keep the tunneling current constant. At constant current, increasing the bias voltage will result in increasing the tip-substrate separation, and *vice versa*. Recall that in STM, one can also image at negative voltage, and in this case, decreasing the bias voltage (*i.e.* voltage becomes more negative) increases the tip-substrate separation. On the other hand, keeping the bias voltage constant while increasing the current set point will decrease the tip-substrate separation. It is generally agreed that a scanning STM tip is approximately 5 to 10 Å from the surface.[55] For double layer assembly, the distance between two overlayers is *ca*. 3.5 Å.[56,57] In this case, one may ask: "when decreasing the bias voltage or increasing the tunneling current does the STM tip 'remove' the top layer to image the bottom layer?" Crivillers *et al*., Blunt *et al*.,

and Yoshimoto *et al*. believe that the tip removes the top layer during imaging at the liquid-solid interface.[53,56,58] More evidence for tip-modified surfaces was recently demonstrated by Ivasenko *et al*., who successfully erased or dissolved part of an adlayer by bringing the tip closer to the substrate while imaging.[59] In this case, after bring the STM tip further away from the surface and zooming out from the original scan area, the authors were able to see a square hole showing bare substrate (**Figure 16**). On the other hand, Piot *et al*. believe that the STM tip does not remove overlayers.[52] Using sequential images, monolayers were imaged at low voltage while double layers were imaged at high voltage. Most importantly, this process was reversible and the second layer 're-appeared' at the same location with similar shape and size. They believe it is possible to image different adlayers under different tunneling conditions and called this phenomenon 'tunneling transparency'. Future STM studies at the liquid-solid interface are expected to shed more light on these different multilayer imaging theories, in particular, which one is more likely or do they coexist?

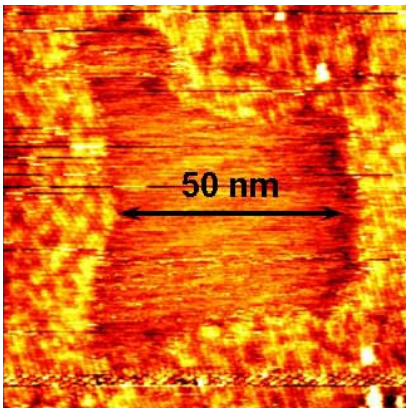

Figure 16. Tip assisted desorption of TMA-selenosunflower. This image was taken immediately after scanning at I_t = 1000 pA, V_b = 500 mV in a 50 × 50 nm^2 area by zooming out to 90 × 90 nm^2 and scanning at I_t = 300 pA, V_b = 800 mV. (from Supramolecular assembly of heterocirculenes in 2D and 3D)

Towards the controlled self-assembly of supramolecular bilayers

a. Concentration:

It has been demonstrated in several groups that multilayer formation can be controlled by sample concentration. Ivasenko *et al*. has shown the accumulation of multilayers upon gradual drying of a heterocirculene sunflower with trimesic acid (TMA) in DMF.[59] Similar results have been shown by Chen *et al*., where at high metallocycle concentration, bilayers and trilayers were observed and at higher concentrations, both the second layer and the third layer grow larger.[51]

b. Guest molecule

Formation of supramolecular bilayers may be induced by guest molecules. Blunt *et al*. has demonstrated the process of induced growth of a second layer by a three-dimensional guest molecule (C_{60}) and subsequent erasing of the top layer by a two-dimensional guest molecule (coronene).[56] Significantly, the formation of the bilayer network is reversible, where guest exchange leads to changes in the third dimension perpendicular to the surface.

Template-assisted assemblies for the patterning of functional molecules

With fine control, layered self-assembly of different molecular additives can be achieved. Piot *et al*. were able to demonstrate heteroepitaxial growth of a disklike graphene molecule (hexakis(*n*-dodecyl)-peri-hexabenzocoronene; HBC-C_{12}) on a *n*-$C_{50}H_{102}$ monolayer by first assembling a long *n*-alkane, *n*-$C_{50}H_{102}$, on the HOPG surface, followed by addition of HBC-C_{12} in *n*-tetradecane solution (**Figure 17**).[60] The highly ordered monolayer of *n*-$C_{50}H_{102}$, which functions as a template, induced new types of HBC-C_{12} packing different from the packing structures obtained on HOPG alone. The alkane template slowed down the physisorption process of HBC-C_{12}. Lee *et al*. also demonstrated the use of long *n*-alkanes as templates for engineered molecular nanostructures.[61] In this case, the template was the solvent molecule itself, where long *n*-alkanes (C_nH_{2n+2}, $n \geq 13$) have very strong affinity to the substrate.

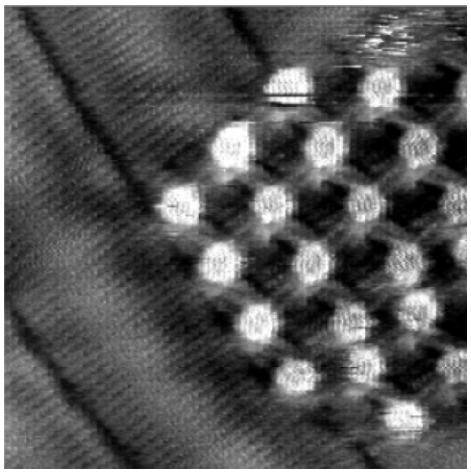

Figure 17. STM images showing an HBC-C_{12} island adsorbed on top of an *n*-$C_{50}H_{102}$ monolayer; imaging conditions: 18.7 × 18.7 nm^2, I_t = 5.4 pA V_b = 634 mV.[60]

In this section, we have described that in contrast to the study of monolayer patterns of molecules, multilayers are also possible and show a rich diversity of self-assembly and organization due to the delicate balance of interactions among molecules, solvent and the surface. Through the use of STM, one can begin to explore self-assembled multilayers of molecules, as exemplified by these select literature examples. The potential applications of such hierarchical organizations of molecules will be discussed in Chapter 3.

1.6. Mechanochemistry

Greener reactions have gained much attention not only in science but also for economic and political reasons.[62] Various governmental regulations require industries to properly treat their chemical waste. The high cost of waste disposal has stimulated the study of solvent-free chemical reactions. Mechanochemistry is one very suitable alternative for chemical industries, since it minimizes the use of costly and toxic organic solvents, and ultimately reduces the discharge of hazardous organic waste into the environment.[63–65] Many stoichiometric solid-solid reactions give 100% yields, therefore there is no need for costly and time-consuming purification. Furthermore, since extraction of the products from the reaction mixture is not required, solvent consumption and waste disposal are minimized.[66] Mechanochemistry avoids the limitations of solution-based chemistry, such as solubility, solvent complexation, or solvolysis[67] and is significantly faster than conventional solution based techniques, while providing higher yields and often improved selectivity towards the desired product.[63,64,66,68] Finally, solid state reactions of various types can often be scaled up to industrial levels (**Figure 18**).[66] As a result, solid state mechanochemistry is sustainable and environmentally benign.

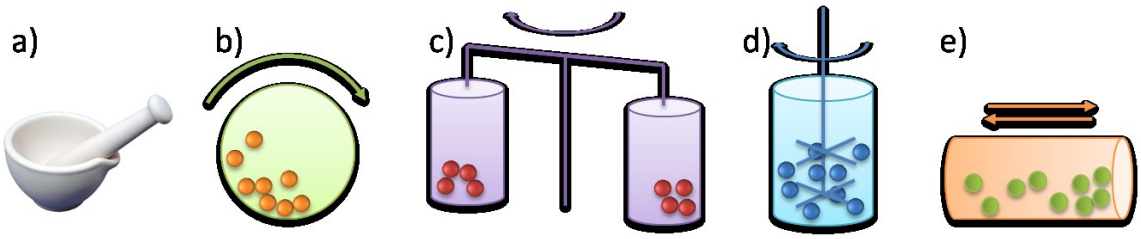

Figure 18. Mechanochemistry equipment: Mortar and pestle (a). (b to e) different types of mills.[69]

The term “mechanochemistry” was first introduced by Wilhelm Ostwald in his book “Textbook of General Chemistry” (1885). He explained mechanochemistry from the energy point of view. The implementation of mechanochemistry has long been a part

of human history.[70] For example, ancient fire making took advantage of friction to ignite solid explosives by shock.[70]

Mechanochemistry includes the use of a mortar and pestle, grinding using many small beads, ball milling and planetary mills (**Figure 18**). Milling can provide enhanced reactivity of the reagents since the strong mechanical impact of the balls will continuously and efficiently provide fresh contacts between the solid reactants.[71] The reactivity of the reagents is enhanced due to: (*i*) effective reagent mixing, which increases the reagent's surface area enormously, and (*ii*) increased temperature and pressure.[71] For example, Urakaev *et al*. (2000) have developed a model showing that a local temperature of *ca.* 1000 K and pressures of several thousand atmospheres can be achieved in ball milling.[72]

In conclusion, given the advantages of green chemistry, mechanochemistry should be applied to more types of reactions. As such, a library of reaction types and successful examples is continuously growing. Herein, solvent-free and mechanochemistry will be applied towards the synthesis of *para*-aminobenzoquinone derivatives, *meta*-aminobenzoquinone derivatives and a *meta*-aminobenzoquinone Ni complex.

Chapter 2.

Charge-Assisted Hydrogen Bond-Directed Self-Assembly of an Amphiphilic Zwitterionic Benzoquinonemonoimine at the Liquid-Solid Interface

Published as:

Fang, Y.; Nguyen, P.; Ivasenko, O.; Aviles, M. P.; Kebede, E.; Askari, M. S.; Ottenwaelder, X.; Ziener, U.; Siri, O.; Cuccia, L. A. *Chem. Commun*. **2011**, *47*, 11255.

2.1. Abstract

Charge-assisted hydrogen bond-directed self-assembly of a zwitterionic benzoquinonemonoimine was investigated at the liquid/solid interface using scanning tunneling microscopy. Factors governing morphology, chirality and multilayer formation are discussed, presenting an important foundation for understanding the properties of a large family of related molecules with interesting potential in supramolecular design.

2.2. Introduction

Molecular self-assembly and self-organization are ubiquitous in nature and are becoming increasingly important in the realm of molecular engineering.[73] This bottom-up approach relies on encoding specific and directional interactions within the molecular building blocks themselves.[23,74] In the special case of surface self-assembly, conveniently studied by scanning tunneling microscopy (STM), in-depth understanding and control of selected supramolecular interactions has been demonstrated by elaborate design of highly ordered multi-component hierarchical nanostructures.[75] Charge-assisted hydrogen bonding (CAHB), where traditional hydrogen bonding is accompanied by Coulombic interactions, leads to exceptionally strong and inherently flexible interactions between oppositely charged or zwitterionic components.[76,77] The typical energy of a normal N-H···O HB is ≤ 4 kcal/mol while that of a (+)N-H···O(-) CAHB is almost 4 times as strong (15.2 kcal/mol).[78,79] Rational supramolecular design utilizing CAHB is, however, in its early development stage with only few CAHB surface self-assemblies studied thus far.[80–83] In contribution to this promising field herein we present the first surface self-assembly STM investigation of a novel amphiphilic zwitterionic benzoquinonemonoimine (**C18*m***, **Figure 19a**).

In 2002, Braunstein and Siri discovered unusual 6π+6π electron zwitterionic *p*-benzoquinonemonoimines that form strong CAHB in the solid state.[84] Recently, Braunstein *et al.* have investigated the adsorption of the *N*,*N*'-dibutyl derivative (**C4*m***, **Figure 19a**) on metallic (gold) and ferroelectric (lithium niobate) surfaces using a suite

of photoemission spectroscopy techniques.[85,86] They observed pronounced epitaxial growth due to strong adsorbate-substrate interactions and were able to corroborate preferential molecular orientations of **C4*m*** in monolayers. To get detailed insights into supramolecular interactions and factors governing surface self-assembly of zwitterionic *p*-benzoquinonemonoimines we wanted to study their adsorption on a less reactive surface using STM. Targeting stable surface adsorption of this class of compounds on highly oriented pyrolytic graphite (HOPG), we have designed **C18*m*** with two octadecyl chains capable of providing multiple van der Waals contacts between the molecules and the substrate. It was synthesized according to a convenient one-pot transamination reaction developed by Braunstein *et al*.[87]

2.3. Results and Discussion

C18*m* applied onto a freshly cleaved HOPG surface in 1,2,4-trichlorobenzene (TCB) was easily imaged by STM and resulted in the formation of multi-domain ordered assemblies where bright zigzag rows of quinone head groups were separated by darker regions of alkyl chains packed into lamellae (**Figure 19b**).

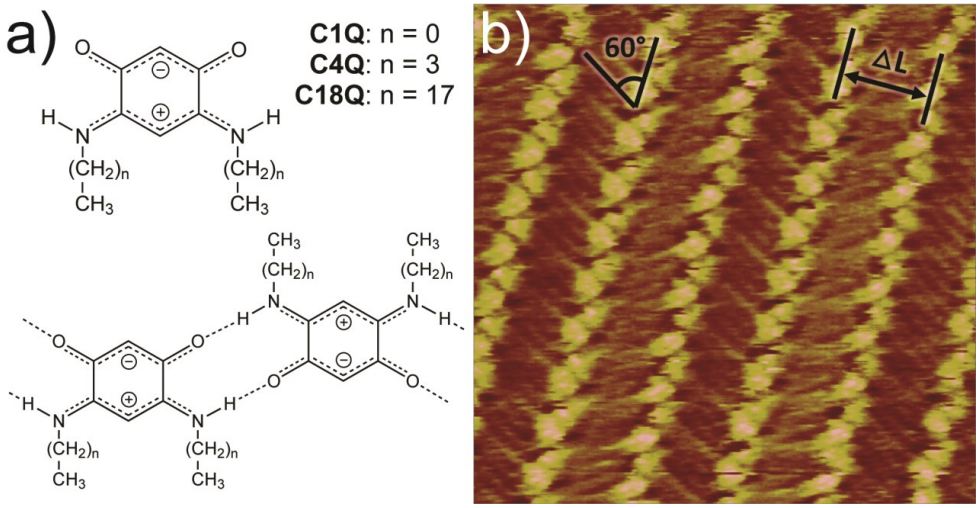

Figure 19. (a) Structure and CAHB zigzag of zwitterionic *p*-benzoquinonemonoimines. (b) STM topography image of **C18*m*** at the TCB/HOPG interface highlighting the lamellar width, ΔL (27.8 Å) and the angle between alkyl chains and head group rows (60°). 15 nm × 15 nm; I_t = 19.8 pA, V_b = -259.4 mV.

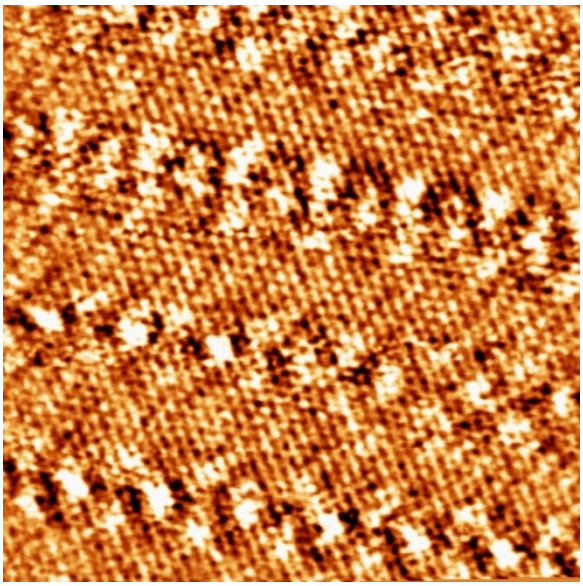

Figure 20. STM topography images of **C18*m*** at the HOPG/TCB interface under ambient conditions. The molecular orientation is superposed on a resolved graphite lattice. This image reveals the molecular orientation with respect to HOPG. 10 nm × 10 nm; I_t = 23.3 pA, V_b = 581.2 mV.

The width of the stripes (ΔL) was measured to be 27.8 ± 0.3 Å (**Figure 19b**). This, together with a 60° ± 2° angle between the alkyl chains and the head group rows (**Figure 27**), indicates that the alkyl chains are fully extended and interdigitating within the lamellae. The periodicity of the zigzag rows, 14.8 Å (denoted as a_1 or a_2 in **Figure 26a**) accounts for two **C18*m*** molecules per period and is in agreement with hydrogen-bonded *p*-benzoquinonemonoimine zigzags found in the crystal structure of **C1*m***.[88] Although this corresponds to essentially planar zigzags of aromatic cores linked *via* fully stretched out CAHBs (*i.e.* the flat CAHB head group network unit cell width of **C1*m*** is 14.9 Å), the spacing is too small for the adsorption of four C_{18} alkyl chains on HOPG since the minimum spacing between neighbouring alkyl chains is *ca.* 4.2 Å.[89] Indeed, the observed ratio between the alkyl chains and the head groups in the packing of **C18*m*** is 1.5, indicating that for every two molecules, one alkyl chain is missing. The missing alkyl

chain phenomenon has been reported by several research groups with the most common explanation being that the unrevealed alkyl chains are, "pointing out of the plane of the monolayer into the liquid phase."[90–92] (**Figure 21**) While there is no direct method to confirm or rule out this hypothesis several observations presented below suggest an alternative arrangement for **C18*m*** self-assembly.

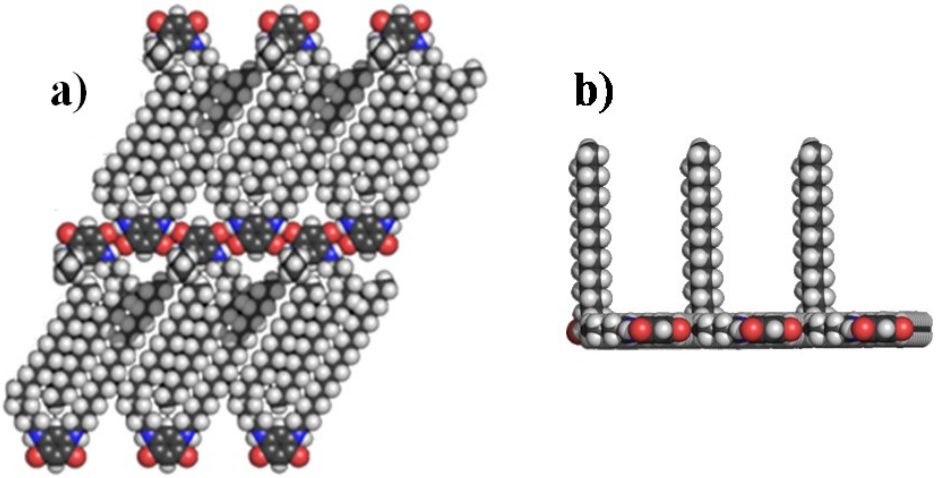

Figure 21. Alternate packing model of **C18*m*** with an alkyl chains pointing out of the plane of the monolayer; a) top view and b) side view.

The experimentally observed tilt and co-alignment of the alkyl chains is only possible for **C18*m*** conformations where the aromatic core is bent away from the plane of the alkyl chains. As a consequence, each hydrogen-bonded zigzag is also non-planar with a complex quasi-three-dimensional intedigitated structure of alkyl chain lamellae featuring multiple attractive van der Waals interactions (**Figure 22**).

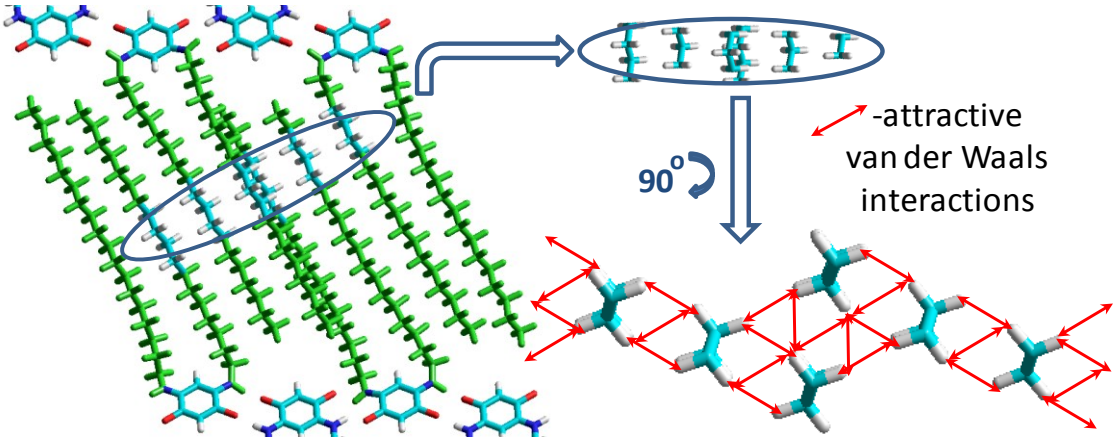

Figure 22. Schematic representation of multiple van der Waals interactions between alkyl chains of a **C18*m*** monolayer. Here we have used a small **C18*m*** cluster where all aromatic cores were frozen at experimentally observed distances while alkyl chains within lamella were allowed to relax using general force field MM+ implemented in HyperChem 7.5 (Copyright 2002; HyperChem, v. 7.5; HyperCube Inc.; Gainesville, FL.)

A simplified model is shown in Figure 25 a & b. This heterogeneity within the lamellae was repeatedly observed in many high-resolution images of **C18*m*** monolayers (**Figure 23** and **Figure 25**) where every third alkyl chain appears brighter than its neighbours. This variation in contrast is different from the estimated Moiré pattern (17.2 Å, *i.e.* 4 alkyl chains, **Figure 24**), suggesting its molecular origin.

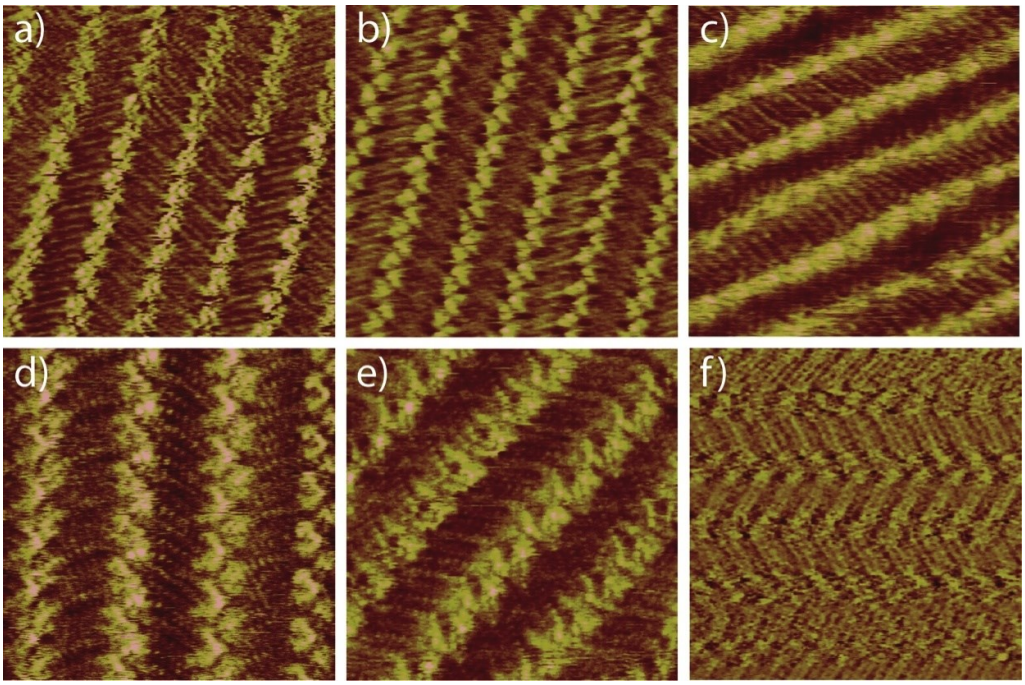

Figure 23. STM topography images (a-e) and current image (f) of **C18*m*** where the periodicity of every third alkyl chain is observed. (a) 15 nm × 15 nm; I_t = 17.3 pA, V_b = -522.7 mV; (b) 15 nm × 15 nm; I_t = 17.3 pA, V_b = -322.9 mV; (c) 15 nm × 15 nm; I_t = 40.0 pA, V_b = -300 mV; (d) 10 nm × 10 nm; I_t = 16.0 pA, V_b = -500 mV; (e) 10 nm × 10 nm; I_t = 22.0 pA, V_b = -485.2 mV and (f) 20 nm × 20 nm; I_t = 18.7 pA, V_b = -734.9 mV.

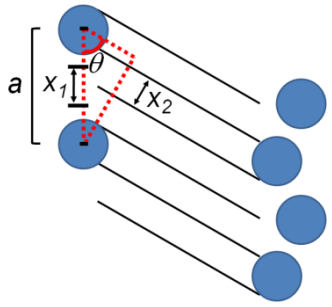

Figure 24. Graphite periodicity = 2.46 Å; Periodicity of the zigzag rows (a) = 14.8 Å; Distance between alkyl chains along the headgroup axis (x_1) = 14.8 Å /3 = 4.93 Å; Angle between alkyl chains and head group rows (θ) = 60°; Perpendicular alkyl chain periodicity (x_2) = 4.93 Å x sin(60°) = 4.27 Å; Calculated moiré pattern = 4 chains.

Further indirect evidence of the proposed neatly packed double-decker lamellae is the facile growth of ordered multilayers (*vide infra*); which cannot be expected for a structure with flying ("pointing out of the plane of the monolayer") alkyl chains.

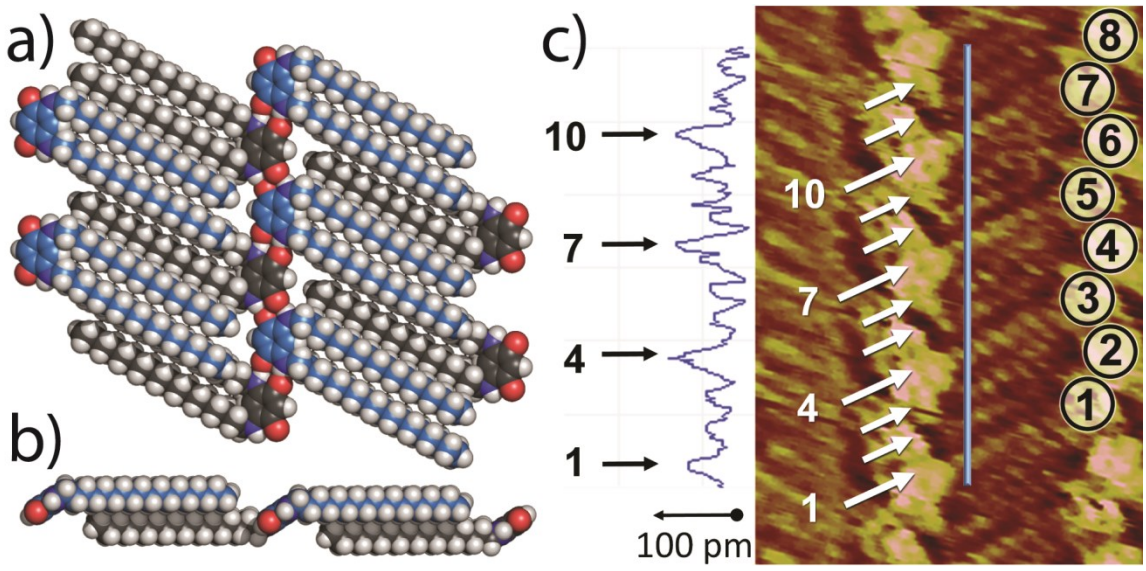

Figure 25. (a) Top view and (b) side view of the proposed packing model of **C18*m***. (c) STM topography image of **C18*m*** adsorbed at the TCB/HOPG interface with eight head groups identified with circles and twelve alkyl chains identified with white arrows. The line profile highlights the brighter alkyl chains. 5.2 nm × 7.5 nm; I_t = 19.8 pA. V_b = -259.4 mV.

Upon surface self-assembly, achiral **C18*m*** adopts a bent conformation that is chiral and thus exists as two enantiomers (inset in **Figure 26**). The unusual double-decker packing of the alkyl chains in interdigitated lamellae enforces an intrinsically racemic composition of **C18*m*** monolayers since both enantiomers are required. An alkyl chain lamella built from a single enantiomer would have an unfavourable crisscrossing arrangement of alkyl chains (**Figure 26c**) and as a consequence, low stability.

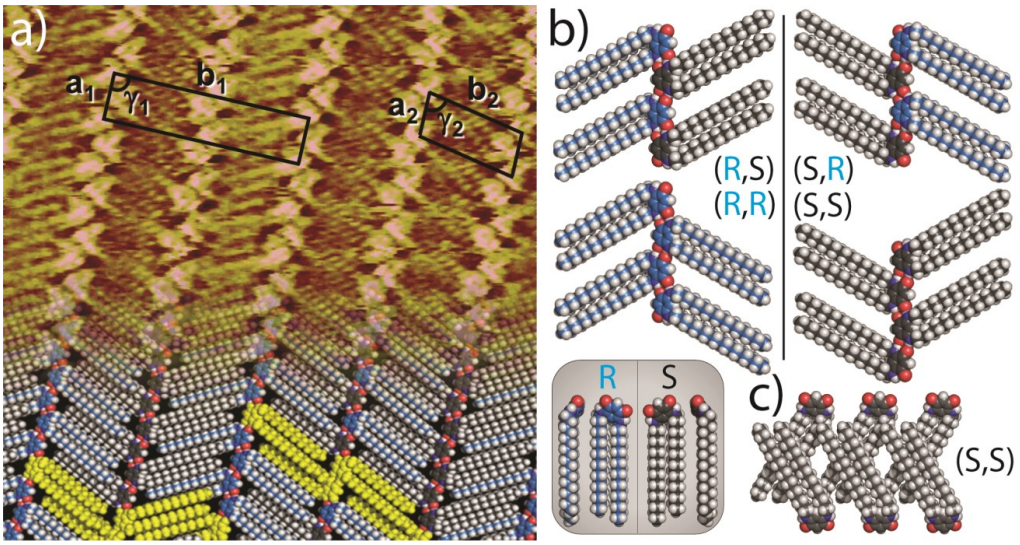

Figure 26. (a) STM topography images (upper) and model (lower) of **C18*m*** at the TCB/HOPG interface. Herringbone arrangement (a_1 = 14.8 Å, b_1 = 55.6 Å and γ_1 = 90°) and linear arrangement (a = 14.8 Å, b = 29.4 Å and γ = 79°) unit cells are shown. 15 nm × 15 nm; I_t = 13.0 pA, V_b = -313.4 mV. Inset: right- and left-handed conformations of **C18*m*** (top and side view) are identified with blue (R) or grey (S) carbons. (b) CAHB of head groups with alternating chirality generates a linear arrangement of the alkyl chains, while CAHB of head groups with the same chirality generate a herringbone arrangement. (c) Packing of homochiral chains within one row results in unfavourable crisscrossing of alkyl chains.

Two pairs of enantiomeric zigzags can be identified: 'herringbone' (RR or SS, highlighted in **Figure 26a**, left) and 'linear' (RS or SR, highlighted in **Figure 26a**, right), named so for their appearance (**Figure 26b**). Since all four motifs are randomly distributed within the **C18*m*** adlayers, the planar organization of **C18*m*** represents an unusual type of pseudoracemate.[74] The coexistence of enantiomerically pure and racemic zigzags thus implies a small energy difference in their formation and mixing. Assuming that thermodynamic equilibrium is reached, the calculated difference in free energies of these self-assembly modes is only 1 kcal/mol. 107 pairwise alkyl chain observations were tabulated and 15 linear and 92 herringbone arrangements were observed in 19 distinct images of **C18*m***. This corresponds to 86% of herringbone and 14% of linear arrangements (*i.e.* $\Delta G = -RT\ln K$ = -8.314 x 298 x ln(86/14)=-4497.5 J/mol, or ~1 kcal/mol).

The substrate often plays an important role in the resolution of racemates into racemic conglomerates since it limits the configurational space available to racemates.[74,93] In this case however, the 60° tilt between alkyl chains and head-group rows within lamellae results in perfect co-alignment of the alkyl chains and head-group rows with the main symmetry axes of HOPG independently of the enantiomeric nature of the molecules (**Figure 27a**). This pseudoracemic packing does not imply weakness of the adsorbate-substrate interactions, as, in fact, they are very strong and in full control over the possible orientations of the domains (**Figure 27b**).

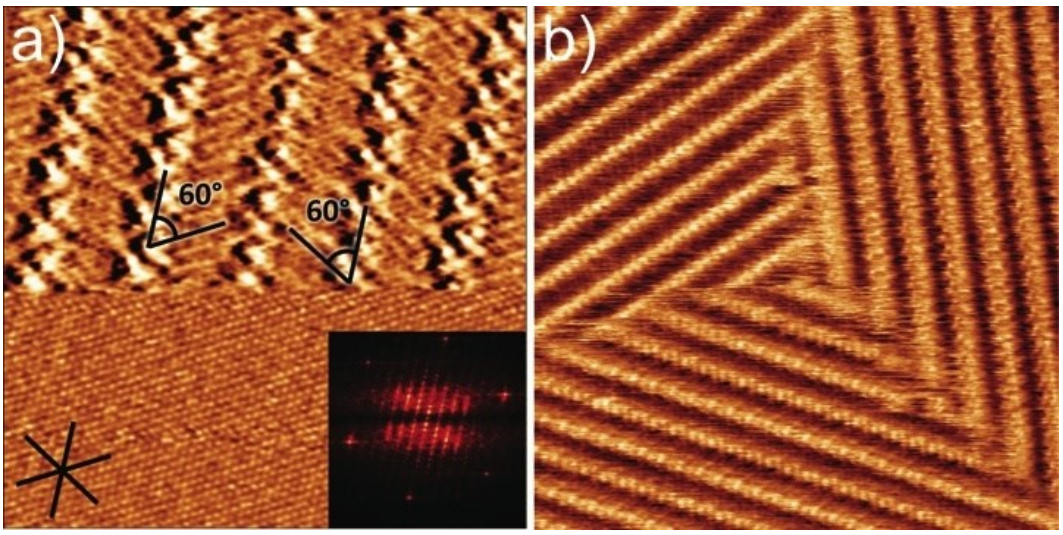

Figure 27. (a) STM current image of C18m at the TCB/HOPG interface. The current was changed during scanning, revealing atomic resolution of the HOPG. The angle between alkyl chains and head groups is 60 ± 2°. 15 nm × 15 nm; I_t = 17.3 pA. V_b = -322.9 mV (SAM). I_t = 17.3 pA, V_b = 40 mV (HOPG). Inset: 2D Fast Fourier Transform indicates that head group rows of **C18*m*** follow one of the main axes of HOPG. (b) STM topography image of C18m at the TCB/HOPG interface. 43 nm × 43 nm; I_t = 1.26 pA, V_b = -433 mV.

Multilayer assemblies have been previously visualized using STM.[53,94] Such studies are important both for understanding crystal growth mechanisms and as an advanced level of supramolecular design. Upon prolonged imaging (and/or using supersaturated solutions) we have repeatedly observed the formation of **C18*m*** bilayers. Nucleated and initially growing complementary to the underlying layer to maximize favourable van der Waals

interactions, the second layer often extends over domain boundaries leading to misaligned bilayers easily visualized as a characteristic rhomboidal grid (**Figure 28** and **Figure 29**).

The most stable structure of bilayer is the one with parallel arrangement of lamellae in both layers which is expected to maximize favorable van der Waals interactions (**Figure 28**). 'Criss-cross' bilayer is simply the result of continuous growth of the second layer over multi-domain region of the first layer in which all domains are rotated by 60° with respect to each other (**Figure 30**). Since STM observations of thicker **C18*m*** films was technically hindered (low conductivity) we turned our attention to its self-assembly in the solid state.

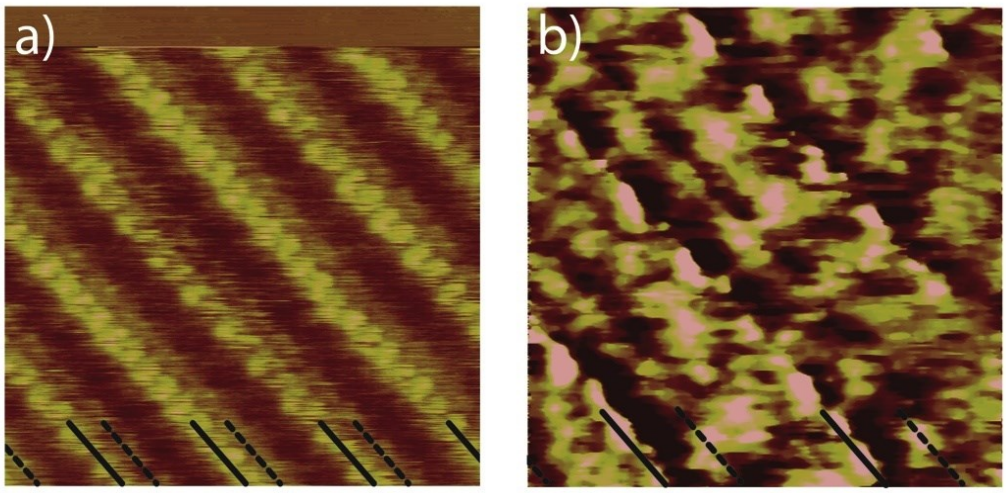

Figure 28. STM topography images of **C18*m*** at the HOPG/TCB interface showing offset parallel bilayers. Dashed lines highlight the lower layer and solid lines highlight the top layer. (a) 15 nm × 15 nm; I_t = 20.0 pA, V_b = -518.8 mV and (b) 10 nm × 10 nm; I_t = 20.3 pA, V_b = -96.6 mV.

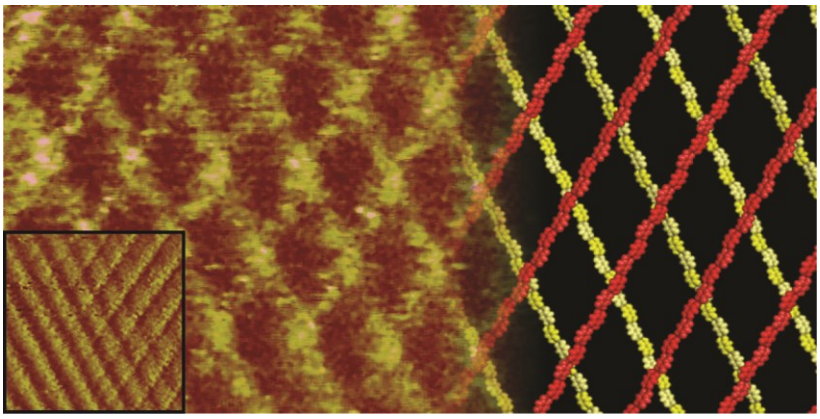

Figure 29. STM double layer topography image of **C18*m*** (left) adsorbed at the TCB/HOPG interface under ambient conditions. Model of the molecular packing of two layers (with alkyl chains removed for clarity; right). The layers are shifted approximately 60° relative to each other. 12.5 nm × 25 nm; I_t = 12.5 pA. V_b = 686.4 mV. Inset: growth of a second layer on top of the first. 20 nm × 20 nm; I_t = 13.3 pA, V_b = 668.4 mV.

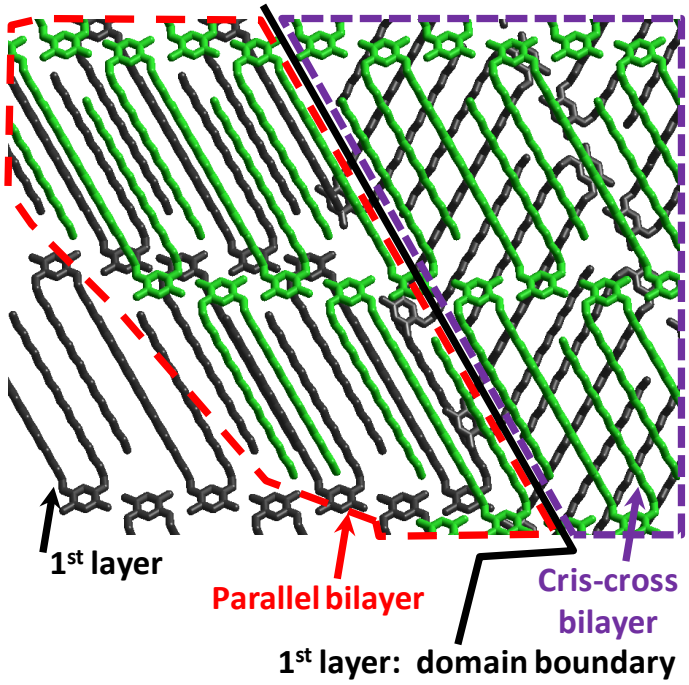

Figure 30. A schematic model illustrating the formation and structure of criss-cross bilayers. This observation suggests that penalties for both breaking intermolecular interactions within the second layer and creating domain boundaries complementary to the layer underneath seems to be higher than the energy difference between parallel and criss-cross interlayer configurations.

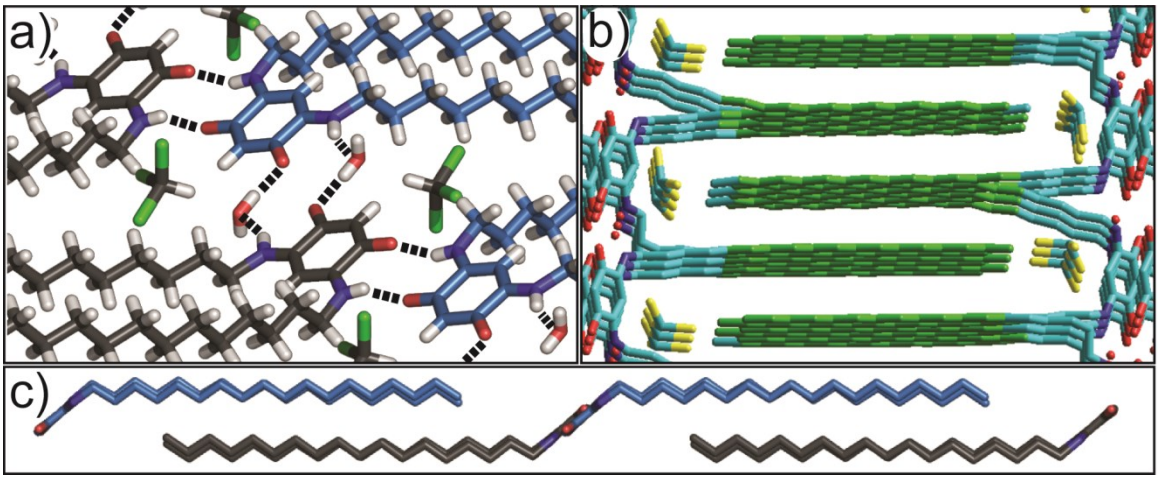

Figure 31. Important substructures of the **C18*m*** crystal structure: (a) hydrogen bonded linear (racemic) zigzags; (b) double-decker layer and (c) parallel packing of alkyl chains belonging to different layers.

Slow evaporation of a chloroform solution of **C18*m*** gave crystals suitable for X-ray diffraction experiments. Despite inclusion of chloroform and water molecules, partially disrupting the original hydrogen bonding, the crystal structure has many important similarities with the proposed model of **C18*m*** surface self-assembly: bent conformation, hydrogen bonding and double-decker packing of alkyl chains into lamellae (**Figure 31**). The (δ+)N–H···O(δ−) distance, a measure of the CAHB, in the 2D packing (*ca.* 3.0 Å) and the crystal structure (2.85 Å) are in close agreement and are in the robust range of N···O distances reported in the literature (2.8-3.3 Å).[95,96] In the crystal structure, the H-bonded zigzags are completely racemic due to the presence of an inversion centre. This inversion is impossible in surface adsorbates,[74] which leads to the observed local chirality in the 2D structure. The orientation of layers in the crystal is defined by maximized interactions between alkyl chains in parallel lamellae in the same way as is expected for an ideal (defect-free) bilayer. The close correspondence of the 2D and 3D arrangements is thus a successful illustration of the usefulness and validity of STM investigations of multilayers for gaining insights into early stages of crystal growth.

2.4. Conclusion

In this work we have addressed various aspects of surface self-assembly of a model *p*-benzoquinonemonoimine **C18*m***, covering structure and interplay of different supramolecular interactions, formation of pseudoracemates and growth of thin films. This work sets a foundation for understanding and applying *p*-benzoquinonemonoimines in supramolecular design. Currently we are investigating surface self-assembly of several other benzoquinonemonoimines and their metal complexes.

2.5. Experimental

2.5.1. Chemicals and Instrumentation

Chemicals 4,6-Diaminoresorcinol dihydrochloride, octadecylamine and 1,2,4-trichlorobenzene were obtained from Aldrich. Ethanol (anhydrous) was obtained from Fisher Scientific. Melting points (m.p.) were recorded with a capillary melting point apparatus (Thomas Hoover). The reported R_f values were determined by a standard thin-layer chromatography (TLC) procedure: 0.25 mm silica gel plates eluted with chloroform/methanol (98:2).

NMR ^{1}H NMR (500 MHz) and ^{13}C NMR (125 MHz) spectra were recorded on a Varian 500 spectrometer at ambient temperature. The residual proton and carbon signals of deuterated $CHCl_3$ were used as internal standards ($CDCl_3$: δ (^{1}H) 7.26 ppm, δ (^{13}C) 77.23 ppm). The following notation is used for the ^{1}H NMR splitting patterns: singlet (s), doublet (d), triplet (t), quartet (q), quintet (p), multiplet (m) and broad signal (br).

MS Mass spectrometric analysis was performed using a Waters Micromass, Quattro LC triple quadrupole mass spectrometer (Waters, Montreal, PQ, Canada). The instrument was operated using an ESI (electrospray ionization) source by direct injection with a syringe pump (50 μL syringe; flow rate: 1 μL/min). The MS instrument was operated in the positive mode (ES+) and the data acquisition/analysis was carried out using Masslynx software version 4.01. Source working conditions were as follows: cone

voltage: 20 V, Capillary voltage: 3.3 V, source temperature: 90 °C, desolvation temperature: 100 °C, desolvation gas flow rate: 220 L/hr, nitrogen: (99.9% purity, from cylinder).

UV-Vis UV-Vis spectra were recorded on an Agilent 8453 UV-Visible spectrophotometer.

STM STM measurements were carried out under ambient conditions with a Bruker Nanoscope MultiMode Scanning Probe Microscope equipped with a low-current STM head or an RHK STM (SPM1000) running under ambient conditions. *In situ* STM imaging was performed at the liquid/solid interface; the substrate was freshly cleaved highly oriented pyrolytic graphite (HOPG; ZYB quality; NT-MDT Castletroy, Limerick, Ireland). Mechanically sharpened Pt/Ir (90/10 or 80/20; NanoScience Instruments, Phoenex, AZ) tips were tested by obtaining atomic resolution images of graphite and subsequently a drop (*ca.* 5 μL) of **C18m** in 1,2,4-trichlorobenzene was added. Self-assembled monolayers (SAMs) were observed immediate after the tip was engaged. The concentration of **C18m** was typically close to saturation, but lower concentrations also led to the same molecular packing.

The specific tunneling conditions are given in the figure captions. All images were flattened and Gaussian smoothed using WSxM[1] software and the images in **Figure 26** and **Figure 27** have been lattice-corrected for distortion due to drift. All other images were flattened and median filtered using the Nanoscope 6.14r2 software. The unit cell of **C18m** was measured based on 17 lattice-corrected images and the overall error in the unit cell was determined to be below 4%.

2.5.2. Synthesis and characterization of C18*m*

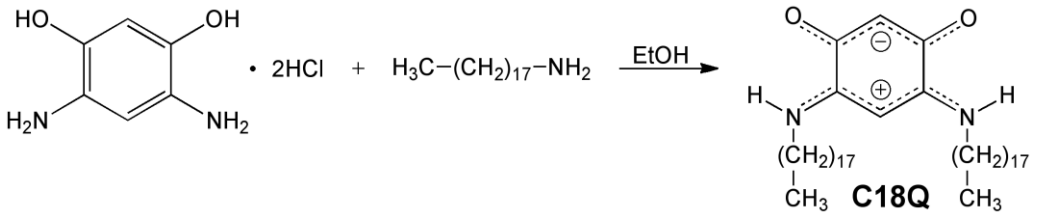

4,6-Diaminoresorcinol dihydrochloride (110.4 mg; 0.518 mmol) was dispersed in ethanol (7 mL) and after 2 min. octadecylamine (1.1014 g; 4.086 mmol) was added to the stirred solution. The mixture was left to stir for *ca.* one day. The resulting dark green precipitate was isolated by vacuum filtration on filter paper, washed with cold ethanol and air-dried. The crude product was purified by centrifugal chromatography on silica (98/2 chloroform/methanol) and dried under vacuum (259.7 mg; 0.404 mmol; 78%). Single crystals suitable for X-ray diffraction were obtained by slow evaporation from $CDCl_3$. m.p. 105.5-107.0 °C; R_f 0.35 (98/2 $CHCl_3$/MeOH); ^{1}H NMR (500 MHz, $CDCl_3$) δ 0.88 (t, ^{3}J = 7.0 Hz, 6H, CH_3), 1.26 (m, 56H, CH_2-C*H*$_2$-CH_2), 1.73 (p, ^{3}J = 7.3 Hz, 4H, NH-CH_2-C*H*$_2$), 3.37 (dt, ^{3}J = 6.7 Hz, 4H, NH-C*H*$_2$), 5.13 (s, 1H, NH-C-C*H*), 5.44 (s, 1H, O-C-C*H*), 8.32 (br s, 2H, N*H*); ^{13}C NMR (125 MHz, $CDCl_3$): δ 14.08 (CH_3), 22.66, 26.92, 28.27, 29.14, 29.33, 29.41, 29.52, 29.60, 29.63, 29.67, 31.90, 43.30, 80.53 (N-C-*C*), 98.81 (O-C-*C*), 156.61 (N-*C*), 172.33 (O-*C*); UV-Vis: λ 337 (log ε = 4.41), 350 (log ε = 4.43); MS (Triple Quad-ESI): m/z: 643.65 $[M+H]^+$ calcd $[M+H]^+$: 644.61

2.6. Acknowledgements

We thank Nadime Salamé for assistance in the characterization of **C18*m*** and Charles F. Campana for assistance in refining the crystallographic data of **C18*m***. NSERC, FQRNT, CFI, Concordia University and the German Science Foundation ("Deutsche Forschungsgemeinschaft") for funding within the Research Center 569 („Sonderforschungsbereich 569"). O.I. is grateful to FWO (the Fund of Scientific Research- Flanders) for a post-doctoral fellowship. We also acknowledge our

membership in the FQRNT-supported, multi-university Centre for Self-Assembled Chemical Structures (CSACS).

2.7. Notes

X-ray structural and crystallographic data (CCDC-830819; Chapter 6. Appendix I)

Chapter 3.

Influence of Alkyl Chain Length, Hydrogen Bonding, Constitutional Geometry and Metal Complexation on the 2D and 3D Self-Assembly of Aminoquinone Derivatives

Yuan Fang, Oleksandr Ivasenko, Shernlong Lee, Mihaela Cibian, Garry S. Hanan, Olivier Siri, and Louis A. Cuccia

3.1. Abstract

It is well accepted that the processes of molecular assembly are governed by a delicate balance of molecule-molecule and molecule-substrate interactions. However, systematic studies of the subject are relatively rare. Here, aminoquinone derivatives (zwitterionic *meta*-diaminobenzoquinones (**C18*m*** & **C22*m***), *para*-aminobenzoquinones (**C18*p***) and the 2:1 metal complex of **C18*m*** with Ni(II), **(C18*m*)$_2$Ni**), were exploited as a model system to investigate the effect of alkyl chain length, hydrogen bonding, constitutional geometry and metal complexation of molecules upon their 2D and 3D self-assembly behavior on graphite. These interactions lead to various self-assembled patterns of molecules on the surface as revealed using scanning tunneling microscopy. Such patterns can be explained very well in terms of the strength of intermolecular interactions among molecules and the adsorption energy of the molecules on graphite.

3.2. Introduction

The construction of organic semiconductor materials on solid surfaces with well-ordered 2D and 3D structures has attracted considerable attention in nanotechnology and materials science.[52,56,97,98] Controlled organization of molecules is expected to be highly applicable for surface functionalization and design of molecule-based devices.[99] A variety of methods have been developed to pattern molecules on surfaces.[100] Among these, a prominent one is molecular self-assembly.[101,102] The approach is referred to as the 'bottom-up' strategy and when applied to surfaces, typically involves non-covalent and reversible interactions between adsorbate-adsorbate and adsorbate-substrate.[74] These interactions are, for example, hydrogen-bonding, van der Waals, π-π, electrostatic, dipolar and metal coordination interactions. The variety in functional groups and their interactions drive non-covalent intermolecular bonds and form the basis of supramolecular chemistry.[103]

Over the past several years, we have witnessed a rapid growth in surface-based supramolecular chemistry.[104] On the one hand, the field is still waiting for various

compounds with novel functions or potential advantages in applications such as decreased feature size and enhanced device efficiency. On the other hand, a deeper understanding of specific classes of molecules and their analogues or derivatives with respect to their ability to self-assemble is of fundamental importance.[105]

We have particular interests in the study of quinonoid molecules because of the important role of numerous quinonoid compounds in nature and, moreover, because of their unique charge-transfer properties. More specifically our interest lies with aminobenzoquinones, which have been widely explored for biological applications, especially in medicinal chemistry. For example, some have anticancer and antimalarial properties.[106–108] Recently, we have studied the charge-assisted hydrogen bond-directed self-assembly of a zwitterionic benzoquinonemonoimine (**C18*m***) using scanning tunneling microscopy (STM) at the liquid-solid interface.[109]

Herein, we strategically designed a series of aminobenzoquinone derivatives, (**C18*m***, **C22*m***, **C18*p*** and **(C18*m*)$_2$Ni**; **Figure 32)**, and investigated their self-assembly behavior using STM. We systematically discuss the effect of alkyl chain length, constitutional geometry and metal complexation as well as hydrogen bonding on their molecular self-assembly.

There are several reasons to investigate these molecules. Hydrogen-bonding interactions are arguably the most widely exploited force in molecular assembly due to their strength, directionality and reversibility.[23] Thus, all of these molecules are designed to exploit their hydrogen bonding interactions when they self-assemble into 2D patterns on graphite. The difference between **C18*m*** and **C22*m*** is the length of the alkyl chains. Long alkyl chains have been widely applied in 2D self-assembly, since they help stabilize and increase the physisorption of molecules on surfaces. Thus, it is envisaged that the interplay between hydrogen bonding and van der Waals interaction in the self-assembly of these molecules can influence surface molecular patterning.

For surface patterning, modification and device setup, Braunstein *et al.* have employed zwitterionic benzoquinonemonoimines to alter static dipoles on surfaces taking

advantage of their large intrinsic electrical dipole (*ca.* 10 Debye), a result of their zwitterionic character. It was proposed that these n-type conductive molecular films could play an important role in organic electronic devices.[110] Firstly, charge-assisted hydrogen bonding may allow these molecules to self-assemble into extended networks on a surface.[109,111] Secondly, zwitterionic benzoquinonemonoimines may exist in a film where π-stacking may allow for conductivity perpendicular to the plane of the quinoidal core while hydrogen bonding may allow for in-plane conductivity.[110] In addition to the π-stacking channels of a film, for electron transport, the so-called cross-junction structure of a film can also be considered as conductive pathways.[112]

(C18*m*)$_2$Ni is an N,O ligand suitable for metal coordination. It is expected that non-covalent coordination compounds and networks may provide a new dimension towards nanostructured materials with novel functions.[111] Indeed, for the past several years the study of the supramolecular properties and coordination chemistry of quinonoid molecules has appeared based on their potential applications, including homogenous catalysis and molecular electronics.[113] Recently, new chelating N,O ligands have been synthesized and have been shown to have very high catalytic activity.[114] Aminoquiones provide an alternative for N,O type ligands other than ligands such as porphyrin dimers and oligomers.[114] In 2005, Yang *et al.* synthesized a novel family of zwitterionic benzoquinonemonoimine derivatives and their metal complexes,[87] based on which we synthesised **(C18*m*)$_2$Ni** for comparison (**Figure 32**). Apart from the viewpoint of potential applications of zwitterionic benzoquinonemonoimine nickel complexes, to date attempts to prepare crystals of related square planar nickel complexes for X-ray crystallography have not been successful. Thus, the visualization of **(C18*m*)$_2$Ni** by STM is of particular importance. For the above-mentioned reasons, this systematic STM study of a family of aminobenzoquinone derivatives should merit special attention.

3.3. Results and Discussion

We have previously addressed various aspects of surface self-assembly of a model *p*-benzoquinonemonoimine, **C18*m***, directed by charge-assisted hydrogen bonding

(CAHB) coupled with an unusual double-decker packing of the alkyl chains in interdigitated lamellae.[109] Herein, for comparison we introduce three related molecules (**Figure 32**): (*i*) a zwitterionic *p*-benzoquinonemonoimine, **C22*m***, which has longer alkyl chains, (*ii*) an isomer of **C18*m***, 2,5-di(octadecylamino)1,4-quinone, with *para* orientation of the identical groups, **C18*p*** and (*iii*) a metal coordinated dimer of **C18*m***, **(C18*m*)$_2$Ni**. These four compounds are investigated in order to study the effect of alkyl chain length, substitution position and metal coordination on the self-assembly process at the liquid/solid interface.

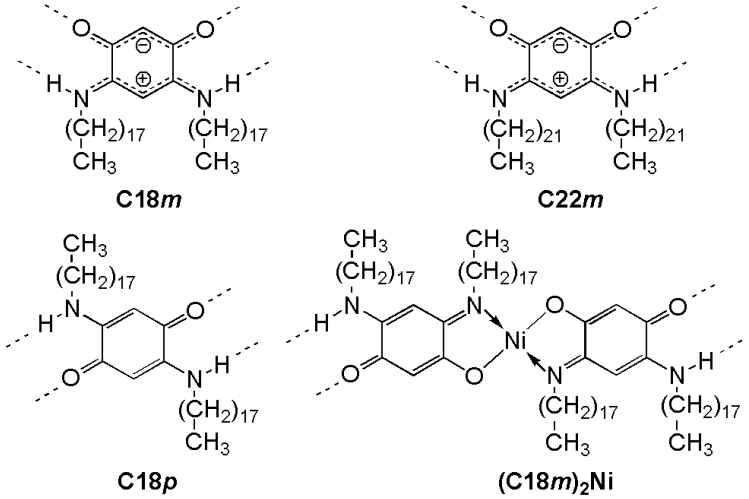

Figure 32. Chemical structures of **C18*m***, **C22*m***, **C18*p***, and **(C18*m*)$_2$Ni**.

C22*m* has four additional carbons on both alkyl chains as compared to **C18*m***. Initially, one might expect that the self-assembly behaviour of **C22*m*** similarly to **C18*m***, with pseudoracemic double-decker packing as shown in **Figure 33**.[36] For **C18*m***, both head groups and alkyl chains follow the main symmetry axes of graphite. In other words, the alkyl chains tilt 60° with respect to the head group rows. From the unit-cell measurements and careful analysis of STM images (**Figure 33**), the head group and alkyl chain ratio is 2:3, which indicates that one out of four alkyl chains of **C18*m*** is not absorbed directly on the graphite surface. The alkyl chains may either point up into the solution (**Figure 33, b & c**) or overlap on top of other alkyl chains (**Figure 33, d & e**). Note that double decker packing is distinct from double-layer packing. In the double

decker packing, there is only partial overlap of the alkyl chain regions and there is no overlapping of the head group region. A more detailed description of **C18*m*** packing can be found in Chapter 2.

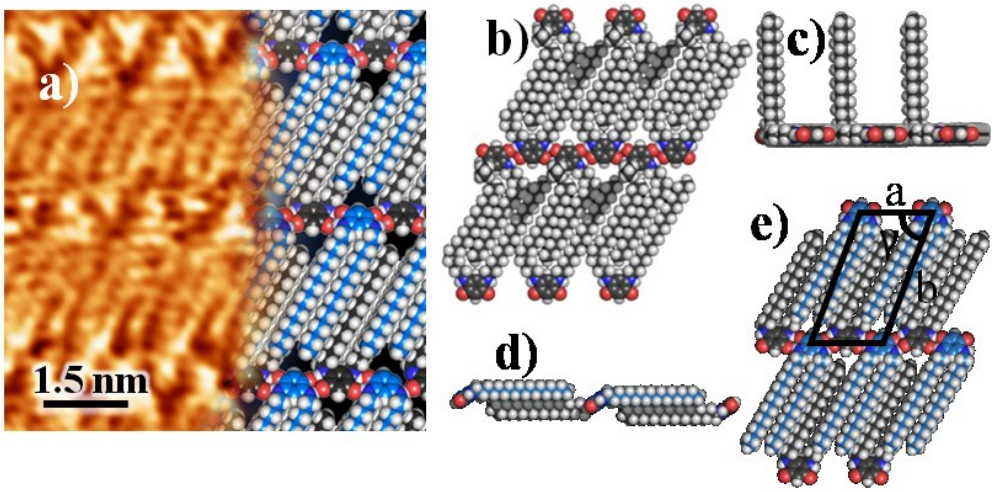

Figure 33. (a) STM topography images (left) and model (right) of **C18*m*** at the TCB/HOPG interface. (a = 14.8 Å, b = 29.4 Å and γ = 79°). 6 nm × 6 nm; I_t = 25 pA, V_b = -150 mV. b, c) & d, e) are two tentative models for the packing structure of **C18*m***. c) side view of b) and d) side view of e).

In addition to the **C18*m***-like morphology, **C22*m*** forms two additional morphologies. The three morphologies of **C22*m*** are type 1 (**Figure 34a**, the **C18*m***-like morphology), type 2 (**Figure 34b**) and type 3 (**Figure 34c, d & e**). The type 2 morphology of **C22*m*** is the most prominent morphology, where the alkyl chain tilt is 86° with respect to the head group row (**Table 1**). Type 2 morphology dominates with a *ca.* 70% coverage on HOPG. Unlike type 1, in type 2 morphology of **C22*m***, there are 7 out of 8 alkyl chains adsorbed on the HOPG (**Figure 34b**). Recall that type 2 morphology has an 86° angle between alkyl chains and head group rows, while for type 1 morphology the tilt angle is 60°. The decreasing tilt angle and the increasing in hydrogen bonding distance (based on STM image analysis; **Table 1)** allow an additional alkyl chain to adsorb on the HOPG surface. The adsorption of more alkyl chains of **C22*m*** on the surface increases stability and is likely responsible for the prevalence of type 2 morphology for **C22*m*** on HOPG.

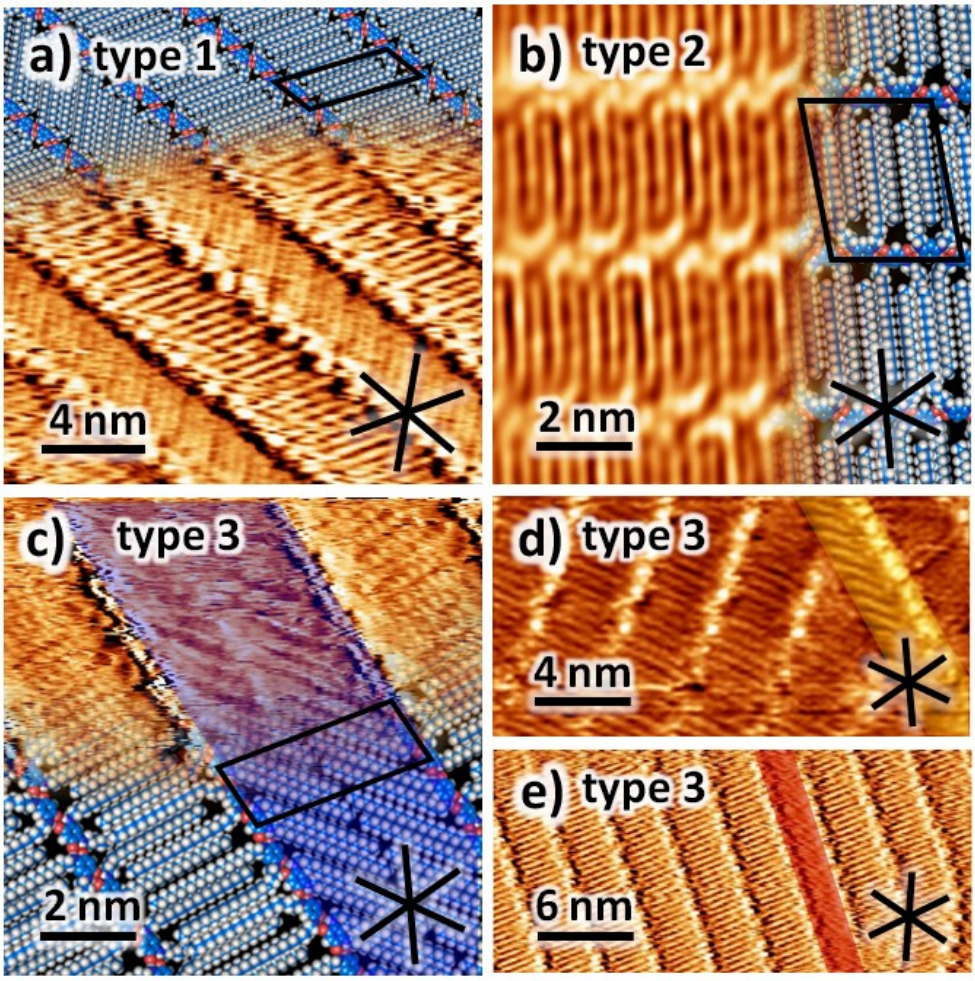

Figure 34. Three different packing morphologies of **C22*m***; the three main axes of graphite are highlighted by black lines. a) type 1 (packing model upper and STM topography image lower); alkyl chain head group angle 60˚; unit cell: a_1 = 14.8 ± 0.4 Å, b_1 = 34.1 ± 0.3 Å and γ = 75 ± 1˚; I_t = 20 pA, V_b = -50 mV. b) type 2 (STM topography image left and packing model right); alkyl chain head group angle 86˚; unit cell: a = 30.1 ± 0.8 Å, b = 36.6 ± 0.3 Å and γ = 76 ± 1˚) I_t = 13.0 pA, V_b = -92 mV. c, d & e) type 3 highlighted in blue yellow and red; alkyl chain head group angle 34˚ unit cell: a = 15.1 ± 0.4 Å, b = 40.8 ± 0.3 Å and γ_1 = 75 ± 1˚; c) I_t = 20 pA, V_b = -856 mV. ; d) I_t = 25 pA, V_b = -313 mV. e) I_t = 22 pA, V_b = -47 mV.

Different head group to alkyl chain ratios were observed for the 2D packing of **C22*m*** (**Figure 34**). Type 1 (**Figure 34a**) and type 2 (**Figure 34b**) morphologies have head group to alkyl chain ratios of 3:4 and 4:7, respectively. Type 3 morphology occurs

very rarely and was only observed as single rows within type 2 morphology domains (**Figure 34 c, d, & e**). It has an alkyl chain and head group row tilt angle of 34°. The alkyl chains have a separation of 0.42 nm, which lies within the preferred alkyl chain separation range (0.4-0.55 nm).[89] The alkyl chain tilt with respect to the head group row is given in **Table 1**.

Table 1. Packing parameters of aminobenzoquinone derivatives.

	Alkyl chain tilt with respect to the head group row	Alkyl chain distance (nm)	Unit cell 'a' (nm)
C18m	60	0.427	1.479
C22m type 1	60	0.428	1.481
C22m type 2	86	0.427	1.507×2
C22m type 3	34	0.419	1.507
C18mNi	66	0.460	1.509
C18p	43	0.508	0.745

Type 3 morphology of **C22*m*** was observed in three cases: In case I, alkyl chains are non-interdigitated (**Figure 34c**, highlighted in blue). In case II, there is only one row of alkyl chains that lies at a domain boundary of type 2 morphology (**Figure 34d**, highlighted in yellow). It is believed that this morphology acts to stabilize the edge of a second layer of type 2 morphology (right) on top of an underlying type 2 morphology (left). This is the case because the alkyl chains of the case II (type 3) morphology have the same orientation as the underlying type 2 morphology. It should be noted that there are varying degrees of alkyl chain overlap due to the overall orientation of the top layer. In case III of type 3 morphology (**Figure 34e**), the alkyl chains are either fully overlapped or half the alkyl chains are pointing up into the solution.

For all these morphologies, the head groups of **C22*m*** adopt a zigzag arrangement, which is similar to the charge-assisted hydrogen bonding motif of **C18*m***. The favorable van der Waals interactions between the alkyl chains and the HOPG offset the expense of the slightly longer H-bond distance (**Table 1**). This example shows the fine balance

between van der Waals and H-bond interactions. A ripening process from the 60° domain (type 1) to the 86° domain (type 2) observed in consecutive STM images indicates that the more prominent 86° domain is thermodynamically more stable than the 60° domain. (**Figure 35**).

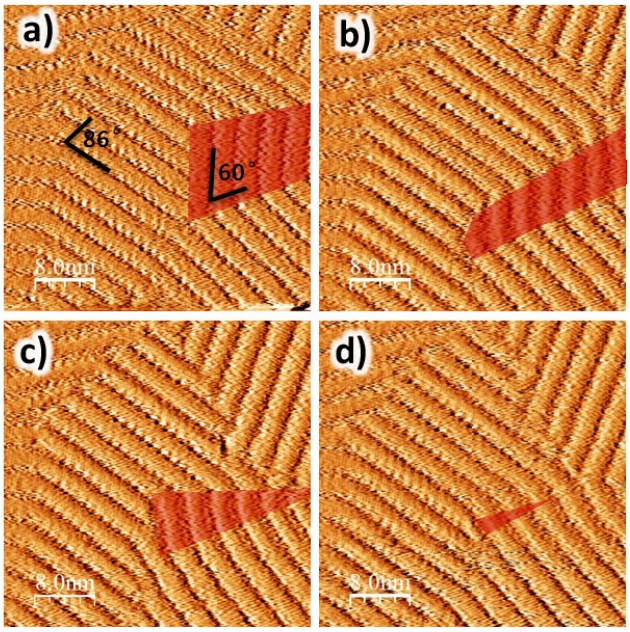

Figure 35. Consecutive STM images revealing the ripening process of a phase transition from type 1 to type 2 packing at the TCB/HOPG interface at room temperature. Domains of type 1 are heighted in red; I_t = 20 pA, V_b = -50 mV.

Unexpected interruptions in the CAHB are sometimes observed in type 2 morphology of **C22*m***. In Figure 36, a gap in the head group region is highlighted with black arrows. The hydrogen bonding is broken by an adsorption of an additional alkyl chain of **C22*m***. Specifically, instead of seven alkyl chains of four **C22*m*** molecules, all eight of the alkyl chains were adsorbed on graphite. This one extra adsorbed alkyl chain stretches the head group row and literally breaks one CAHB. The adsorption energy for every methylene group is 0.5 kcal/mol[45] and the binding energy of the CAHB is *ca.* 2 x 15.6 kcal/mol.[109] An adsorption of an extra 22 carbon long alkyl chain on the surface results in a gain of *ca.* 11 kcal/mol. The fact that the gained energy is lower than that of

the binding energy of the CAHB is in agreement with why this CAHB cleavage is relatively rare. We have shown that the extension of four extra carbons on each chain of **C18*m***, namely **C22*m***, can alter the supramolecular packing on HOPG. These results suggest that the collective strength of van der Waals interactions can override strong hydrogen bonding interactions. To the best of our knowledge, this is the first explicit example where alkyl chain packing is able to break H-bonding, more specifically a strong CAHB.

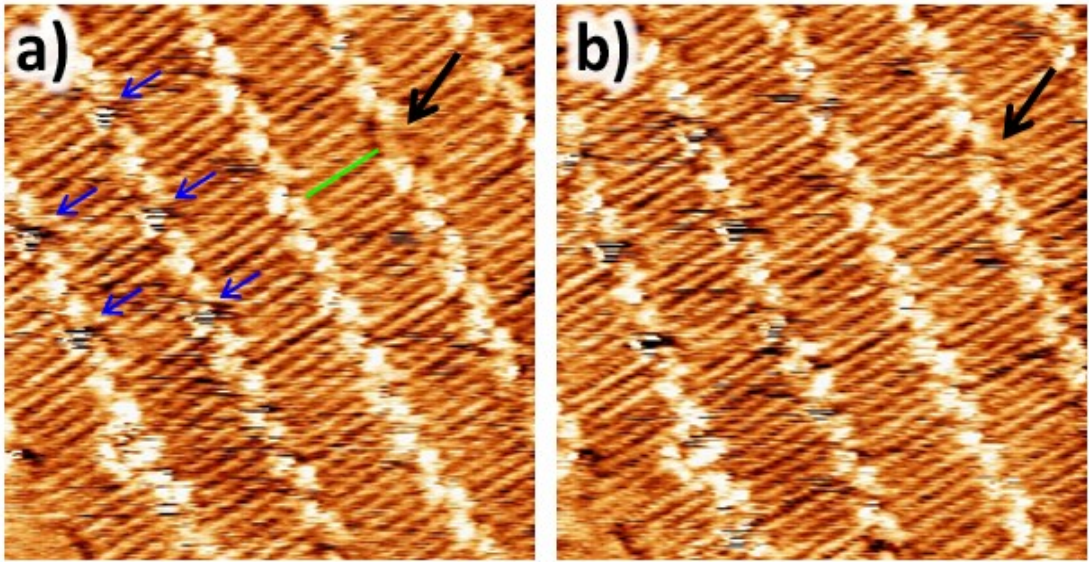

Figure 36. Unexpected breakage in a CAHB observed in type 2 morphology of **C22*m***. The black arrow points towards the broken CAHB and the green lines highlight where the additional alkyl chain is adsorbed. a & b are two consecutive images showing noticeable 'noise' stripes on every fourth head group of type 2 packing for **C22*m*** highlighted by blue arrows. I_t = 13 pA, V_b = -92 mV.

In Figure 36, it is interesting to note that some black noise lines with regular periodicity appear on top of head groups of **C22*m***. More importantly they are observable in the same location during several scans. Figure 36 a & b are two consecutive images (both scan down direction) where the noise stripes appear at the same positions. Examining the images more carefully, the noisy head groups or 'streaked' heads[115] appear every fourth head group of **C22*m***. This could be explained by two possibilities: (*i*) every

8th alkyl chain overlaps on top of another alkyl chain causing every 4th head group to slightly tilt away from the plane of HOPG or (*ii*) every 8th observed alkyl chain extends into the solution and the 'noise' is observed when the STM tip interacts with the flying alkyl chain during the scanning.

For **C18*p*,** non-interdigitated monolayer packing was observed. Based on unit cell measurements, all alkyl chains are fully extended and adsorbed on HOPG (**Figure 37a**). **C18*p*** forms large extended domains that usually extend until the end of graphite terraces.

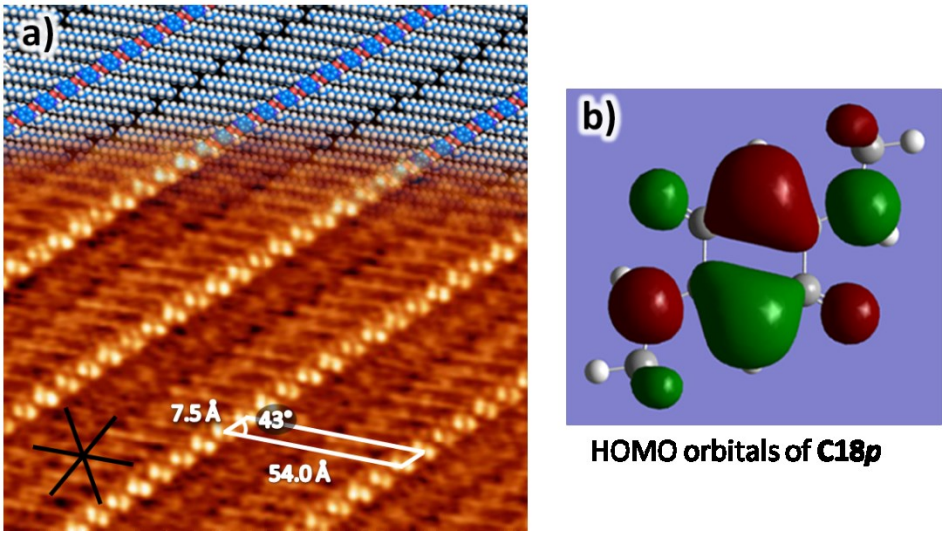

Figure 37. a) STM topography image of **C18*p***; b) HOMO orbitals of **C18*p***. I_t = 16 pA, V_b = -200 mV; alkyl chain head group angle 43˚; a = 7.4 ± 0.4 Å, b = 54.0 ± 0.5 Å and γ = 43 ± 1˚.

For **C18*p*** only linear structures were observed (**Figure 37a**). On the other hand, for **C22*m*** type 1, both herringbone and linear structures were observed (**Figure 37a**). The angle between the head group rows and the alkyl chains of **C18*p*** is 43° and the head group rows of **C18*p*** do not follow one of the main axes of graphite. The head group rows of **C22*m*** type 1 follow one of the main axes of graphite, and the alkyl chains can follow either one of the two other axes of graphite. As a result both herringbone and linear structures were observed and both packing motifs are expected to have the same energy.

On the other hand, since the head group rows of **C18*p*** do not follow the graphite, the alkyl chains can follow any one of the three main axes of the underlying graphite. As a result, there will be an energy difference between the linear and herringbone arrangement.

The switch in position of the N and O groups allows the **C18*p*** head group to pack in a linear fashion, rather than the zigzag motif observed for in **C18*m*** and **C22*m***. Although STM cannot directly identify atoms with chemical specificity, it is able to distinguish between some functional groups. For example, the **C18*p*** head group rows appear as bright regions, while alkyl chains are less bright (**Figure 37a**). Another feature noticed in **Figure 37** is that two spots were observed for the head group of **C18*p***. This can be due to: (*i*) the contrast of N being more bright than that of O, so the two bright spots might be N,[55] or (*ii*) the HOMO of the **C18*p*** head group was visualized. Since the image is taken at negative bias, electron movement from the HOMO of the SAM to the STM tip is preferred. In Figure 37b, the HOMO orbital geometry of a shorter chain *para* compound, **C1*p***, was optimized using Gaussian 09 M06-2X/6-31G* method. The orbitals can be made to resemble the observed STM image.

Similar to **C18*m***, **(C18*m*)$_2$Ni** forms stripe-like packing. The repeat distance of the stripes was measured to be 28.1 Å with an angle between the alkyl chains and head group rows of 66.1° ± 0.9°, indicating that **(C18*m*)$_2$Ni** alkyl chains are fully extended and interdigitate with the neighboring rows. The results are very similar to the double decker motif of **C18*m*** (**Figure 38**).

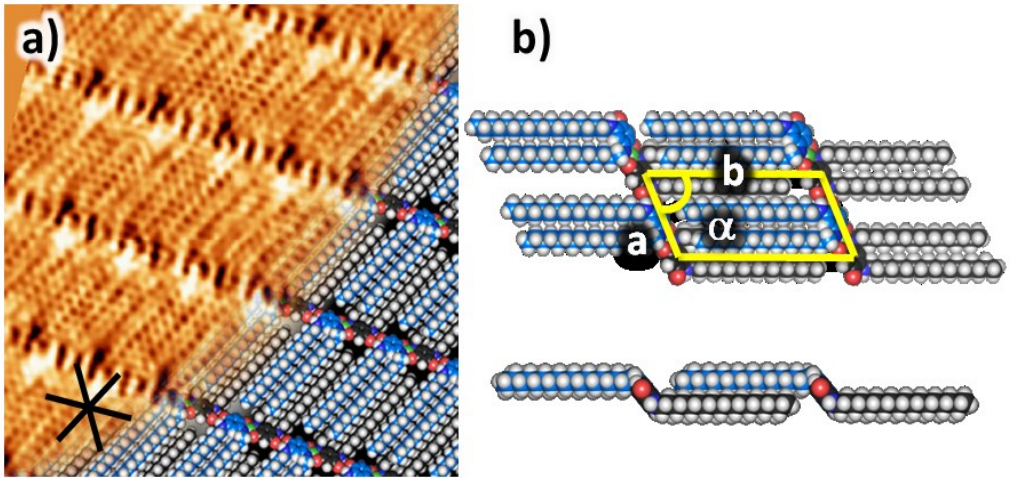

Figure 38. a) STM current image (left) and packing model (right) of **(C18*m*)$_2$Ni**, b) top view and side view packing model. The yellow box shows the unit cell (a = 15.1 ± 0.2 Å, b = 30.7 ± 0.5 Å and γ = 66 ± 1˚). I_t = 26 pA, V_b = -800 mV.

The difference between the repeat distance between **C18*m*** and **(C18*m*)$_2$Ni** is due to the angle between the head group rows and alkyl chains. As expected, the measured unit cell width of **(C18*m*)$_2$Ni**, 15.1 Å, is slightly longer than that of **C18*m***, 14.8 Å. Since a Ni atom is added into the packing of the head group rows, this leads to a stretched zigzag pattern. In other words, a ligand-Ni-ligand bond replaces every second ligand-ligand hydrogen-bonding interaction. The two motifs have a similar distance. Therefore, the difference between the unit cell's 'a' parameter is almost indistinguishable. **(C18*m*)$_2$Ni** also adopts a double decker packing similar to that of **C18*m***. The width of the unit cell after multiplying by sin(66.1) is 13.8 Å. There is not enough space for the adsorption of four alkyl chains on HOPG, since the minimum spacing between neighbouring alkyl chains is *ca.* 4.2 Å.[89] This is in agreement with the observed ratio between head groups and alkyl chains of 1.5 in the packing of **C18*m***, indicating that for **(C18*m*)$_2$Ni**, every one pair of ligands and one Ni atom, one alkyl chain is 'missing'.

The submolecular STM image also gives us evidence for a *trans* configuration of the metal complex. It is difficult to prove the *trans*-geometry of these complexes due to the absence of a crystal structure of related *meta*-aminobenzoquinone square planar

nickel complexes. However it is believed that **(Cn*m*)$_2$Ni** adopts an N,O,N,O trans-geometry since the *trans*-geometry is the less sterically hindered conformation. To support this hypothesis, the visualization of **(C18*m*)$_2$Ni** by STM is of particular importance.

Based on STM image analysis, it was found that alkyl chain spacing for **C18*m***, **C22*m***, and **(C18*m*)$_2$Ni** are similar. However, these alkyl chain spacings differ from that of **C18*p*** (**Table 1**). Further experiments and modelling are required to explain this difference in alkyl chain spacing.

Achiral molecules can adopt a chiral conformation when adsorbed on a surface. As such, chiral domains are often observed in the self-assembly of achiral molecules.[116] Due to the presence of the 3 main symmetry axes of HOPG, a total of 6 domain orientations can be found. That is, 3 domains rotate clockwise and 3 domains rotate counterclockwise with respect to the 3 main axes of graphite (*i.e.* there are 3 pairs of mirror image domains).

Two exceptions are when the head group row lies parallel to either the main or the sub axes of HOPG. In these two cases, only 3 domain orientations are observed. In molecules with alkyl chains, if the head group row occupies one of the main axes of graphite, the chains can only follow one of the remaining two axes of graphite. An example of this is **C18*m***, where the head group rows follow on a main axis of graphite and the alkyl chain randomly choose to follow one of the two remaining graphite axes, resulting in the formation of either a linear or herringbone structure (**Figure 26**), and the resulting domain is pseudoracemic. On the other hand, the head group row of all the other molecules, **C18*p***, **(C18*m*)$_2$Ni** and **C22*m*** (type 2 and type 3 morphologies), do not follow one of the main symmetry axes of HOPG and mirror chiral domains are formed with equal probability. (**Figure 39**)

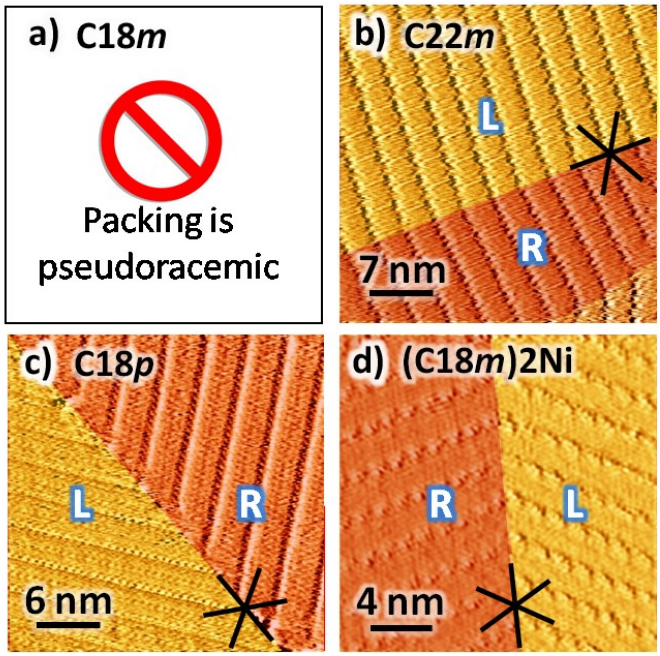

Figure 39. a) **C18*m*** Form a pseudoracemic packing; b, c, d) left or right mirror image domains highlighted by yellow and red color of **C22*m***, **C18*p***, **(C18*m*)$_2$Ni**, respectively. Image conditions: b) I_t = 22 pA, V_b = -47 mV; c) I_t = 17 pA, V_b = -300 mV; d) I_t = 13 pA, V_b = -293 mV.

Type 1 morphology of **C22*m*** does not have mirror domains since the head group row follows one of the axes of graphite. Morphologies 2 of C22*m* does form mirror image domains since the head group row has a 26° shift with respect to one of the graphite axes (**Figure 39b**). For **C18*p***, the shift of the head group row and the HOPG is 13° and mirror image domains were observed (**Figure 39c**). similarly, for **(C18*m*)$_2$Ni** the shift between head group rows and one of the axes of graphite is 6° and mirror image domins were once again observed. (**Figure 39d**)

In addition to the successful visualization of the self-assembled monolayers of these amonobenzoquinone derivatives, we also observed well-ordered multilayers of these compounds using STM. For all the systems, multilayers can form from saturated concentrations (**Figure 40**).

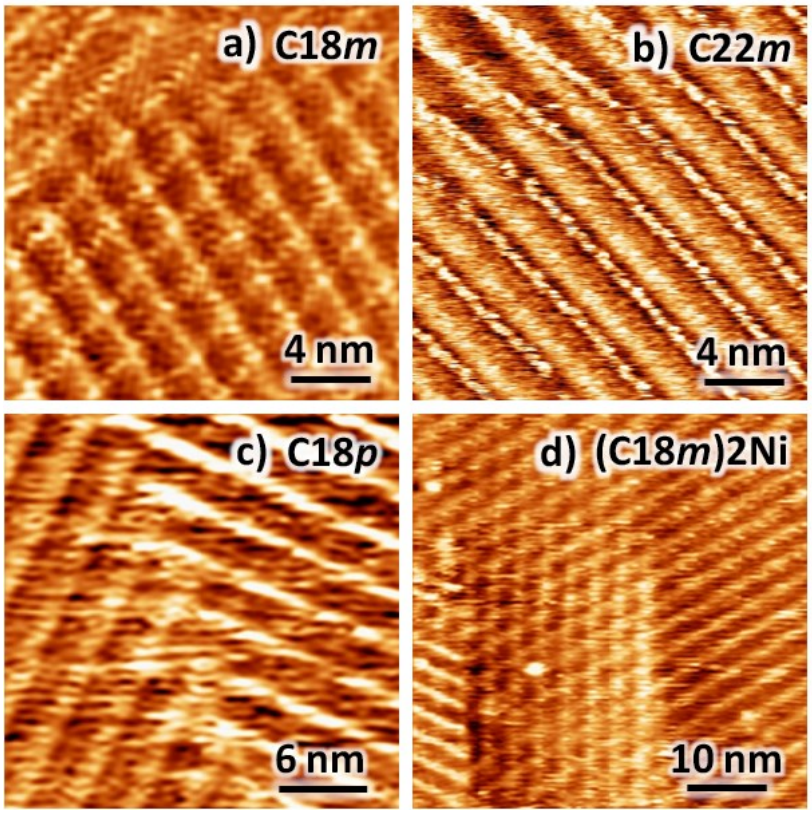

Figure 40. Multilayers were observed for all four molecules; a) I_t = 12 pA, V_b = 686 mV. b) I_t = 26 pA, V_b = 528 mV. c) I_t = 20 pA, V_b = 600 mV. d) I_t = 30 pA, V_b = -1753 mV.

These molecules all tend to form multilayers in a criss-cross and parallel fashion. We ascribe this phenomenon to strong intermolecular interactions which 'link' them to pack into stripe-like patterns on HOPG. These stripe-like self-assembled rows could deposit directly on the surface or from solution *via* intermolecular interactions. It is most likely that the second layer forms in the similar fashion as the first layer. This is likely the case since orientation of the upper layer is governed by the orientation of the underlying layer. As a result, these hierarchical frameworks appear with criss-cross or parallel features. Note that these observations are not due to a double-tip artifact since they are observed using different tips and in several experimental sessions with both criss-cross and parallel arrangements.

3.4. Conclusions

We have synthesized aminobenzoquinone derivatives including **C18*m***, **C22*m***, **C18*p*** and **(C18*m*)$_2$Ni** and using these compounds, we have set up a model system and discussed how the functional groups of molecules influence their self-assembly on HOPG using STM. The resulting self-assembled motifs are well explained by the strength of intermolecular interactions among molecules and the adsorption energy of the molecules on graphite. This study provides general guidelines for the formation of specific molecular motifs with a variety of molecules, which sheds light on the ability to establish predictable molecular self-assembly *via* constitutional isomerism.

3.5. Experimental Section

3.5.1. Chemicals and Instrumentation:

Chemicals 4,6-Diaminoresorcinol dihydrochloride, palladium on activated carbon, bromodocosane, hexadecyltrimethylammonium bromide, deuterated chloroform, and 1,2,4-trichlorobenzene were obtained from Aldrich. Chloroform, ethyl acetate, ethanol, hexanes and methanol were obtained from Fisher Scientific. Toluene was obtained from J.T. Baker. Nickel(II) acetate tetrahydrate ($Ni(OAc)_2 \bullet 4H_2O$) was obtained from BDH Chemicals. Melting points (m.p.) were recorded with a capillary melting point apparatus (Thomas Hoover). The recorded R_f values were determined by a standard thin-layer chromatography (TLC) procedure: 0.25 mm silica gel plates (Aldrich, 122785-25EA) eluted with chloroform/methanol (98:2).

NMR ^{1}H NMR (300 MHz) and ^{13}C NMR (75 MHz) spectra were recorded on a Varian 300 MHz spectrometer for 1-azidodocosane and docosan-1-amine at ambient temperature. ^{1}H NMR (500 MHz) and ^{13}C NMR (125 MHz) spectra were recorded on a Varian 500 spectrometer at ambient temperature for **C18*m*, C22*m*** and **C18*p*** or 45 °C for **(C18*m*)$_2$Ni**. The residual proton signals of the deuterated solvents were used as internal standards ($CDCl_3$: δ (^{1}H) 7.26 ppm, δ (^{13}C) 77.23 ppm; the following notation is used for the ^{1}H

NMR splitting patterns: singlet (s), doublet (d), triplet (t), quartet (q), multiplet (m) and broad signal (br).

MS For compounds **C18*m*** and **C18*p***, mass spectrometric analysis was performed using a Waters Micromass, Quattro LC triple quadrupole mass spectrometer (Waters, Montreal, PQ, Canada). The instrument was operated using an ESI (electrospray ionization) source by direct injection with a syringe pump (50 μL syringe; flow rate: 1 μL/min). The MS instrument was operated in the positive mode (ES+) and the data acquisition/analysis was carried out using Masslynx software version 4.01. Source working conditions were as follows: cone voltage: 20 V, Capillary voltage: 3.3 V, source temperature: 90 °C, desolvation temperature: 100 °C, desolvation gas flow rate: 220 L/hr, nitrogen: (99.9% purity, from cylinder). Mass spectrometric analysis of individual compounds: **C18*m*** and **C18*p*** (1 mg) was dissolved in acetonitrile/water (1:1; 100 mL). Prior to MS analysis, 1 mL of this solution was further diluted into acetonitrile/water (1:1; 10 mL) and formic acid (10 μL) was added.

For compounds $C22NH_2$ and **C22*m***, low resolution mass measurements were performed on a LC-MSD-Tof instrument from Agilent Technologies in positive electrospray. Aliquots of 0.1 uL were injected into the mass spectrometer using a 0.5 mL/min flow of 75% methanol/ 25% water mixture. The capillary voltage was set at 3000 V and mass spectra were acquired from 100 to 1000 m/z. Both the protonated molecular ions $[M+H]^+$ and the sodium adduct $[M+Na]^+$ were used for empirical formula confirmation.

For **(C18*m*)$_2$Ni**, mass measurements were performed on Bruker Ultraflex MALDI TOF/TOF Mass Spectrometer. MALDI was used as ionization method, with dithranol as matrix, in reflector mode. The protonated molecular ion $[M]^+$ was used for empirical formula confirmation.

STM STM measurements were carried out under ambient conditions with a Bruker Nanoscope MultiMode Scanning Probe Microscope equipped with a low-current STM head or an RHK STM (SPM1000) with a Nanoscope IIIa controller, running under ambient conditions. *In situ* STM imaging was performed at the liquid/solid interface; the

substrate was freshly cleaved highly oriented pyrolytic graphite (HOPG; ZYB quality; NT-MDT Castletroy, Limerick, Ireland). Mechanically sharpened Pt/Ir (90/10); NanoScience Instruments, Phoenex, AZ) tips were tested by obtaining atomic resolution images of graphite and subsequently a drop (*ca.* 5 μL) of the molecule of interest in 1,2,4-trichlorobenzene was added on the substrate. Solutions of **C18*m***, **C22*m*** and **(C18*m*)$_2$Ni** were heated prior to deposition to improve the solubility. Self-assembled monolayers were observed immediate after the tip was engaged. Saturated solutions were prepared first then concentrations were gradually decreased until the best resolution of the imaged SAM was achieved.

The specific tunneling conditions are given in the figure captions. All Images were flattened and Gaussian smoothed using WSxM software[117] and the images in **Figure 33**, **Figure 34**, **Figure 37**, and **Figure 38** have been lattice-corrected for distortion due to drift.

3.5.2. Synthesis and characterization:

a) 4,6-di(octadecylamino)-m-quinone (C18*m*)

The detailed synthesis procedure of **C18*m*** can be found elsewhere (Chapter 2).[109]

b) 4,6-di(docosylamino)-*m*-quinone (C22*m*)

i. 1-azidodocosane:[118]

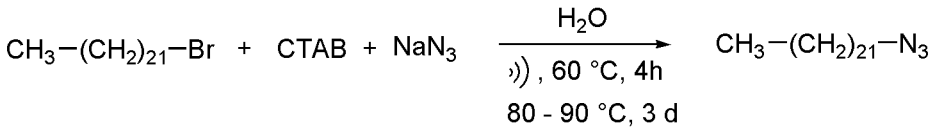

A mixture of bromodocosane (5.17 g, 13.3 mmol), hexadecyltrimethylammonium bromide (0.48 g, 1.32 mmol), Sodium azide NaN_3 (2.21 g, 34.0 mmol), and water (6 mL), was sonicated at 60 for 4 h. The resulting slurry was refluxed (80 - 90 °C) for 3 days. Hexane was used to extract the product from the milky reaction mixture and the solid was subjected to continuous Soxhlet extraction with hexane for 1 day. The filtrate was concentrated under vacuum yielding a sticky white solid which was subjected to the next

step without further purification (3.41 g, 9.70 mmol; 73%).[1]H NMR (300 MHz, $CDCl_3$): δ 0.88 (t, 3H), 1.24–1.33 (m, 38H), 1.55 (m, 2H), 3.26 (t, 2H).

ii. docosan-1-amine:[118]

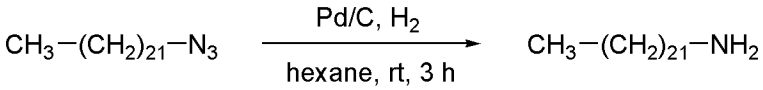

1-azidodocosane (3.41 g, 9.72 mmol) was dissolved in hexane (52 mL), followed by addition of 10% Pd/C (0.18 g). The mixture was shaken and hydrogenated at 62 psi at RT for 3 hours. After gravity filtration through Celite on a course glass frit, the filtrate was concentrated to give a white solid which was recrystallized from EtOAc to give the final white powder (2.45 g, 7.52 mmol; 77%). m.p. 64-66 °C; R_f 0.10 (98/2 $CHCl_3$/MeOH); [1]H NMR (300 MHz, $CDCl_3$): δ 0.88 (t, 3H), 1.20–1.35 (m, 40H; 2H), 1.44 (m, 2H), 2.68 (t, 2H). m.p. 64-66 °C. MS (LC-MSD-Tof): m/z: 326.4 $[M+H]^+$ calcd $[M+H]^+$: 326.38.

iii. 4,6-di(docosylamino)-*m*-quinone (C22*m*)

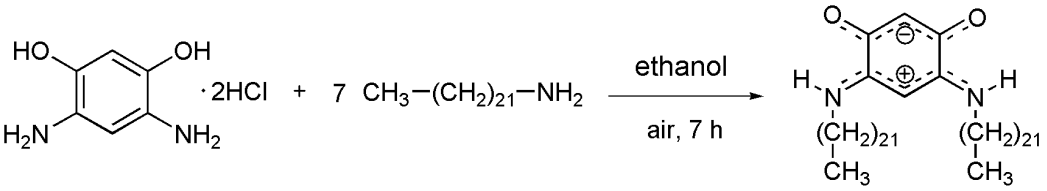

4,6-diaminoresorcinol dihydrochloride (0.10 g, 0.48 mmol) was dissolved in ethanol (16 mL). Docosan-1-amine (1.18 g, 3.63 mmol) was added to the reaction mixture to give a dark pink solution. The solution changed to dark brown/green with time. The mixture was left to stir for 7 hours, and then left on ice for 15 min. The solid was collected by vacuum filtration, washed with cold ethanol and air dried. Crude product was dissolved in a minimal amount of chloroform, purified using centrifugal chromatography, 98:2 $CHCl_3$/MeOH, on silica and dried under vacuum to yield the final product (253.8 mg, 0.34 mmol; 70.8%). The dissolved form of **C22*m*** is red, while the power form is green. m.p. 92-93 °C; R_f 0.37 (98:2 $CHCl_3$/MeOH); [1]H NMR (500 MHz, $CDCl_3$) δ 0.88 (t, 6H, C*H*$_3$), 1.34 (m, 76H, CH_2-C*H*$_2$-CH_2), 1.75 (q, 4H, NH-CH_2-C*H*$_2$), 3.36 (p, 4H, NH-C*H*$_2$),

5.13 (s, 1H, NH-C-C*H*), 5.47 (s, 1H, O-C-C*H*), 8.21 (br s, 2H, N*H*); ^{13}C (125 MHz, $CDCl_3$) δ 14.08, 22.66, 26.91, 28.29, 29.14, 29.33, 29.40, 29.53, 29.60, 29.64, 29.68, 31.90, 43.28, 80.48(N-C-*C*), 98.76(O-C-*C*), 156.71(N-*C*), 172.25 (O-*C*). MS (LC-MSD-Tof): m/z: 755.7 $[M+H]^+$ calcd [M+H]+: 755.74.

c) 2,5-di(octadecylamino)1,4-quinone (C18*p*)

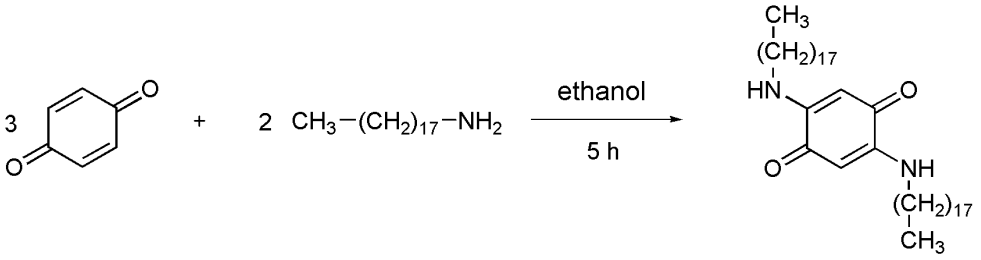

1,4-benzoquinone (75.3 mg; 0.693 mmol) and octadecylamine (125.1 mg; 0.462 mmol) with a molar ratio of 3:2 was dissolved in 15 mL of ethanol. The solution initially turns black and over time gains a slight redness. The mixture was left to stir for five hours and the solvent was removed under vacuum. The black powder was dissolved in a minimal amount of chloroform, purified using centrifugal chromatography (99.5/0.5 $CHCl_3$/MeOH) on silica and dried under vacuum to yield the final bright orange product (33.3 mg; 0.052 mmol; 22.4%). m.p. 100-102 °C; R_f 0.81; ^{1}H NMR (500 MHz, $CDCl_3$ at 21°C) δ 0.88 (t, ^3J= 7.0 Hz, 6H, C*H*$_3$), 1.2-1.4 (m, 60H, CH_2-C*H*$_2$-CH_2), 1.65 (tt, ^3J = 7.3 Hz, 4H, NH-CH_2-C*H*$_2$), 3.15 (quartet, ^3J= 6.7 Hz, 4H, NH-C*H*$_2$), 5.30 (s, 2H, O-C-C*H*), 6.61 (br t, ^3J = 6 Hz, 2H, N*H*); ^{13}C NMR (125 MHz, $CDCl_3$ at 21°C) δ = 14.13 (*C*H$_3$-CH_2), 22.84 (CH_3-*C*H$_2$), 27.01, 28.27, 29.24, 29.31, 29.38, 29.48, 29.56, 29.59, 29.64, 29.68, 29.70, 29.72 (*C*H$_2$CH$_2$), 31.95 (NH-CH_2-*C*H$_2$), 42.62 (NH-*C*H$_2$-CH_2), 92.65 (*C*H=C-NH), 151.37 (CH=*C*-NH), 178.13 (*C*=O), MS (Triple Quad-ESI): m/z: 643.65 $[M+H]^+$ calcd $[M+H]^+$: 643.61.

d) **Bis[4-(octadecylamino)-2-(octadecylimino)-5-oxo-1,4-cyclohexadienolato]nickel ((C18*m*)$_2$Ni)**

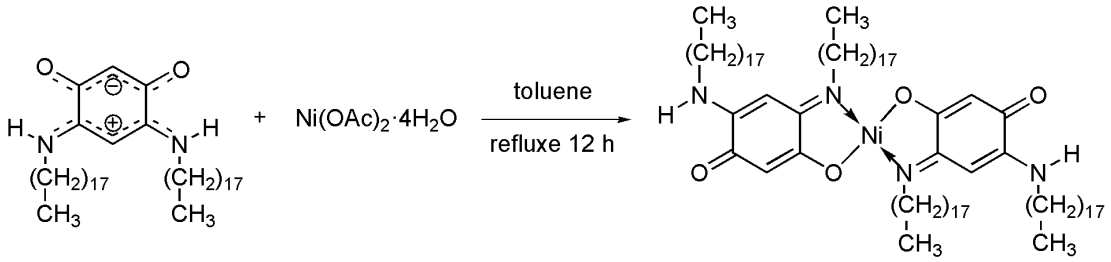

C18*m* (80.0 mg; 0.124 mmol) was dissolved in toluene (10.0 mL) with Nickel(II) acetate tetrahydrate ($Ni(OAc)_2.4H_2O$; 28.1 mg; 0.11 mmol). The mixture was left to stir under reflux for 12 hours. After cooling down the solution, the resulting precipitate, purple color with metallic lustre, was isolated by filtering through a Pyrex® Glass Buchner Funnel with medium porosity fritted disc (10-15 μm) and washed with cold chloroform (to remove starting material **C18*m***), hot water (to remove unreacted $Ni(OAc)_2$) and dried in air. A modified recrystallization method was performed to purified the crude product. The crude product (*ca.* 90% pure) was removed from glass disc (washed through) with hot chloroform, transferred to a separatory funnel with a total of 40 mL warm chloroform, and capped to prevent solvent evaporation. **(C18*m*)$_2$Ni** slowly crystallizes out of the solution, and due to the lower density of **(C18*m*)$_2$Ni** with respect to the chloroform, purple precipitate floats to the top of the solution. After one day (**(C18*m*)$_2$Ni** recrystallize slowly**)** the bottom red solution containing starting material **C18*m*** is drained, followed by adding another 40 mL of warm chloroform to redissolve **(C18*m*)$_2$Ni** in solution. The process was repeated 3 to 4 times until the bottom solution showed only a slight pink color. Solvent was drained and the final metallic lustre purple solid was dried under reduced pressure (57.5 mg; 0.086 mmol; 69%). Other recrystallization attempts from various solvents gave lower purity (95%). Chromatography (the Ni complex does not move on silica, alumina or cellulose plates) and soxhlet extraction (the Ni complex dissolve in most of hot solvents) were unsuccessful purification methods. m.p. > 200 °C; R_f 0 (98/2 $CHCl_3$/MeOH); ^{1}H NMR (500 MHz, $CDCl_3$ at 45°C) δ 0.88 (t, ^3J= 7.0 Hz, 12H, CH_3), 1.54 (m, 26H, CH_2-C*H*$_2$-CH_3), 2.84 (br t, ^3J= 7.3 Hz, 4H, NH-C*H*$_2$), 3.07 (q,

^{3}J= 6.7 Hz, 4H, NH-CH_2), 5.02 (s, 2H, NH-C-C*H*), 5.22 (s, 2H, O-C-C*H*), 6.26 (br s, 2H, N*H*); ^{13}C NMR (125 MHz, $CDCl_3$ at 45°C) δ = 14.06, 22.72 (CH_3-CH_2), 27.14, 27.39 (CH3-*C*H2), 28.44, 29.33, 29.39, 29.40, 29.47, 29.54, 29.62, 29.66, 29.69, 29.72, 29.73, 29.75, 29.78, 29.93, 31.99 (CH_2CH_2), 42.70, 47.74 (NH-CH_2), 83.27 (H*C*=C), 102.55(H*C*=C), 146.73 (C-N), 167.29 (*C*-O), 180.25 (C=N), 180.60 (*C*=O); MS (Triple Quad-ESI): m/z: 1342.51 $[M+H]^+$ calcd $[M+H]^+$: 1342.14

3.6. Acknowledgements

We thank Salamé, N. for assistance in the characterization of **C18*m*** and **C18*p***. P. Nguyen and E. Kebede for synthesis and characterization $C22NH_2$ and **C22*m***. NSERC, FQRNT, CFI, Concordia University and the German Science Foundation ("Deutsche Forschungsgemeinschaft") are acknowledged for funding within the Research Center 569 („Sonderforschungsbereich 569"). O.I. is grateful to FWO (the Fund of Scientific Research- Flanders) for a post-doctoral fellowship. We also acknowledge our membership in the FQRNT-supported, multi-university Centre for Self-Assembled Chemical Structures (CSACS).

Chapter 4.

Mechanochemistry and Solvent-Free Methods for the Preparation of Aminobenzoquinones

Yuan Fang, Nadime Salamé, Simon Woo, Tomislav Friščić and Louis A. Cuccia

4.1. Introduction

The synthesis and characterization of quinonoid compounds is important due to their fundamental role in many areas of chemistry and biochemistry.[87,119–122] Stable quinonoids are derived from *ortho*-benzoquinone and *para*-benzoquinone (I & II, respectively; **Figure 41**).[123] Aminobenzoquinones have been widely explored for biological applications, especially in medicinal chemistry. For example, they have anticancer and antimalarial properties. [120,124–131]

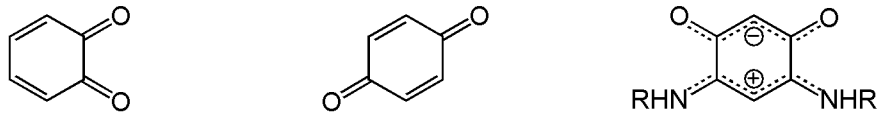

I II III

Figure 41. *Ortho*-benzoquinone (**I**), *para*-benzoquinone (**II**), and diamino-*meta*-benzoquinon*e* (**III**).

The first synthesis of a novel stable *meta*-benzoquinone zwitterion (**Figure 41**, III), which is formally a diamino derivative of *meta*-benzoquinone, was reported by Braunstein *et al.* (2002).[84] This zwitterion has attracted much attention due to its unique structural and physical properties.[123,132–136] X-ray crystal structure analysis of *meta*-diaminobenzoquinones reveal that they are formal zwitterions with two separate charged subunits.[123] In 2005, Braunstein *et al.* developed a simple one-pot synthetic route to prepare these *meta*-diaminobenzoquinones, also known as, *p*-benzoquinonemonoimine zwitterions.[87] This new synthetic strategy incorporates a transamination reaction and allows for a wide variety of functionalities to be attached to the quinonoid core (**Figure 41**, III).[87,88,114,137–139] These quinonoids show rich organic chemistry,[140,141] supramolecular chemistry[84,88,140] and coordination chemistry.[88,140,142] Their zwitterionic nature allows these molecules to self-assemble into extended 2D networks at the liquid-solid interface of highly ordered pyrolytic graphite *via* charge-assisted hydrogen bonding.[109] Their self-assembly properties have also been investigated on other surfaces, including graphene, Cu(111), Ag(111) and gold substrates.[110,111,143] Routaboul *et al.* have employed these benzoquinones to alter static dipoles on surfaces taking advantage of their large intrinsic

dipole (*ca.* 10 Debye), a consequence of their zwitterionic character.[110] Furthermore, thin film conductivity due to π-stacking was observed for these zwitterionic benzoquinonemonoimines and it was proposed that these conductive molecular films could play an important role in organic electronics devices.[110]

N,O metal complexes, "have been recognized as an important class of molecules endowed with interesting structural, electronic, magnetic, nonlinear optical, or catalytic properties."[88] Due to the presence of both nitrogen and oxygen functional groups, these quinonoid compounds are ideal ligands for the formation of metal complexes.[139,140,142,144] For example, Ni complexes of compound III (**Figure 41**) can catalyze ethylene polymerization.[114,142,144]

The synthesis of *para*- and *meta*-aminobenzoquinones through traditional reactions is well established.[87,88,106,145,146] These reactions, however, often require polar solvents and long reaction times. A new "greener" synthesis of this class of molecules was of great interest in order to make them more readily accessible for investigating their potential applications and to exploit their possible use as intermediates in synthetic chemistry. In this paper we report new and extremely efficient solvent-free syntheses of members of these molecular families through mechanochemistry. Specifically, the synthesis of *para*-aminobenzoquinone derivatives, *meta*-aminobenzoquinone derivatives and a *meta*-aminobenzoquinone Ni complex were investigated. We also demonstrate the importance of temperature effects resulting from the mechanochemical grinding which guided us to alternative reaction conditions using melt chemistry. To the best of our knowledge, this is the first report of mechanochemical and melt syntheses of aminobenzoquinone molecules.

4.2. Results and Discussion

Synthesis of zwitterionic amino *meta*-benzoquinones: For 4,6-di(alkylamino)-*m*-quinones, the conventional solution based synthesis involves reacting 4,6-diaminoresorcinol dihydrochloride with excess alkylamine, typically in a 1:7 ratio in organic or aqueous solvents for approximately two hours at room temperature (**Table 2**,

entries 1, 2, 8, 9, 15, & 16). Two equivalents of the alkylamine are required to neutralize the HCl salt, while the remaining excess alkylamine drives the reversible reaction forward (**Table 2**). Mechanochemistry was applied to synthesize these derivatives in an attempt to eliminate the use of solvents and reduce reaction times. An excess of alkylamines (4 or 7 equiv) and 4,6-diaminoresorcinol dihydrochloride were added to a 2 mL screw cap Eppendorf tube (lysis tube) loaded with ceramic beads to a specific height (*vide infra*). The tube was then shaken using a cell lysis apparatus for 10 shaking cycles (1 minute shaking with a 5 minutes instrument cooling period - 10 min. shaking time; 1 hour total time) after which the reaction mixture became dark green for **C18*m*** or dark purple for **C12*m*** and **C4*m***, indicating a reaction had taken place. The crude products were purified by chromatography to provide pure products in high yield (**Table 2**, entries 3, 4, 10, 11, 17, & 18).

Based on the success of the synthesis in the lysis mill, we also investigated the synthesis of the *meta* compounds in a ball mill setup. The synthesis of **C18*m*** from diaminoresorcinol dihydrochloride and octadecylamine was the first tested with this apparatus. However, after 60 minutes reaction at 30 Hz, the appearance of the reaction mixture, which was brownish red in color, was different from that obtained in the cell lysis apparatus experiment. This brownish red product was characterized and determined to be primarily **C0*m*** (scheme in **Table 2**), an intermediate on the route to the target zwitterionic *meta*-quinone.[87] The reason for the difference in results obtained from the lysis mill versus the ball mill was investigated further.

During the experiments with the lysis mill, it was noted that the temperature of the tubes following the same period of agitation varied, and higher yields of products were obtained in the hotter tubes. In the cooler tubes, the yields were lower, and by TLC analysis it was determined that large quantities of **C0*m*** were present (**C0*m*** has a brownish red color and has an R_f = 0 chloroform/methanol 90/10). It was believed that the main factor contributing to this temperature variability was the number of ceramic beads placed inside the tube (*i.e.* the "bead height" of the tube). This was verified by measuring the temperature of the tube contents after 1 minute of agitation (6.0 m/s), using

a thermocouple (inserted into the ceramic beads), as a function of bead height. The results, shown in **Figure 42**, confirmed that the bead height had a considerable effect on the temperature of the vial contents following agitation, with a maximum temperature of approximately 70 °C after 1 minute when the bead height was 60-70% of the tube height. A low level of beads limited the temperature increase, presumably due to a lower overall number of collisions between the beads. On the other hand, too many beads also resulted in a limited temperature increase, possibly due to less efficient conversion of kinetic energy into heat when the beads are not able to move freely.

It was noticed that in the ball milling experiments, the temperature of the steel jars did not increase significantly past room temperature after one hour of shaking at 30 Hz. We reasoned that the lower temperature was not sufficient to overcome the activation barrier to convert the intermediate (**C0*m***) to the final product, in spite of the mechanical input.

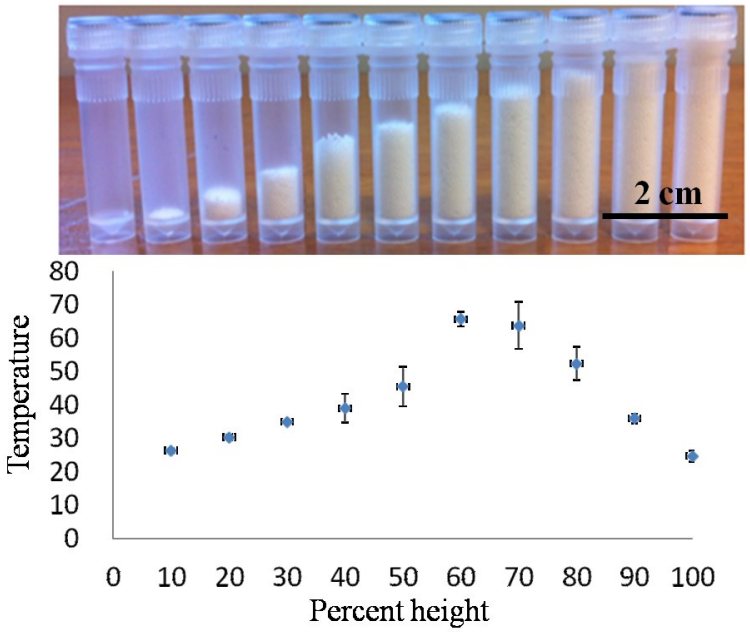

Figure 42. Lysis tube temperature after 1 minute of agitation in the lysis mill operating at 6.0 m/s as a function of bead height.

In light of this new information, the ball-milling experiment was repeated for synthesizing **C18*m*** with the steel reaction jar containing the starting materials pre-heated

in an oven at 45 °C for 20 minutes prior to shaking at 30 Hz for one hour. The appearance of the crude product, which was dark green in color, more closely resembled that obtained from the lysis mill experiments, and the formation of the desired product was confirmed by TLC and NMR analysis (**Table 2**, entries 19 & 20). On the other hand, the synthesis of **C12*m*** and **C4*m*** using the ball milling setup did not require heat (**Table 2**, entries 5, 6, 12, & 13). It was noticed that dodecylamine and *n*-butylamine have lower melting points, 28 °C and -49 °C, respectively, than octadecylamine (52 °C).[147] At this point, we questioned whether grinding was necessary for these reactions to proceed, or whether it simply served as a means to heat the reaction mixture. The maximum temperature of 70 °C observed in the lysis mill tubes is clearly sufficient to melt octadecylamine, suggesting the possibility that a melt reaction might have occurred. A simple melt reaction for the synthesis of **C18*m*** was carried out by mixing 4,6-diaminoresorcinol dihydrochloride with excess octadecylamine. The two powders were ground together using a mortar and pestle for two minutes, with no significant color change observed. The mixture of powders was then transferred to an open vial and heated at 70 °C with stirring for 5 minutes. As soon as the octadecylamine melted, a color change from white to dark green was observed and product formation was confirmed by TLC and NMR analysis (**Table 2**, entry 21). In conclusion, it was determined that this transamination reaction to prepare zwitterionic *meta*-benzoquinones can proceed simply in the melt. In the case of **C18*m***, only the melting of the octadecylamine was necessary. This was further confirmed with the synthesis of **C4*m*** and **C12*m***. When the reaction was attempted using 4,6-diaminoresorcinol dihydrochloride and *n*-butylamine, a liquid at room temperature, no heat was required for the reaction to proceed. As soon as both starting materials were combined, the transparent reaction mixture became red indicating the formation of product (**Table 2**, entry 7). In the case of **C12*m*** formed from dodecylamine, the reaction mixture was heated to 35 °C for 5 minutes. As expected, the color change associated with product formation was apparent immediately after the dodecylamine melted (**Table 2**, entry 14). In the end, due to the high reactivity of alkylamines with 4,6-diaminoresorcinol dihydrochloride, a thorough mixing of the

reagents (either by melting or mechanically-induced melting) is sufficient for the reaction to occur in the absence of solvent.

Table 2. Synthesis of 4,6-di(alkylamino)-*m*-benzoquinones under various reaction conditions.

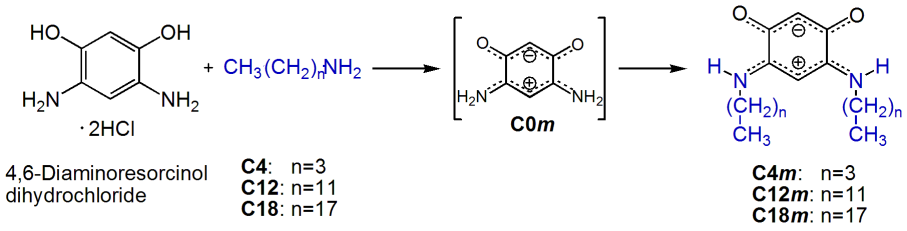

entry	product	reaction type[a]	time (min)	alkyl amine (equiv)	yield %
1		A	120	4	79
2		A	120	7	88
3		B	10	4	83
4	**C4*m***	B	10	7	86
5		C	60	4	80
6		C	60	7	89
7		D	10	10	92
8		A	120	4	70
9		A	120	7	74
10		B	10	4	79
11	**C12*m***	B	10	7	85
12		C	60	4	81
13		C	60	7	86
14		D	10	8	87
15		A	120	4	75
16		A	120	7	80
17		B	10	4	70
18	**C18*m***	B	10	7	90
19		C	60[b]	4	83
20		C	60[b]	7	87
21		D	10	7	69

[a] Reaction Type A, conventional solvent synthesis in MeOH for **C4*m*** and EtOH for **C12*m*** and **C18*m***; Type B, lysis mill; Type C, ball mill; Type D, melt. [b] Pre-heated in oven at 45 °C for 20 minutes.

Synthesis of *para*-aminobenzoquinones: Mechanochemistry was also successfully applied for the synthesis of the isomeric *para* compounds. Conventionally, 2,5-di(alkylamino)-1,4-benzoquinones are synthesized by mixing 1,4-benzoquinone and various alkylamines in a 3:2 ratio in ethanol, with stirring at room temperature for five hours (**Table 3**, entries 1, 5, & 9).[106,145,146] In the reaction, 2 of the 3 equivalents of benzoquinone serve to oxidize the reaction intermediates back to the quinone oxidation state. The first interesting aspect of this reaction is that a change in color is apparent as soon as both solid reagents come into contact prior to dissolution. In fact, a color change is apparent as soon as both powdered reagents are brought into close proximity, even prior to dissolution. To better visualize this phenomenon, the two starting materials, benzoquinone and octadecylamine, were placed in separate vials contained within a sealed jar (**Figure 43**).

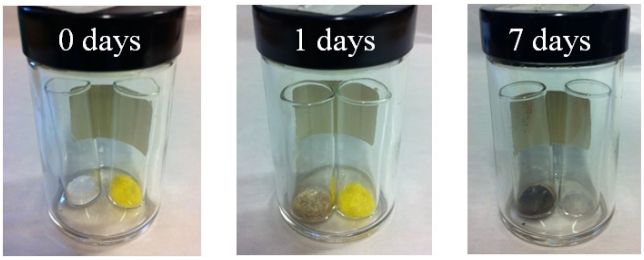

Figure 43. Vapor phase synthesis of 2,5-di(octadecylamino)-1,4-quinone, **C18*p***. With time, the quantity of yellow 1,4-benzoquionone reduces, and white octadecylamine gradually darkens, which indicates a reaction has occurred.

Over the course of several days, the originally white octadecylamine changed color from slightly brown orange (after several hours) to light brown (after one day) to dark brown (after one week). TLC analysis of the dark brown powder revealed the presence of product, **C18*p***. The high vapor pressure of benzoquinone likely facilitates contact between the two otherwise isolated starting materials under these conditions. With this evidence that the reaction occurs in the absence of solvent, and based on the successful synthesis of the *meta*-benzoquinones, we then attempted to enhance the mixing of the solids by grinding both of the reagents together in the lysis mill and the ball

mill. The same 3:2 stoichiometric ratio of reagents were placed inside a 2 mL screw cap eppendorf tube (lysis tube) loaded with ceramic beads (1 mm in diameter) to 3/4 of the tube height. The tube was shaken at 6.0 m/s using the cell lysis apparatus for 5 shaking cycles (1 minute shaking with a 5 minute instrument cooling period - 5 min. shaking time; 30 min. total time; **Table 3**, entries 2, 6, & 10). The color of the reaction mixture changed to black in less than one minute.

Table 3. Synthesis of 2,5-di(alkylamino)-1,4-quinones.

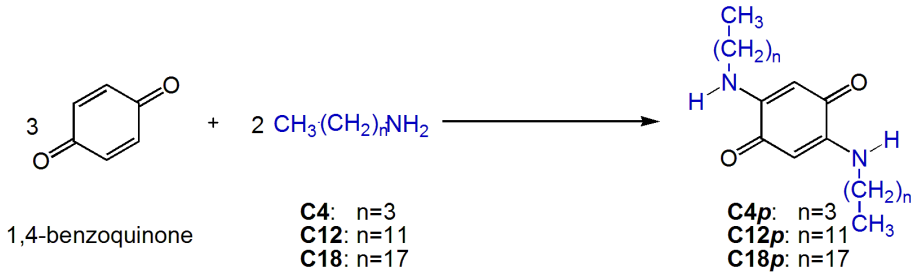

entry	product	reaction type[a]	time (min)	yield %
1	**C4*p***	A	300	32
2		B	5	27
3		C	7	25
4		D	5	22
5	**C12*p***	A	300	29
6		B	5	30
7		C	7	32
8		D	5	26
9	**C18*p***	A	300	22
10		B	5	28
11		C	7	27
12		D	5	27

[a] Reaction Type A, conventional solvent synthesis in EtOH; Type B, lysis mill; Type C, ball mill; Type D, melt.

The reaction was also successful with a standard ball mill apparatus. After grinding the reagents together for 7 minutes, comparable yields of the desired products were obtained (**Table 3**, entries 3, 7, & 11). Interestingly, as in the case with the *meta* compounds, the synthesis also can be carried out simply in the melt. Both reactants were

mixed and heated to 70 °C for 5 minutes. The mixture turns black immediately when the alkylamine melts. In the synthesis of **C4*p*** (**Table 3**, entry 4), when liquid *n*-butylamine was added to the yellow benzoquinone powder, white vapour was visualized inside the sealed vial, suggesting a sufficiently exothermic reaction to partially vaporize the *n*-butylamine. After work up, it was determined that the yields were comparable to those of both the conventional solvent reaction and the mechanochemical synthesis (**Table 3**, entries 1-4). It should be noted that higher yields (70%) have been reported for the synthesis of **C4*p*** with a 1:2 ratio of 1,4-benzoquinone and *n*-butylamine in solvent reacting under aerobic conditions for 15 hours.[148] We obtained only 9% yield when we attempted the reaction under the same conditions. In conclusion, alkylamines and 1,4-benzoquinone react readily as soon as both reagents are in contact, either in solution, in the solid-state, in the vapor phase, or in the melt.

Synthesis of nickel-**III** complex (**(C18*m*)$_2$Ni**)

(Bis[4-(octadecylamino)-2-(octadecylimino)-5-oxo-1,4-cyclohexadienolato]nickel

The last reaction attempted by mechanochemistry was the synthesis of **(C18*m*)$_2$Ni**. The conventional solvent reaction was carried out overnight in refluxing toluene using a 1:1 ratio of **C18*m*** and nickel(II) acetate tetrahydrate, Ni(OAc)$_2$•4H$_2$O (**Table 4**, entry 1). These conditions were based on those reported for the synthesis of a related compound, **(C4*m*)$_2$Ni**, with shorter alkyl chains, using nickel(II) acetylacetonate, Ni(acac)$_2$ (**C4*m***:Ni(acac)$_2$; 2:1).[114] We successfully substituted the less expensive Ni(OAc)$_2$•4H$_2$O reagent for Ni(acac)$_2$ in the solution synthesis (*i.e.* Ni(acac)$_2$ (95%, Sigma-Aldrich), CAD$ 468/mol; Ni(OAc)$_2$•4H$_2$O (98%, Sigma-Aldrich), CAD$ 93/mol). We considered the use of the even less expensive nickel reagent, nickel(II) hydroxide, Ni(OH)$_2$ (Sigma-Aldrich, CAD$ 80/mol). There is a clear advantage for using nickel hydroxide, not only because of the cost, but also because the by-product is water. However, due to the low solubility of nickel hydroxide, it is not a reagent of choice in solution reactions (**Table 4**, entry 2). For the mechanochemical syntheses carried out with the lysis mill, reagent solubility is no longer a factor, and both nickel acetate and nickel(II) hydroxide, Ni(OH)$_2$

could be used. In the lysis mill, $Ni(OAc)_2 \bullet 4H_2O$ or $Ni(OH)_2$ react with **C18*m*** to give 85% and 80% yield of the **(C18*m*)$_2$Ni** complex, respectively, after 20 shaking cycles (1 minute shaking with a 5 minutes instrument cooling period - 20 min. shaking time; 120 min. total time), respectively (**Table 4**, entries 3 & 4). For the reaction with nickel acetate, a distinct odor of acetic acid, which is the by-product of the reaction, was noticed upon opening the reaction vial. The reaction was also successful with a standard ball mill apparatus. After grinding the reagents together for 2 hours, comparable yields of the desired product were obtained (**Table 4**, entries 5 & 6). The solvent-free synthesis of the **(C18*m*)$_2$Ni** complex is a true solid state reaction, since all the starting materials and metal complexes have high melting points.

Table 4. Synthesis of Bis[4-(octadecylamino)-2-(octadecylimino)-5-oxo-1,4-cyclohexadienolato]nickel **(C18*m*)$_2$Ni** under different reaction conditions.

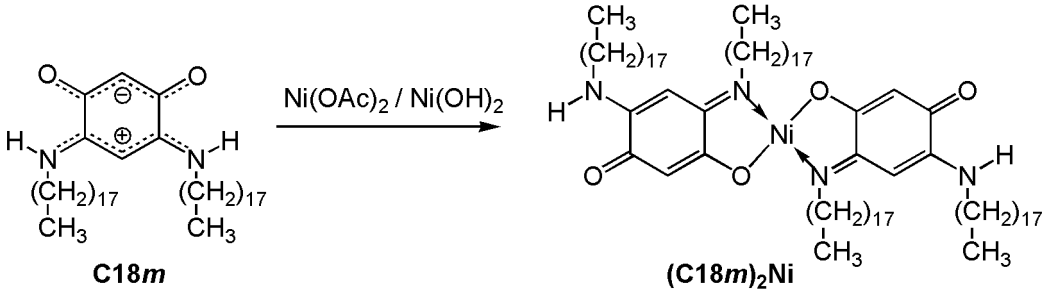

entry	reaction type[a]	time (min)	starting materials, equiv	yield %
1	A	720	C18*m*: nickel acetate, 1:1	69
2	A	720	C18*m*: nickel hydroxide, 1:1	10
3	B	20	C18*m*: nickel acetate, 1:1	85
4	B	20	C18*m*: nickel hydroxide, 1:1	80
5	C	120	C18*m*: nickel acetate, 1:1	71
6	C	120	C18*m*: nickel hydroxide, 1:1	70

[a] Reaction Type A, conventional solvent synthesis in refluxing toluene?; Type B, lysis mill; Type C, ball mill.

4.3. Conclusion

In conclusion, two families of aminobenzoquinone molecules and the *meta* metal complex of **C18*m*** were synthesized under several solvent-free reaction conditions. Compared to conventional solvent reactions, the reaction times are significantly reduced. In a matter of minutes, yields comparable to what normally takes hours in solution can be obtained. Furthermore, solvent-free mechanochemistry provides more flexibility for the choice of starting materials. Finally, in this case, the reaction temperature attained during the shaking process was an important factor to consider when optimizing mechanochemistry reaction conditions.

4.4. Experimental

4.4.1. Chemicals and Instrumentation

Chemicals: 4,6-Diaminoresorcinol dihydrochloride, *n*-butylamine, dodecylamine, octadecylamine and deuterated chloroform were obtained from Aldrich. 1,4-benzoquinone was obtained from American Chemicals. Chloroform, diethyl ether, ethanol, hexanes and methanol were obtained from Fisher Scientific. Deuterated DMSO was obtained from Cambridge Isotope Laboratories, Inc. Toluene was obtained from J.T. Baker. Nickel(II) acetate tetrahydrate ($Ni(OAc)_2 \bullet 4H_2O$) was obtained from BDH Chemicals. Nickel(II) hydroxide ($Ni(OH)_2$) were obtained from Research Organic/Inorganic Chemical Corp. Melting points (m.p.) were recorded with a capillary melting point apparatus (Thomas Hoover). The recorded R_f values were determined by a standard thin-layer chromatography (TLC) procedure: 0.25 mm silica gel plates (Aldrich, 122785-25EA).

NMR: ^1H NMR (500 MHz) and ^{13}C NMR (125 MHz) spectra were recorded on a Varian 500 spectrometer. The residual proton signals of the deuterated solvents were used as internal standards ($CDCl_3$: δ (^1H) 7.26 ppm, δ (^{13}C) 77.0 ppm; DMSO: δ (1H) 2.48 ppm, δ (13C) 40.0 ppm). The following notation is used for the ^1H NMR splitting patterns: singlet (s), doublet (d), triplet (t), quartet (q), multiplet (m) and broad signal (br).

MS: For both *meta* and *para* compounds mass spectrometric analysis was performed using a Waters Micromass, Quattro LC triple quadrupole mass spectrometer (Waters, Montreal, PQ, Canada). The instrument was operated using an ESI (electrospray ionization) source by direct injection with a syringe pump (50 μL syringe; flow rate: 1 μL/min). The MS instrument was operated in the positive mode (ES+) and the data acquisition/analysis was carried out using Masslynx software version 4.01. Source working conditions were as follows: cone voltage: 20 V, Capillary voltage: 3.3 V, source temperature: 90 °C, desolvation temperature: 100 °C, desolvation gas flow rate: 220 L/hr, nitrogen: (99.9% purity). Mass spectrometric analysis of individual compounds: The aminobenzoquinone derivatives were dissolved in acetonitrile/water (1:1; 100 mL). Prior to MS analysis, 1 mL of this solution was further diluted into acetonitrile/water (1:1; 10 mL) and formic acid (10 μL) was added. For **(C18*m*)$_2$Ni**, mass measurements were performed on Bruker Ultraflex MALDI TOF/TOF Mass Spectrometer. MALDI was used as ionization method, with dithranol as matrix, in reflector mode. The protonated molecular ion $[M]^+$ was used for empirical formula confirmation.

4.4.2. Synthesis and characterization

General Methods for synthesizing *meta* compounds

Method A: Conventional solvent synthesis

In a round bottomed flask, a total mass of *ca.* 0.2 g of diaminoresorcinol dihydrochloride and 4-7 equiv. of various primary alkylamines, RNH_2, were mixed in 10 mL in a solvent. The mixture was left to stir for two hours. The reaction mixture was dried under reduced pressure. The crude product was dissolved in a minimum amount of chloroform insoluble

solids were filtered out and purified by centrifugal thin-layer chromatography using mixtures of chloroform and methanol as eluent.

Method B: Cell lysis grinding

In a 2 mL screw cap eppendorf tube (**Figure 44a**, lysis tube), a total mass of *ca.* 0.1 g of diaminoresorcinol dihydrochloride and 4-7 equiv. of various primary alkylamines, RNH_2, was added with ceramic beads (**Figure 44b**, 1 mm in diameter) to 3/4 of the tube height. The tube was then shaken at 6.0 m/s using a cell lysis apparatus (**Figure 44c**) for 10 shaking cycles (1 minute shaking with a 5 minutes instrument cooling period - 10 min. shaking time; 1 hour total time).

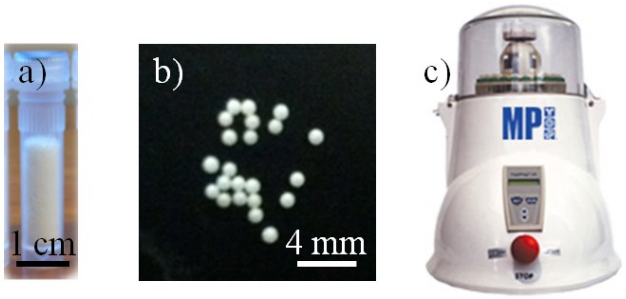

Figure 44. a) lysis tube b) ceramic beads and c) FastPrep®24 cell lysis mill.

Method C: Ball milling

In a 10 mL steel grinding jar with two stainless steel balls of 7 mm diameter, a total mass of *ca.* 0.2 g of diaminoresorcinol dihydrochloride and 4-7 equiv. of various primary alkylamines, RNH_2, were added. The reaction mixture was ground for a period of 60 minutes in a Retsch MM200 ball mill operating at a frequency of 30 Hz (**Figure 45**).

Figure 45. MM200 Retsch ball mill

Method D: Melt

In a 5 mL glass vial with a stir bar, a total mass of *ca.* 0.4 g of diaminoresorcinol dihydrochloride and 7-10 equiv. of various primary alkylamines, RNH_2, were added and heated with stirring for 10 minutes at a temperature slightly higher than the melting point of the alkylamine.

General Methods for synthesizing *para* compounds

Method A: Conventional solvent synthesis

In a round-bottom flask, a total mass of *ca.* 0.2 g of 1,4-benzoquinone and various primary alkylamines, RNH_2, with molar ratio of 3:2 were mixed in 10 mL of ethanol. The mixture was left to stir for five hours. Solvent was removed under reduced pressure. The crude product was dissolved in a minimum amount of chloroform and purified by centrifugal thin-layer chromatography using mixtures of chloroform and methanol as eluent.

Method B: Cell lysis grinding

In a 2 mL screw cap eppendorf tube, a total mass of *ca.* 0.1 g of 1,4-benzoquinone and various primary alkylamines, RNH_2, with molar ratio of 3:2 were added with ceramic beads to 3/4 of the tube height. The tube was then shaken at 6.0 m/s using a cell lysis apparatus for 10 shaking cycles (1 minute shaking with a 5 minutes instrument cooling period - 10 min. shaking time; 1 hour total time).

Method C: Ball milling

In a 10 mL steel grinding jar with two stainless steel balls of 7 mm diameter, a total mass of *ca.* 0.2 g of 1,4-benzoquinone and various primary alkylamines, RNH_2, with molar ratio of 3:2 were added. The reaction mixture was ground for a period of 7 minutes in a Retsch MM200 ball mill operating at a frequency of 30 Hz.

Method D: Melt

In a 5 mL glass vial with a stir bar, a total mass of *ca.* 0.4 g of 1,4-benzoquinone and various primary alkylamines, RNH_2, with molar ratio of 3:2 were added and heated for 5 minutes with stirring to a temperature higher than the melting point of the alkylamine.

4,6-diamino-m-quinone (C0*m*):

4,6-Diaminoresorcinol dihydrochloride (30.9 mg; 0.145 mmol) was dissolved in water (4 mL), and one drop of ammonium hydroxide was added to the stirred solution. The mixture was left to stir for *ca*. one day. The resulting dark purple precipitate was isolated by filtration, washed with water, and then dried in air. The air-dried product was subsequently dried under reduced pressure to afford the title compound (182 mg; 0.132 mmol; 91%). m.p. greater than 250 °C; R_f = 0 (90/10 $CHCl_3$/MeOH); ^{1}H NMR (500 MHz, DMSO-D_6 at 21°C) δ = 4.89 (s, 1H, N-C-C-*H*), 5.60 (s, 1H, O-C-C-*H*), 8.38 (s, 1H, N*H*$_2$), 9.15 (s, 1H, N*H*$_2$); ^{13}C NMR (125 MHz, DMSO-D_6 at 21°C): δ = 86.7 (N-C-*C*), 98.4 (O-C-*C*), 160.48 (N-*C*), 172.98 (O-*C*).

4,6-di(butylamino)-*m*-quinone (C4*m*):

Conventional solvent synthesis

General Method A was followed using methanol (10 mL), 4,6-diaminoresorcinol dihydrochloride (85 mg; 0.40 mmol) and *n*-butylamine (0.17 ml; 119 mg; 1.63 mmol, 4 equiv.) and a reaction time of 2 hours. The title compound (79.5 mg; 0.32 mmol; 79%; purple powder) was obtained following purification using 96:4 chloroform:methanol as eluent.

Lysis grinding

General method B was followed using 4,6-Diaminoresorcinol dihydrochloride (44.7 mg; 0.21 mmol) and 4 equiv. *n*-butylamine (0.089 ml; 62 mg; 0.85 mmol). (44.2 mg; 0.176 mmol; 83%)

Ball milling

General method C was followed using 4,6-Diaminoresorcinol dihydrochloride (83 mg; 0.39 mmol) and 4 equiv *n*-butylamine (0.165 ml; 116 mg; 1.58 mmol). (78.1 mg; 0.312 mmol; 80%)

Melt

General method D was followed using 4,6-diaminoresorcinol dihydrochloride (89.6 mg; 0.42 mmol) and 10 equiv. *n*-butylamine (0.443 ml; 310 mg; 4.24 mmol). (96.8 mg; 0.388 mmol; 92%)

m.p. 93-95 °C; R_f 0.35 (98/2 $CHCl_3$/MeOH); ^{1}H NMR (500 MHz, $CDCl_3$ at 21°C) δ = 0.99 (t, ^3J= 7.0 Hz, 6H, CH_2-C*H*$_3$), 1.44 (sextet, ^3J= 7.5 Hz, 4H, CH_2-C*H*$_2$-CH_3), 1.73 (quintet, ^3J= 7.0 Hz, 4H, NH-CH_2-C*H*$_2$), 3.38 (q, ^3J= 6.5 Hz, 4H, NH-C*H*$_2$), 5.14 (s, 1H, NH-C-C*H*), 5.45 (s, 1H, O-C-C*H*), 8.26 (br, 2H, N*H*); ^{13}C NMR (125 MHz, $CDCl_3$ at 21°C) δ = 13.6 (*C*H_3-CH_2), 20.1 (*C*H_2CH_3), 30.2 (NH-CH_2-*C*H_2), 43.0 (NH-*C*H_2-CH_2), 80.61 (NH-C-*C*H), 98.95 (O-C-*C*H), 156.57 (NH-*C*), 172.38 (*C*-O).

4,6-di(dodecylamino)-*m*-quinone (C12*m*):

Following the general methods, the title compound (green powder) was obtained following purification on silica using 96:4 chloroform:methanol as eluent. In addition to following general method D, the two starting materials were premixed using a mortar and pestle before transferring to a glass vial. m.p. 93-95 °C; R_f 0.65 (98/2 $CHCl_3$/MeOH); ^{1}H NMR (500 MHz, $CDCl_3$ at 21°C) δ = 0.88 (t, ^3J= 7.0 Hz, 6H, CH_2-C*H*$_3$), 1.22-1.50 (m, 36H, CH_2-C*H*$_2$), 1.74 (quintet, ^3J= 7.0 Hz, 4H, NH-CH_2-C*H*$_2$), 3.36 (q, ^3J= 6.5 Hz, 4H, NH-C*H*$_2$), 5.12 (s, 1H, NH-C-C*H*), 5.46 (s, 1H, O-C-C*H*), 8.24 (br, 2H, N*H*); ^{13}C NMR (125 MHz, $CDCl_3$ at 21°C) δ = 14.08 (*C*H_3-CH_2), 22.56 (*C*H_2CH_3), 26.91, 27.48, 28.55, 29.73, 29.74, 29.82, 29.88, 31.99 (*C*H_2CH_2), 43.88 (NH-*C*H_2-CH_2), 80.31 (NH-C-*C*H),

98.75(O-C-*C*H), 156.41 (NH-*C*), 172.22 (*C*-O), MS (Triple Quad-ESI): m/z: 475.40 $[M+H]^+$, calcd $[M+H]^+$: 475.78.

4,6-di(octadecylamino)-*m*-quinone (C18*m*):[2]

Following general methods, the title compound (green powder or red crystal) was obtained after purification using 98:2 chloroform:methanol as eluent. In addition to following general method D, the two starting materials were premixed using a mortar and pestle before transferring to a glass vial. m.p. 105.5-107.0 °C; R_f 0.35 (98/2 $CHCl_3$/MeOH); ^{1}H NMR (500 MHz, $CDCl_3$) δ 0.88 (t, ^3J= 7.0 Hz, 6H, CH_3), 1.25-1.28 (m, 56H, CH_2-CH_2-CH_2), 1.73 (quintet, ^3J= 7.3 Hz, 4H, NH-CH_2-CH_2), 3.37 (q, ^3J= 6.7 Hz, 4H, NH-CH_2), 5.13 (s, 1H, NH-C-C*H*), 5.44 (s, 1H, O-C-C*H*), 8.32 (br, 2H, N*H*); ^{13}C NMR (125 MHz, $CDCl_3$): δ 14.1 (CH_3), 22.6, 26.9, 28.3, 29.1, 29.3, 29.4, 29.5, 29.6, 29.7, 31.9, 43.3, 80.5 (N-C-*C*), 98.8 (O-C-*C*), 156.6 (N-*C*), 172.3 (O-*C*); MS (Triple Quad-ESI): m/z: 643.65 $[M+H]^+$ calcd $[M+H]^+$: 643.61

2,5-di(butylamino)1,4-quinone (C4*p*)

Conventional solvent synthesis

General method A was followed using 1,4-benzoquinone (141 mg; 1.3 mmol) and *n*-butylamine (0.091 ml, 64 mg; 0.88 mmol) with a molar ratio of 3:2 and a reaction time of 5 hours. The title compound (35.3 mg; 0.14 mmol; 32%; bright orange) was obtained following purification using 99.5:0.5 chloroform:methanol as eluent.

Lysis grinding

General method B was followed using 1,4-benzoquinone (70.1 mg, 0.65 mmol) and *n*-butylamine (0.046 ml, 32 mg; 0.44 mmol). (14.9 mg; 0.06 mmol; 27%).

Ball milling

General method C was followed using 1,4-benzoquinone (139 mg; 1.3 mmol) and *n*-butylamine (0.09 ml, 63 mg; 0.86 mmol). (27.0 mg; 0.11 mmol; 25%).

Melt

General method D was followed using 1,4-benzoquinone (275.9 mg, 2.6 mmol) and *n*-butylamine (0.180 ml, 126 mg; 1.7 mmol). The two starting materials were combined in a 5 mL capped glass vial with a stir bar and stirring at room temperature for 5 mins. (46.9 mg; 0.19 mmol; 22%).

m.p. 100-102 °C; R_f 0.81 (98/2 $CHCl_3$/MeOH); ^{1}H NMR (500 MHz, $CDCl_3$ at 21°C) δ = 0.88 (t, ^3J= 7.0 Hz, 6H, CH_2-C*H*$_3$), 1.34 (sextet, ^3J= 7.5 Hz, 4H, CH_2-C*H*$_2$-CH_3), 1.57 (quintet, ^3J= 7.0 Hz, 4H, NH-CH_2-C*H*$_2$), 3.09 (q, ^3J= 6.5 Hz, 4H, NH-C*H*$_2$), 5.24 (s, 2H, C-C*H*-C), 6.55 (br t, ^3J= 5.5 Hz 2H, N*H*); ^{13}C NMR (125 MHz, $CDCl_3$ at 21°C) δ = 13.63 (*C*H_3-CH_2), 20.13 (*C*H_2-CH_3), 30.22 (NH-CH_2-*C*H_2), 42.28 (NH-*C*H_2-CH_2), 92.61 (*C*H=C-NH), 151.37 (CH=*C*-NH), 178.06 (*C*=O).

2,5-di(dodecylamino)1,4-quinone (C12*p*)

Following general methods, the title compound (bright orange) was obtained after purification using 99.5:0.5 chloroform:methanol as eluent. m.p. 100-102 °C; R_f 0.81 (98/2 $CHCl_3$/MeOH); ^{1}H NMR (500 MHz, $CDCl_3$ at 21°C) δ = 0.88 (t, ^3J= 7.0 Hz, 6H, CH_2-C*H*$_3$), 1.16-1.35 (m, 36H, CH_2-C*H*$_2$), 1.56 (quintet, ^3J= 7.0 Hz, 4H, NH-CH_2-C*H*$_2$), 3.07 (q, ^3J= 6.5 Hz, 4H, NH-C*H*$_2$), 5.23 (s, 2H, C-C*H*-C), 6.54 (br t, ^3J= 5.5 Hz 2H, N*H*); ^{13}C NMR (125 MHz, $CDCl_3$ at 21°C) δ = 14.1 (*C*H_3-CH_2), 22.7, 26.9, 28.2, 29.2, 29.3, 29.4, 29.5, 29.6 (*C*H_2CH_2), 31.89 (NH-CH_2-*C*H_2), 42.60 (NH-*C*H_2-CH_2), 92.61 (*C*H=C-NH), 151.37 (CH=*C*-NH), 178.04 (*C*=O).

2,5-di(octadecylamino)1,4-quinone (C18*p*)

Following general methods, the title compound (bright orange) was obtained after purification using 99.5:0.5 chloroform:methanol as eluent. m.p. 100-102 °C; R_f 0.81 (98/2 $CHCl_3$/MeOH); ^{1}H NMR (500 MHz, $CDCl_3$ at 21°C) δ 0.88 (t, ^3J= 7.0 Hz, 6H, C*H*$_3$), 1.2-1.4 (m, 60H, CH_2-C*H*$_2$-CH_2), 1.65 (q, ^3J= 7.3 Hz, 4H, NH-CH_2-C*H*$_2$), 3.15 (quartet, ^3J= 6.7 Hz, 4H, NH-C*H*$_2$), 5.30 (s, 2H, O-C-C*H*), 6.61 (br t, ^3J= 5.5 Hz, 2H, N*H*); ^{13}C NMR (125 MHz, $CDCl_3$ at 21°C) δ = 14.1 (*C*H_3-CH_2), 22.7 (CH_3-*C*H_2), 27.0,

28.3, 29.2, 29.3, 29.4, 29.5, 29.6, 29.7 (*C*$H_2$$CH_2$), 32.0 (NH-$CH_2$-*C*$H_2$), 42.6 (NH-*C*$H_2$-$CH_2$), 92.7 (*C*H=C-NH), 151.4 (CH=*C*-NH), 178.1 (*C*=O), MS (Triple Quad-ESI): m/z: 643.65 $[M+H]^+$ calcd $[M+H]^+$: 643.61.

Bis[4-(octadecylamino)-2-(octadecylimino)-5-oxo-1,4-cyclohexadienolato]nickel ((C18*m*)$_2$Ni)

C18*m* (80.0 mg; 0.124 mmol) was dissolved in toluene (10.0 mL) with Nickel(II) Acetate tetrahydrate **($Ni(OAc)_2$·$4H_2O$**; 28.1 mg; 0.11 mmol). The mixture was left to stir under reflux for 12 hours. After cooling down the solution, the resulting precipitate, purple color with metallic lustre, was isolated by filtering through a Pyrex® Glass Buchner Funnel with medium porosity fritted disc (10-15 μm) and washed with cold chloroform (to remove starting material, **C18*m***), hot water (to remove starting material **$Ni(OAc)_2$**) and dried in air. The crude product (*ca.* 90% pure) was removed from the fritted filter with hot chloroform, transferred to a separatory funnel, toped to about 40 mL with chloroform, and capped to prevent solvent evaporation. **(C18*m*)$_2$Ni** slowly crystallizes out of the solution, and due to the lower density of **(C18*m*)$_2$Ni** with respect to the chloroform, purple precipitate floats to the top of the solution. After one day the bottom red solution containing starting material **C18*m*** is drained, followed by adding another 40 mL of fresh hot chloroform to redissolve **(C18*m*)$_2$Ni** in solution. The process was repeated 3 to 4 times until the bottom solution has only a light pink color. Solvent was drained and the final metallic lustre purple solid was dried under reduced pressure (57.5 mg; 0.086 mmol; 69%). Recrystallization from various solvents was attempted but gave lower purity (95%). Chromatography (Ni complex does not move on Si, Al and cellulose plates) and soxhlet extraction (Ni complex dissolves in most hot solvents) were unsuccessful purification methods.

Reaction with nickel(II) hydroxide **$Ni(OH)_2$** in solvent was using the same procedure.

The mechanochemical synthesis of **(C18*m*)$_2$Ni** is as described in the general method B,C, and D above.

m.p. > 200 °C; R_f 0 (98/2 $CHCl_3$/MeOH); ^{1}H NMR (500 MHz, $CDCl_3$ at 45°C) δ 0.88 (t, ^3J= 7.0 Hz, 12H, CH_3), 1.20-1.65 (m, 128H, CH_2-CH_2-CH_3), 2.84 (br t, ^3J= 7.3 Hz, 4H, NH-CH_2), 3.07 (q, ^3J= 6.7 Hz, 4H, NH-CH_2), 5.02 (s, 2H, NH-C-C*H*), 5.22 (s, 2H, O-C-C*H*), 6.26 (br t, 2H, N*H*); ^{13}C NMR (125 MHz, $CDCl_3$ at 45°C) δ = 14.06, 22.72 (*C*H_3-CH_2), 27.14, 27.39 (CH3-*C*H2), 28.44, 29.33, 29.39, 29.40, 29.47, 29.54, 29.62, 29.66, 29.69, 29.72, 29.73, 29.75, 29.78, 29.93, 31.99 (*C*H_2CH_2), 42.70, 47.74 (NH-*C*H_2), 83.27 (H*C*=C), 102.55(H*C*=C), 146.73 (C-N), 167.29 (*C*-O), 180.25 (C=N), 180.60 (*C*=O); MS (MALDI): m/z: 1342.51 $[M+H]^+$ calcd $[M+H]^+$: 1342.14

Chapter 5. Conclusion

We have presented detailed STM investigation of the self-assembly of aminobenzoquinone derivatives at the solid/liquid interface, followed by the development of green, solvent-free synthetic strategies for both *para* and *meta* aminobenzoquinones and an aminobenzoquinone metal complex. The reaction times are significantly reduced, applying solvent-free mechanochemistry. In a matter of minutes, yields comparable to what normally takes hours in solution were obtained. Furthermore, it was found that the reaction temperature attained during the shaking process can be an important factor to consider when optimizing mechanochemistry reaction conditions.

We systematically determined the complementary and sometimes competing role of the hydrogen-bonding functional groups and the long alkyl chains of these quinone molecules, which dictate their self-assembly on graphite, as revealed by STM visualization at the sub-molecular scale. The resulting self-assembled patterns can be explained very well in terms of the strength of intermolecular interactions among molecules and the adsorption energy of the molecules on graphite. In particular, for the first time, the double-decker packing of the alkyl chains in interdigitated lamellae was proposed. In addition, we have shown the formation of mirror image domains or pseudoracemic domains, depending on whether the lamella follows one of the main axes of graphite. This work provides general guidelines for the formation of specific molecular motifs with a variety of molecules governed by hydrogen bonding (or charge assisted hydrogen bonding) with van der Waals interactions. The study not only boosts and unveils the knowledge associated with quinone chemistry but also opens the possibility of utilizing quinone molecules as materials for surface modification, functionalization, crystal growth as well as potential molecule-based device applications.

Chapter 6. References

(1) Ho, W. *J. Chem. Phys.* **2002**, *117*, 11033–11061.
(2) Zandvliet, H. J. W.; Van Houselt, A. *Annu. Rev. Anal. Chem.* **2009**; 2, 37–55.
(3) Katoh, K.; Yoshida, Y.; Yamashita, M.; Miyasaka, H.; Breedlove, B. K.; Kajiwara, T.; Takaishi, S.; Ishikawa, N.; Isshiki, H.; Zhang, Y. F.; Komeda, T.; Yamagishi, M.; Takeya, J. *J. Am. Chem. Soc.* **2009**, *131*, 9967–9976.
(4) Flory, C. A. *Phys. Rev. B* **2006**, *74*.
(5) Paz, O.; Brihuega, I.; Gomez-Rodriguez, J. M.; Soler, J. M. *Phys. Rev. Lett.* **2005**, *94*.
(6) Binnig, G.; Rohrer, H. *Helvetica Phys. Acta* **1982**, *55*, 726–735.
(7) Binnig, G.; Quate, C. F.; Gerber, C. *Phys. Rev. Lett.* **1986**, *56*, 930–933.
(8) Hou, J. G.; Zhao, A. *Nano* **2006**, *1*, 15–33.
(9) Venema, L. C.; Wildoer, J. W. G.; Dekker, C.; Rinzler, G. A.; Smalley, R. E. *Appl. Phys. A* **1998**, *66*, S153–S155.
(10) Binnig, G. K. *Phys. Scr.* **1987**, *T19A*, 53–54.
(11) The Nobel Prize in Physics 1986 http://www.nobelprize.org/nobel_prizes/physics/laureates/1986/presentation-speech.html (accessed September 1, 2013)
(12) Eigler, D. M.; Schweizer, E. K. *Nature* **1990**, *344*, 524–526.
(13) Crommie, M. F.; Lutz, C. P.; Eigler, D. M. *Science* **1993**, *262*, 218–220.
(14) Fischer, O.; Kugler, M.; Maggio-Aprile, I.; Berthod, C.; Renner, C. *Rev. Mod. Phys.* **2007**, *79*, 353–419.
(15) Bocquet, M. L.; Wang, B. *Prog. Surf. Sci.* **2010**, *85*, 435–459.
(16) Girard, C. *Reports Prog. Phys.* **2005**, *68*, 1883–1933.
(17) Repp, J.; Meyer, G.; Stojkovic, S. M.; Gourdon, A.; Joachim, C. *Phys. Rev. Lett.* **2005**, *94*.
(18) Joachim, C.; Gimzewski, J. K.; Aviram, A. *Nature* **2000**, *408*, 541–548.
(19) Griessl, S.; Lackinger, M.; Edelwirth, M.; Hietschold, M.; Heckl, W. M. *Single Mol.* **2002**, *3*, 25–31.
(20) Hamers, R. J. *Annu. Rev. Phys. Chem.* **1989**, *40*, 531–559.
(21) Schöck, M.; Otero, R.; Stojkovic, S.; Hümmelink, F.; Gourdon, A.; Stensgaard, I.; Joachim, C.; Besenbacher, F. *J. Phys. Chem. B* **2006**, *110*, 12835–12838.
(22) Yokoyama, T.; Yokoyama, S.; Kamikado, T.; Okuno, Y.; Mashiko, S. *Nature* **2001**, *413*, 619–621.
(23) Ivasenko, O.; Perepichka, D. F. *Chem. Soc. Rev.* **2011**, *40*, 191–206.
(24) Grabowski, S. *Hydrogen bonding - New insights*; Springer: Dordrecht, 2006.
(25) MacDonald, J. C.; Dorrestein, P. C.; Pilley, M. M. *Cryst. Growth & Des.* **2000**, *1*, 29–38.
(26) Dunitz, J. D. *Chem. Commun.* **2003**, 545–548.
(27) Dunitz, J. D.; Gavezzotti, A. *Angew. Chem., Int. Ed.* **2005**, *44*, 1766–1787.
(28) Ward, M. D. *Chem. Commun.* **2005**, 5838–5842.

(29) Dmitriev, A.; Lin, N.; Weckesser, J.; Barth, J. V.; Kern, K. *J. Phys. Chem. B* **2002**, *106*, 6907–6912.
(30) Griessl, S. J. H.; Lackinger, M.; Jamitzky, F.; Markert, T.; Hietschold, M.; Heckl, W. M. *Langmuir* **2004**, *20*, 9403–9407.
(31) Griessl, S. J. H.; Lackinger, M.; Jamitzky, F.; Markert, T.; Hietschold, M.; Heckl, W. M. *J. Phys. Chem. B* **2004**, *108*, 11556–11560.
(32) Nath, K. G.; Ivasenko, O.; Miwa, J. A.; Dang, H.; Wuest, J. D.; Nanci, A.; Perepichka, D. F.; Rosei, F. *J. Am. Chem. Soc.* **2006**, *128*, 4212–4213.
(33) Mali, K. S.; Lava, K.; Binnemans, K.; De Feyter, S. *Chem. Eur. J.* **2010**, *16*, 14447–14458.
(34) Lackinger, M.; Griessl, S.; Heckl, W. M.; Hietschold, M.; Flynn, G. W. *Langmuir* **2005**, *21*, 4984–4988.
(35) MacLeod, J. M.; Ivasenko, O.; Perepichka, D. F.; Rosei, F. *Nanotechnology* **2007**, *18*.
(36) Fang, Y.; Phuong, N.; Ivasenko, O.; Aviles, M. P.; Kebede, E.; Askari, M. S.; Ottenwaelder, X.; Ziener, U.; Siri, O.; Cuccia, L. A. *Chem. Commun.* **2011**, *47*, 11255–11257.
(37) Harmuth, L. Dictionary of textiles; Fairchild publishing company: New York, 1915; pp 106.
(38) Amidror, I. *The theory of the Moiré phenomenon*; Springer: Netherlands, 2007.
(39) Delhaes, P. *Graphite and Precursors*; CRC Press: Singapore 2001.
(40) Batra, I. P.; Garcia, N.; Rohrer, H.; Salemink, H.; Stoll, E.; Ciraci, S. *Surf. Sci.* **1987**, *181*, 126–138.
(41) Saito, R.; Grüneis, A.; Samsonidze, G. G.; Dresselhaus, G.; Dresselhaus, M. S.; Jorio, A.; Cançado, L. G.; Pimenta, M. A.; Souza Filho, A. G. *Appl. Phys.* **2004**, *78*, 1099–1105.
(42) Kuwabara, M.; Clarke, D. R.; Smith, D. A. *Appl. Phys. Lett.* **1990**, *56*, 2396–2398.
(43) Liu, C. Y.; Chang, H. P.; Bard, A. J. *Langmuir* **1991**, *7*, 1138–1142.
(44) Pong, W.-T.; Durkan, C. *J. Phys. D-Applied Phys.* **2005**, *38*, R329–R355.
(45) Cyr, D. M.; Venkataraman, B.; Flynn, G. W. *Chem. Mater.* **1996**, *8*, 1600–1615.
(46) De Feyter, S.; Gesquiere, A.; Abdel-Mottaleb, M. M.; Grim, P. C. M.; De Schryver, F. C.; Meiners, C.; Sieffert, M.; Valiyaveettil, S.; Mullen, K. *Acc. Chem. Res.* **2000**, *33*, 520–531.
(47) Wawkuschewski, A.; Cantow, H. J.; Magonov, S. N.; Sheiko, S. S.; Moller, M. *Polym. Bull.* **1993**, *31*, 699–705.
(48) Magonov, S. N.; Wawkuschewski, A.; Cantow, H. J.; Liang, W.; Whangbo, M. H. *Appl. Phys. A.* **1994**, *59*, 119–133.
(49) Tahara, K.; Inukai, K.; Hara, N.; Johnson, C. A. II.; Haley, M. M.; Tobe, Y. *Chem. Eur. J.* **2010**, *16*, 8319–8328.
(50) Yuan, Z.; Lee, S.-L.; Chen, L.; Li, C.; Mali, K. S.; De Feyter, S.; Müllen, K. *Chem. Eur. J.* **2013**, *19*, 11842.
(51) Chen, T.; Pan, G.-B.; Wettach, H.; Fritzsche, M.; Hoeger, S.; Wan, L.-J.; Yang,

H.-B.; Northrop, B. H.; Stang, P. J. *J. Am. Chem. Soc.* **2010**, *132*, 1328–1333.
(52) Piot, L.; Marie, C.; Feng, X.; Muellen, K.; Fichou, D. *Adv. Mater.* **2008**, *20*, 3854.
(53) Crivillers, N.; Furukawa, S.; Minoia, A.; Heyen, A. V.; Mas-Torrent, M.; Sporer, C.; Linares, M.; Volodin, A.; Van Haesendonck, C.; Van der Auweraer, M.; Lazzaroni, R.; De Feyter, S.; Veciana, J.; Rovira, C. *J. Am. Chem. Soc.* **2009**, *131*, 6246–6252.
(54) Samori, P.; Severin, N.; Simpson, C. D.; Mullen, K.; Rabe, J. P. *J. Am. Chem. Soc.* **2002**, *124*, 9454–9457.
(55) Faglioni, F.; Claypool, C. L.; Lewis, N. S.; Goddard, W. A. *J. Phys. Chem. B* **1997**, *101*, 5996–6020.
(56) Blunt, M. O.; Russell, J. C.; Gimenez-Lopez, M. del C.; Taleb, N.; Lin, X.; Schroder, M.; Champness, N. R.; Beton, P. H. *Nat. Chem.* **2011**, *3*, 74–78.
(57) Weiss, C.; Wagner, C.; Kleimann, C.; Rohlfing, M.; Tautz, F. S.; Temirov, R. *Phys. Rev. Lett.* **2010**, *105*.
(58) Yoshimoto, S.; Tsutsumi, E.; Suto, K.; Honda, Y.; Itaya, K. *Chem. Phys.* **2005**, *319*, 147–158.
(59) Ivasenko, O.; MacLeod, J. M.; Chernichenko, K. Y.; Balenkova, E. S.; Shpanchenko, R. V.; Nenajdenko, V. G.; Rosei, F.; Perepichka, D. F. *Chem. Commun.* **2009**, 1192–1194.
(60) Piot, L.; Marchenko, A.; Wu, J. S.; Mullen, K.; Fichou, D. *J. Am. Chem. Soc.* **2005**, *127*, 16245–16250.
(61) Lee, S.-L.; Chu, Y.-C.; Wu, H.-J.; Chen, C.-H. *Langmuir* **2012**, *28*, 382–388.
(62) Clark, J. H. *Green Chem.* **2006**, *8*, 17–21.
(63) Mack, J.; Shumba, M. *Green Chem.* **2007**, *9*, 328–330.
(64) Mack, J.; Fulmer, D.; Stofel, S.; Santos, N. *Green Chem.* **2007**, *9*, 1041–1043.
(65) Tanaka, K.; Toda, F. *Chem. Rev.* **2000**, *100*, 1025–1074.
(66) Kaupp, G.; Naimi-Jamal, M. R.; Stepanenko, V. *Chem. Eur. J.* **2003**, *9*, 4156–4160.
(67) Friščić, T. Chem. Soc. Rev., **2012**, *41*, 3493.
(68) Swinburne, A. N.; Steed, J. W. *CrystEngComm* **2009**, *11*, 433–438.
(69) Beyer, M. K.; Clausen-Schaumann, H. *Chem. Rev.* **2005**, *105*, 2921–2948.
(70) Ostwald, W. *Textbook of General Chemistry*; Engelmann: Leipzig, 1885.
(71) Bruckmann, A.; Krebs, A.; Bolm, C. *Green Chem.* **2008**, *10*.
(72) Urakaev, F. K.; Boldyrev, V. V. *Powder Technol.* **2000**, *107*, 197–206.
(73) Lehn, J.-M. *Supramolecular Chemistry: Concepts and Perspectives*; Wiley-VCH: Weinheim, 1995.
(74) Elemans, J. A. A. W.; De Cat, I.; Xu, H.; De Feyter, S. *Chem. Soc. Rev.* **2009**, *38*, 722–736.
(75) Wang, D.; Wan, L. J.; Bai, C. L. *Mater. Sci. Eng., R* **2010**, *70*, 169–187.
(76) Son, S. U.; Reingold, J. A.; Carpenter, G. B.; Czech, P. T.; Sweigart, D. A. *Organometallics* **2006**, *25*, 5276–5285.
(77) Ward, M. D. *Struct. Bond.* **2009**, *132*, 1–23.
(78) Gilli, G.; Gilli, P. *J. Mol. Struct.* **2000**, *552*, 1–15.

(79) Gilli, G.; Gilli, paola *The Nature of the Hydrogen Bond*; Oxford University Press Inc.: New York, 2009.
(80) Nazmutdinov, R. R.; Zhang, J. D.; Zinkicheva, T. T.; Manyurov, I. R.; Ulstrup, J. *Langmuir* **2006**, *22*, 7556–7567.
(81) Schiffrin, A.; Riemann, A.; Auwarter, W.; Pennec, Y.; Weber-Bargioni, A.; Cvetko, D.; Cossaro, A.; Morgante, A.; Barth, J. V. *Proc. Natl. Acad. Sci. United States Am.* **2007**, *104*, 5279–5284.
(82) Xu, S. M.; Chen, M. H.; Cholewa, E.; Szymanski, G.; Lipkowski, J. *Langmuir* **2007**, *23*, 6937–6946.
(83) Makoudi, Y.; Didiot, C.; Palmino, F.; Duverger, E.; Kierren, B.; Malterre, D.; Chérioux, F. *Surf. Sci.* **2010**, *604*, 27–31.
(84) Siri, O.; Braunstein, P. *Chem. Commun.* **2002**, 208–209.
(85) Xiao, J.; Zhang, Z.; Wu, D.; Routaboul, L.; Braunstein, P.; Doudin, B.; Losovyj, Y. B.; Kizilkaya, O.; Rosa, L. G.; Borca, C. N.; Gruverman, A.; Dowben, P. A. *Phys. Chem. Chem. Phys.* **2010**, *12*, 10329–10340.
(86) Zhang, Z. Z.; Alvira, J.; Barbosa, X.; Rosa, L. G.; Routaboul, L.; Braunstein, P.; Doudin, B.; Dowben, P. A. *J. Phys. Chem. C* **2011**, *115*, 2812–2818.
(87) Yang, Q. Z.; Siri, O.; Braunstein, P. *Chem. Commun.* **2005**, 2660–2662.
(88) Yang, Q. Z.; Siri, O.; Braunstein, P. *Chem. Eur. J.* **2005**, *11*, 7237–7246.
(89) Nath, K. G.; Ivasenko, O.; MacLeod, J. M.; Miwa, J. A.; Wuest, J. D.; Nanci, A.; Perepichka, D. F.; Rosei, F. *J. Phys. Chem. C* **2007**, *111*, 16996–17007.
(90) Stawasz, M. E.; Sampson, D. L.; Parkinson, B. A. *Langmuir* **2000**, *16*, 2326–2342.
(91) De Feyter, S.; Gesquiere, A.; Klapper, M.; Mullen, K.; De Schryver, F. C. *Nano Lett.* **2003**, *3*, 1485–1488.
(92) Thalacker, C.; Miura, A.; De Feyter, S.; De Schryver, F. C.; Wurthner, F. *Org. & Biomol. Chem.* **2005**, *3*, 414–422.
(93) Stepanow, S.; Lin, N.; Vidal, F.; Landa, A.; Ruben, M.; Barth, J. V.; Kern, K. *Nano Lett.* **2005**, *5*, 901–904.
(94) Gong, J. R.; Wan, L. J. *J. Phys. Chem. B* **2005**, *109*, 18733–18740.
(95) Cornilescu, G.; Ramirez, B. E.; Frank, M. K.; Clore, G. M.; Gronenborn, A. M.; Bax, A. *J. Am. Chem. Soc.* **1999**, *121*, 6275–6279.
(96) Klappenberger, F.; Canas-Ventura, M. E.; Clair, S.; Pons, S.; Schlickum, U.; Qu, Z. R.; Strunskus, T.; Comisso, A.; Woll, C.; Brune, H.; Kern, K.; De Vita, A.; Ruben, M.; Barth, J. V. *ChemPhysChem* **2008**, *9*, 2522–2530.
(97) Lei, S.; Puigmarti-Luis, J.; Minoia, A.; Van der Auweraer, M.; Rovira, C.; Lazzaroni, R.; Amabilino, D. B.; De Feyter, S. *Chem. Commun.* **2008**, 703–705.
(98) Li, Y. L.; Liu, L.; Subramani, R.; Pan, Y. X.; Liu, B.; Yang, Y. L.; Wang, C.; Mamdouh, W.; Besenbacher, F.; Dong, M. D. *Chem. Commun.* **2011**, *47*, 9155–9157.
(99) Mas-Torrent, M.; Rovira, C. *Chem. Rev.* **2011**, *111*, 4833–4856.
(100) De Luca, G.; Pisula, W.; Credgington, D.; Treossi, E.; Fenwick, O.; Lazzerini, G. M.; Dabirian, R.; Orgiu, E.; Liscio, A.; Palermo, V.; Mullen, K.; Cacialli, F.;

Samori, P. *Adv. Funct. Mater.* **2011**, *21*, 1279–1295.
(101) Whitesides, G. M.; Boncheva, M. *Proc. Natl. Acad. Sci. USA* **2002**, *99*, 4769–4774.
(102) Ariga, K.; Lee, M. V.; Mori, T.; Yu, X.-Y.; Hill, J. P. *Adv. Colloid Interface Sci.* **2010**, *154*, 20–29.
(103) Elemans, J. A. A. W.; Lei, S.; De Feyter, S. *Angew. Chemie Int. Ed. Engl.* **2009**, *48*, 7298–7332.
(104) Lin, N.; Stepanow, S.; Ruben, M.; Barth, J. V. *Top. Curr. Chem.*, **2009**, *287*, pp. 1–44.
(105) Mali, K. S.; Lava, K.; Binnemans, K. *Chem. Eur. J.* **2010**, *16*, 14447-14458.
(106) Barbosa, L. C. A.; Pereira, U. A.; Maltha, C. R. A.; Teixeira, R. R.; Valente, V. M. M.; Ferreira, J. R. O.; Costa-Lotufo, L. V.; Moraes, M. O.; Pessoa, C. *Molecules* **2010**, *15*, 5629–5643.
(107) Schweinfurth, D.; Das, H. S.; Weisser, F.; Bubrin, D.; Sarkar, B. *Inorg. Chem.* **2011**, *50*, 1150–1159.
(108) Barba, V.; Zaragoza, J.; Hopfl, H.; Farfan, N.; Beltran, H. I.; Zamudio-Rivera, L. S. *J. Organomet. Chem.* **2011**, *696*, 1949–1956.
(109) Fang, Y.; Nguyen, P.; Ivasenko, O.; Aviles, M. P.; Kebede, E.; Askari, M. S.; Ottenwaelder, X.; Ziener, U.; Siri, O.; Cuccia, L. A. *Chem. Commun.* **2011**, *47*, 11255–11257.
(110) Routaboul, L.; Braunstein, P.; Xiao, J.; Zhang, Z. Z.; Dowben, P. A.; Dalmas, G.; Da Costa, V.; Felix, O.; Decher, G.; Rosa, L. G.; Doudin, B. *J. Am. Chem. Soc.* **2012**, *134*, 8494–8506.
(111) Dowben, P.; Kunkel, D.; Enders, A.; Rosa, L.; Routaboul, L.; Doudin, B.; Braunstein, P. *Top. Catal.* **2013**, 1–8.
(112) Puigmarti-Luis, J.; Minoia, A.; Lei, S. B.; Geskin, V.; Li, B.; Lazzaroni, R.; De Feyter, S.; Amabilino, D. B. *Chem. Sci.* **2011**, *2*, 1945–1951.
(113) Thomson, R. H. *Naturally Occurring Quinones IV, Recent Advances*; Springer: Netherlands, 1997.
(114) Yang, Q. Z.; Kermagoret, A.; Agostinho, M.; Siri, O.; Braunstein, P. *Organometallics* **2006**, *25*, 5518–5527.
(115) MacLeod, J. M.; Ben Chaouch, Z.; Perepichka, D. F.; Rosei, F. *Langmuir* **2013**, *29*, 7318–7324.
(116) Barlow, S. M.; Raval, R. *Surf. Sci. Reports* **2003**, *50*, 201–341.
(117) Horcas, I.; Fernández, R.; Gómez-Rodríguez, J. M.; Colchero, J.; Gómez-Herrero, J.; Baro, A. M. *Rev. Sci. Instrum.* **2007**, *78*, 013705–1.
(118) Sugandhi, E. W.; Macri, R. V.; Williams, A. A.; Kite, B. L.; Slebodnick, C.; Falkinham, J. O.; Esker, A. R.; Gandour, R. D. *J. Med. Chem.* **2007**, *50*, 1645–1650.
(119) Oh, M.; Carpenter, G. B.; Sweigart, D. A. *Accounts Chem. Res.* **2003**, *37*, 1–11.
(120) Stahl, P.; Kissau, L.; Mazitschek, R.; Giannis, A.; Waldmann, H. *Angew. Chem. Int. Ed.* **2002**, *41*, 1174–1178.
(121) Ling, T.; Poupon, E.; Rueden, E. J.; Kim, S. H.; Theodorakis, E. A. *J. Am. Chem.*

Soc. **2002**, *124*, 12261–12267.
(122) Patai, S. E. *The chemistry of the quinonoid compounds*; Vol. 1; Wiley: New York, 1974.
(123) Holtzl, T.; Veszpremi, T.; Nguyen, M. T. *J. Phys. Org. Chem.* **2005**, *18*, 1123–1131.
(124) Luo, S. H.; Liu, Y.; Hua, J.; Niu, X. M.; Jing, S. X.; Zhao, X.; Schneider, B.; Gershenzon, J.; Li, S. H. *Org. Lett.* **2012**, *14*, 4146–4149.
(125) Braunstein, P.; Siri, O. WO patent 2002072533 2002; *SciFinder Scholar* 2002:716235.
(126) Meazza, G.; Scheffler, B. E.; Tellez, M. R.; Rimando, A. M.; Romagni, J. G.; Duke, S. O.; Nanayakkara, D.; Khan, I. A.; Abourashed, E. A.; Dayan, F. E. *Phytochemistry* **2002**, *60*, 281–288.
(127) Niels, U.; Tokita, S.; Matsuura, K. *Biochim. et Biophys. Acta* **1999**, *1413*, 108–116.
(128) Johnson, J.; Gandhidasan, I.; Murugesan, R. *Free. Radic. Biol. Med.* **1999**, *26*, 1072–1078.
(129) Subbarayudu, N.; Satyanarayana, Y. D.; Venkata Rao, E.; Venkata Rao, D. *Indian J. Pharm. Sci.* **1978**, *40*, 173–175.
(130) Bachur, N. R.; Gordon, S. L.; Gee, M. V. *Cancer Res.* **1978**, *38*, 1745–1750.
(131) Joshi, B. S.; Kamat, V. N. *Indian J. Chem.* **1975**, *13*, 795–800.
(132) Constantinides, C. P.; Koutentis, P. A.; Schatz, J. *J. Am. Chem. Soc.* **2004**, *126*, 16232–16241.
(133) Haas, Y.; Zilberg, S. *J. Am. Chem. Soc.* **2004**, *126*, 8991–8998.
(134) Delaere, D.; Nam, P. C.; Nguyen, M. T. *Chem. Phys. Lett.* **2003**, *382*, 349–354.
(135) Le, H. T.; Nam, P. C.; Dao, V. L.; Veszpremi, T.; Nguyen, M. T. *Mol. Phys.* **2003**, *101*, 2347–2355.
(136) Sawicka, A.; Skurski, P.; Simons, J. *Chem. Phys. Lett.* **2002**, *362*, 527–533.
(137) Yang, Q. Z.; Siri, O.; Brisset, H.; Braunstein, P. *Tetrahedron Lett.* **2006**, *47*, 5727–5731.
(138) Tamboura, F. B.; Cazin, C. S. J.; Pattacini, R.; Braunstein, P. *Eur. J. Org. Chem.* **2009**, 3340–3350.
(139) Braunstein, P.; Siri, O.; Steffanut, P.; Winter, M.; Yang, Q. Z. *Comptes Rendus Chim.* **2006**, *9*, 1493–1499.
(140) Braunstein, P.; Siri, O.; Taquet, J.; Rohmer, M.-M.; Bénard, M.; Welter, R. *J. Am. Chem. Soc.* **2003**, *125*, 12246–12256.
(141) Braunstein, P.; Siri, O.; Taquet, J.; Yang, Q.-Z. *Chem. Eur. J.* **2004**, *10*, 3817–3821.
(142) Taquet, J.-P.; Siri, O.; Braunstein, P.; Welter, R. *Inorg. Chem.* **2004**, *43*, 6944–6953.
(143) Kong, L. M.; Medina, G. J. P.; Santana, J. A. C.; Wong, F.; Bonilla, M.; Amill, D. A. C.; Rosa, L. G.; Routaboul, L.; Braunstein, P.; Doudin, B.; Lee, C. M.; Choi, J.; Xiao, J.; Dowben, P. A. *Carbon* **2012**, *50*, 1981–1986.

(144) Taquet, J. P.; Siri, O.; Braunstein, P.; Welter, R. *Inorg. Chem.* **2006**, *45*, 4668–4676.
(145) Ott, R.; Pinter, E. *Monatsh. Chem.* **1997**, *128*, 901–909.
(146) Anslow, W. K.; Raistrick, H. *J. Chem. Soc.* **1939**, 1446–57.
(147) Zvejnieks, A. *Sven. Kem. Tidskr.* **1954**, *66*, 316–22.
(148) Bayen, S.; Barooah, N.; Sarma, R. J.; Sen, T. K.; Karmakar, A.; Baruah, J. B. *Dyes Pigm.* **2007**, *75*, 770–775.

Chapter 7. Appendix I

X-ray structure and crystallographic data

A red plate-like specimen of **C18*m*** ($C_{43}H_{81}Cl_3N_2O_3$), approximate dimensions 0.070 mm x 0.100 mm x 0.120 mm, was used for the X-ray crystallographic analysis. The X-ray intensity data were measured on a Bruker SMART APEX II CCD system equipped with a Cu ImuS microfocus source with QUAZAR optics (λ = 1.54178 Å). A total of 7320 frames were collected. The total exposure time was 20.33 hours. The frames were integrated with the Bruker SAINT software package using a narrow-frame algorithm. The integration of the data using a triclinic unit cell yielded a total of 45090 reflections to a maximum θ angle of 68.16° (0.83 Å resolution), of which 15653 were independent (average redundancy 2.881, completeness = 94.1%, R_{int} = 4.64%, R_{sig} = 5.33%) and 9911 (63.32%) were greater than $2\sigma(F^2)$. The final cell constants of $\underline{a}$ = 9.53790(10) Å, $\underline{b}$ = 15.4567(2) Å, $\underline{c}$ = 31.2770(4) Å, α = 80.4140(10)°, β = 89.3420(10)°, γ = 87.0510(10)°, volume = 4540.57(10) $Å^3$, are based upon the refinement of the XYZ-centroids of 9965 reflections above 20 σ(I) with 5.731° < 2θ < 135.0°. Data were corrected for absorption effects using the multi-scan method (SADABS). The ratio of minimum to maximum apparent transmission was 0.920. The calculated minimum and maximum transmission coefficients (based on crystal size) are 0.7788 and 0.8615. The structure was solved and refined using the Bruker SHELXTL Software Package, using the space group P -1, with Z = 4 for the formula unit, $C_{43}H_{81}Cl_3N_2O_3$. The final anisotropic full-matrix least-squares refinement on F^2 with 956 variables converged at R1 = 5.20%, for the observed data and wR2 = 14.13% for all data. The goodness-of-fit was 1.014. The largest peak in the final difference electron density synthesis was 0.459 $e^-/Å^3$ and the largest hole was -0.380 $e^-/Å^3$ with an RMS deviation of 0.047 $e^-/Å^3$. On the basis of the final model, the calculated density was 1.142 g/cm^3 and F(000), 1712 e^-.

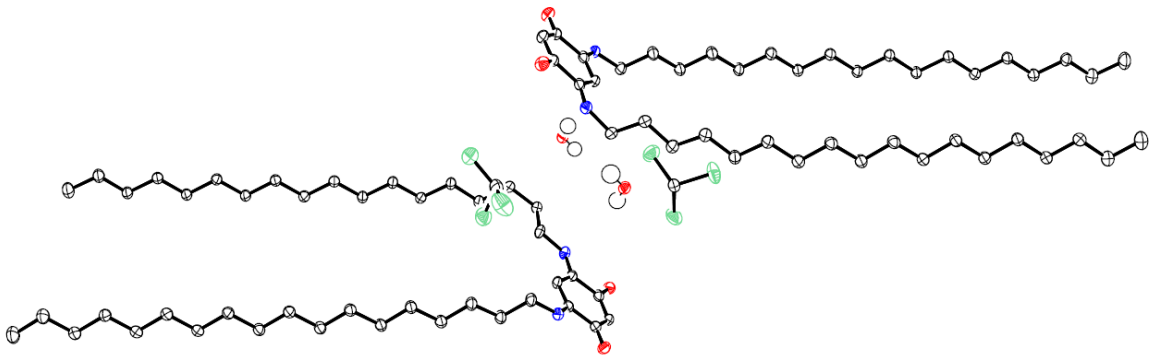

Figure 1. Crystal structure of **C18*m*** at 50% ellipsoid probability.

Table SI-1: Crystal data and structure refinement for **C18Q**

Empirical formula	$C_{42}H_{78}N_2O_2 \cdot CHCl_3 \cdot H_2O$	
Formula weight	780.45	
Temperature	116(2) K	
Wavelength	1.54178 Å	
Crystal system	Triclinic	
Space group	P(-1)	
Unit cell dimensions	a = 9.53790(10) Å b = 15.4567(2) Å c = 31.2770(4) Å	α = 80.4140(10)° β = 89.3420(10)° γ = 87.0510(10)°
Volume	4540.57(10) Å^3	
Z	4	
Density (calculated)	1.142	
Absorption coefficient	2.105	
F(000)	1712	
Crystal size	0.12 × 0.10 × 0.07 mm	
Theta range for data collection	1.43 – 68.16	
Index ranges	h = −11→11, k = −16→18, l = −37→37	
Reflections collected	45090	
Independent reflections	15653	
Completeness to theta = 68.16°	94.1%	
Absorption correction	Multiscan	
Refinement method	Full-matrix least-squares on F^2	

Data / restraints / parameters	15653 / 0 / 955
Goodness of fit on F^2	1.014
Final R indices [$I > 2\sigma(I)$]	$R_1 = 5.20\%$, $wR_2 = 12.05\%$
R indices (all data)	$R_1 = 9.31\%$, $wR_2 = 14.13\%$
Largest diff. peak and hole	0.46 and -0.38 e $Å^{-3}$

Chapter 8. Appendix II

How to calibrate an STM image using WSxM 5.0 Develop 5.3

Proper calibration of STM images can never be stressed enough. WSxM, a free software, works as well as the commercially available SPIP software. WSxM can be conveniently downloaded from the WSxM official website.[117]

Two calibration methods are explained in this tutorial:

Method I:

Requirement: 1) One half-half image – Imaging self-assembled monolayer (SAM) to midway followed by immediately changing the voltage to view the underlying graphite substrate. More reliable results are obtained after the instrument has been stabilized/equilibrated by repeating several scans in the same area.

Method II:

Requirement: 1) One SAM image, 2) one HOPG image

In this case, it is highly recommended for both images to have the same dimension, scan direction (both scan up or both scan down) and both images should be sequential. N.B. calibration steps that are identical with those in method I are not repeated to save space.

Method I:

Step 1: The process is started by first **opening an STM image file (Figure 1)**: 

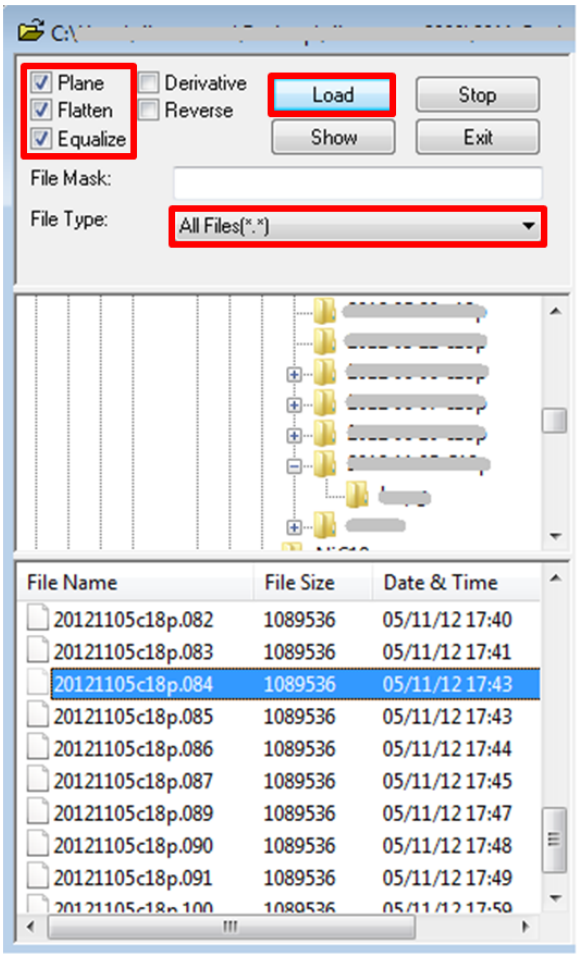

Figure 1. File opening window

In the above menu, check on **Plane Flatten** and **Equalize**, so that all the images that are opened will be automatically pre-processed. Choose the correct file type, select a file and load.

N.B.: Depending on the file format, a message may appear asking if you would like to extract the files. Click on **load**.

Tips: After selecting the **Plane, Flatten** and **Equalize** in the file opening window, close it. Images can be **dragged** onto the program window and they will be pre-processed as well.

The opened file should look like Figure 2.

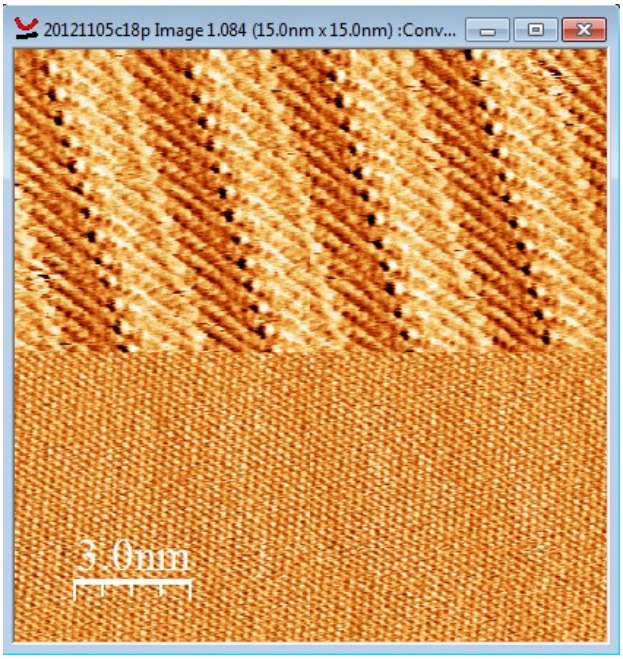

Figure 2. Half-half image. STM current image of **C18*p*** at the TCB/HOPG interface. The bias voltage was changed during scanning, revealing atomic resolution of the HOPG. 15 nm × 15 nm; I_t = 18 pA. V_b = -350 mV (SAM). I_t =18 pA, V_b = 40 mV (HOPG).

Step2: 2D Fast Fourier transform the image: 2D FFT 

2D FFT helps to find the repeating pattern in an image.

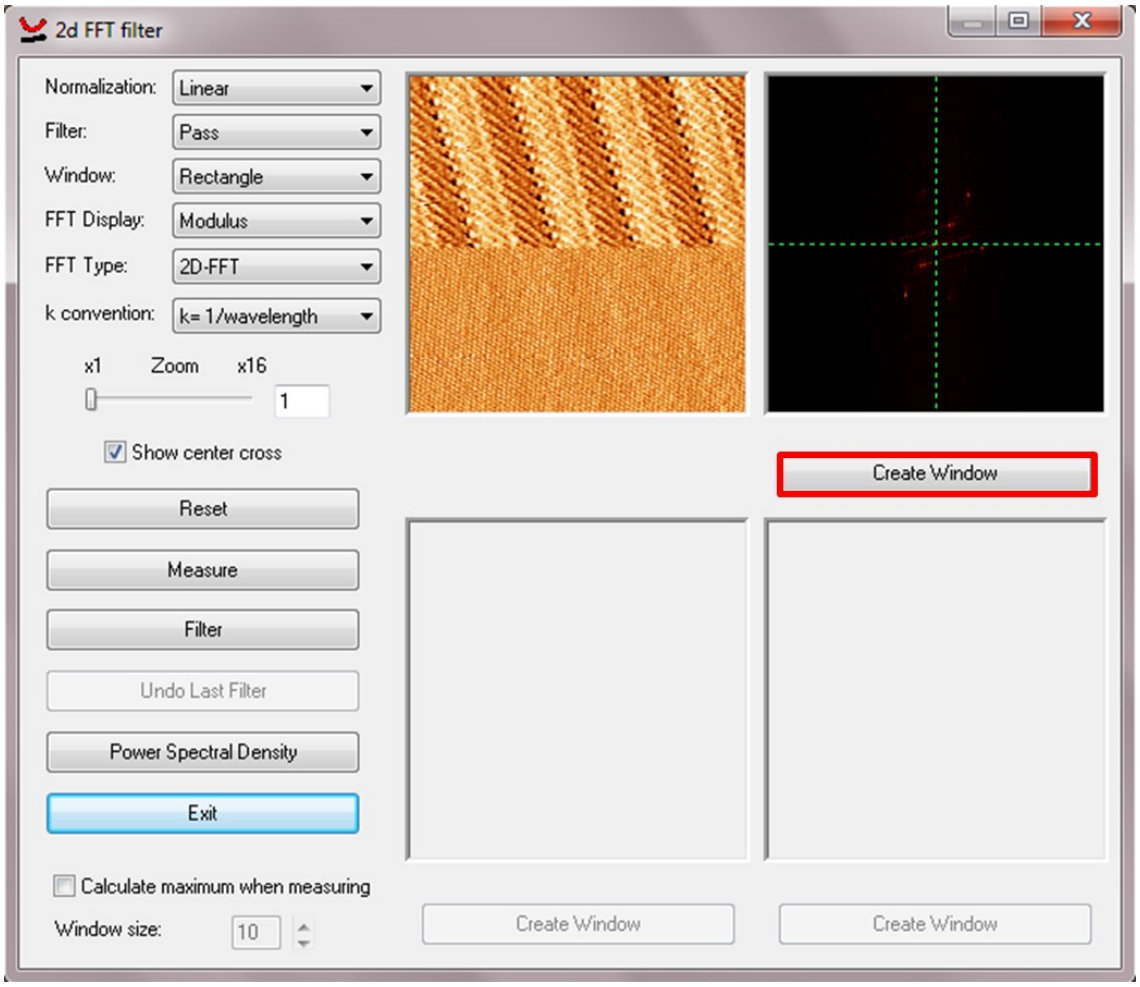

Figure 3. 2D FFT filter window for half-half image.

In the above menu (Figure **3**), click on **Create Window**.

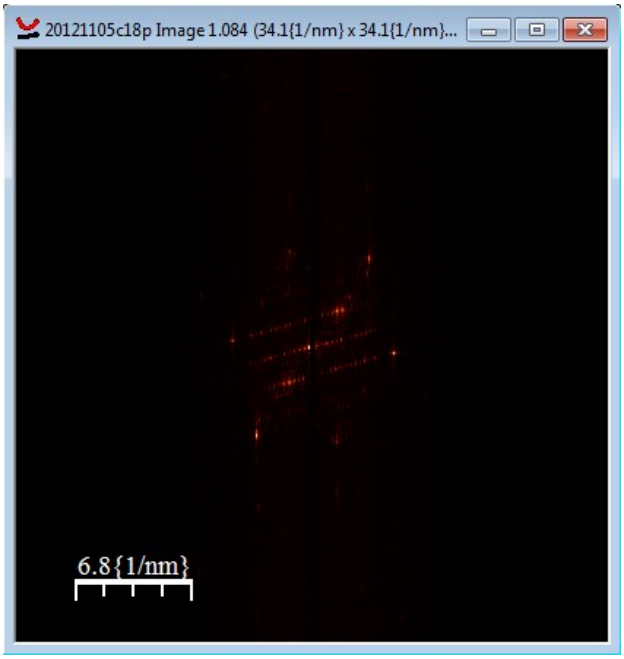

Figure 4. 2D FFT image of the half-half image

A 2D FFT image of the half-half image will look similar to Figure **4**. The 6 outer spots showing the symmetry or repeating pattern of HOPG, while the inner pattern decodes the repeating pattern(s) within the SAM.

Step 3: Zoom in: 

Press Shift (to get a square selection tool) and hold the left mouse key to select a region of interest (Figure **5**).

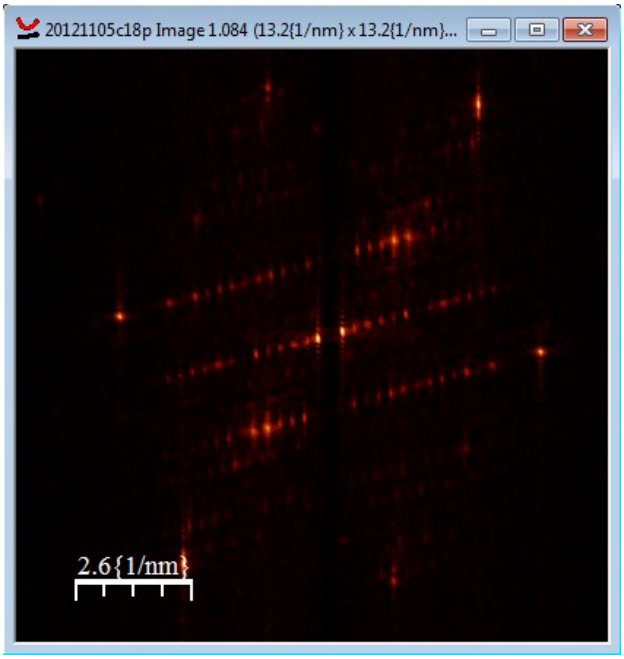

Figure 5. Enlarged 2D FFT image

Step 4: Rotate 90°: 

Using the rotation menu (Figure **6**). The rotated image is shown in Figure **7**.

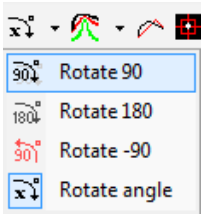

Figure 6. Rotation angle menu

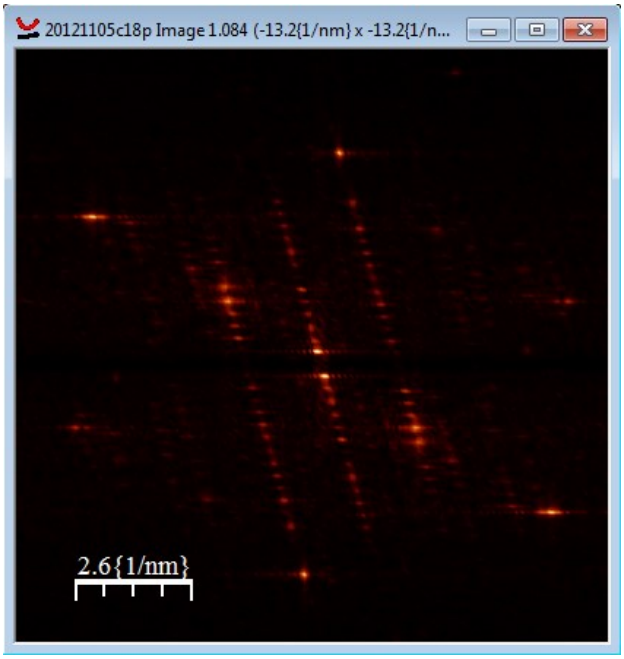

Figure 7. 90° rotated 2D FFT image

Step 5: Redimension the image: 

Due to the cropping, the image in Figure **7** has lower resolution. It is necessary to redimension the image (Figure **8**) to have the same resolution as the original image for the next calibration step (N.B. a typical STM image has a resolution of 512 × 512 points).

To verify the resolution of an image: 1) select the image with a single left click on the image and 2) open the redimension window  . The image resolution can be found in this window.

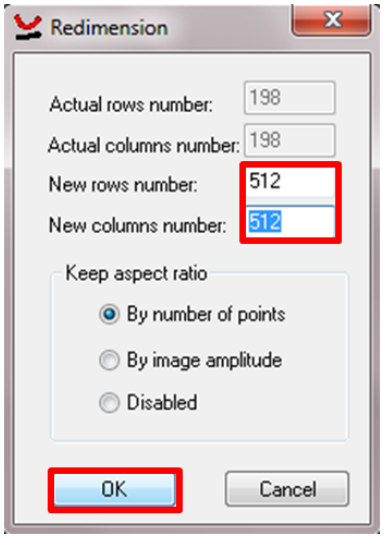

Figure 8. Redimension window

Step 6: Multiple lattice using the **Lattice menu** (Figure **9**): 

Figure 9. Lattice menu

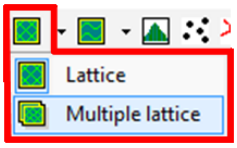

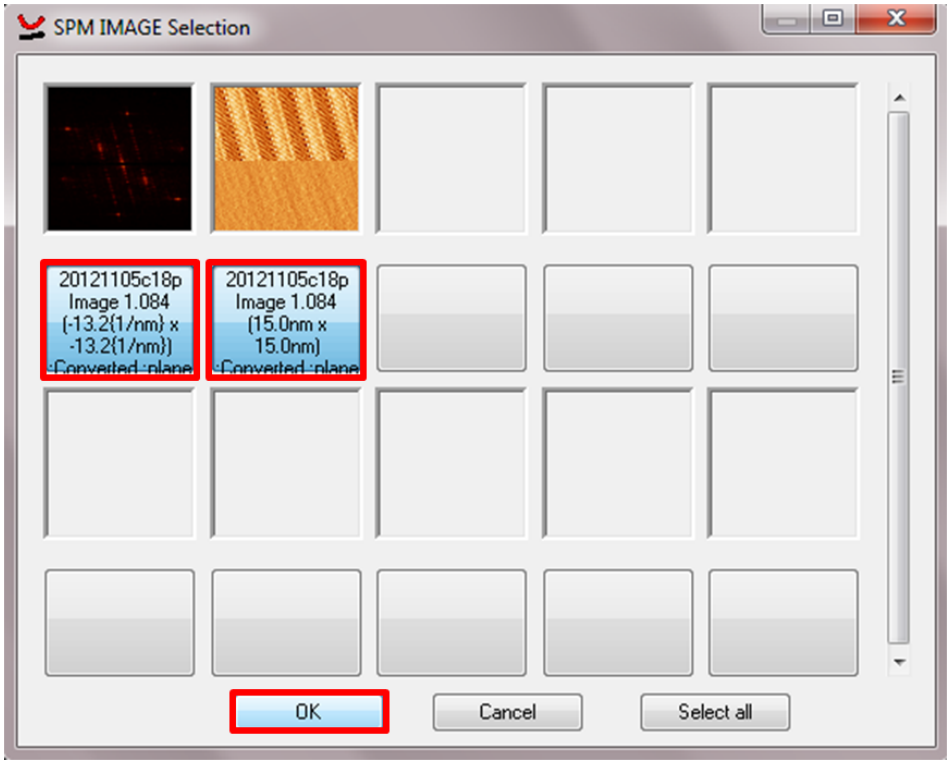

Figure 10. Multiple lattice Image Selection window.

In the resulting **Multiple lattice Image Selection** window (Figure **10**), more images (with the same resolution) would show up if they are opened in the WSxM software. For the purpose of calibration, select the real space image and click on OK to obtain the lattice correction window (Figure **11**).

Notice in the above example, the FFT image should appear on the most left, before the real space image. If not, cancel the selection, and select the FFT image with a single left click and re-open the **Multiple lattice Image Selection** window  .

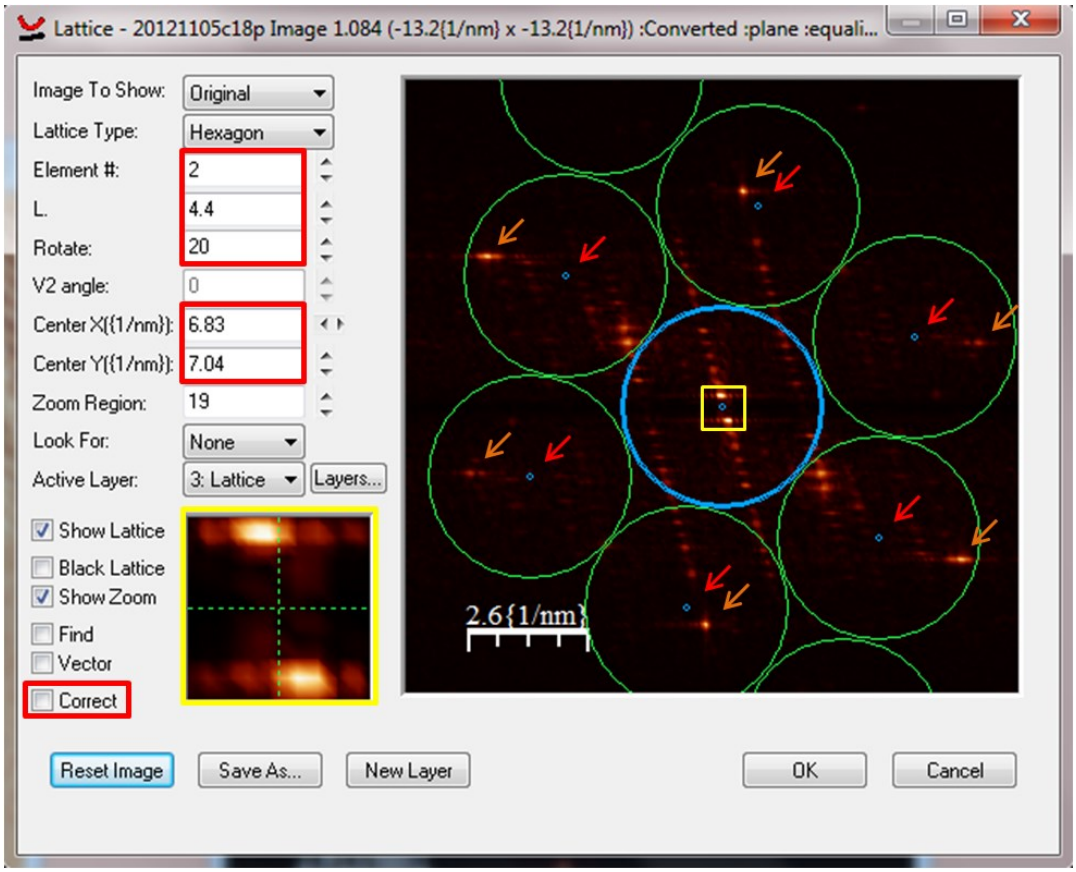

Figure 11. Lattice correction window

In the lattice correction window, center the blue circle using the zoomed-in image on the left (highlighted with a yellow square). Adjust the size of the green circles by changing the 'L' parameter. Note that the distance from the center of the blue circle to the centers of the green circles, highlighted with red arrows, should be shorter than the distance to the six HOPG orange spots, highlighted with orange arrows, to prevent cropping of the real space image) Rotate the position of green circles by changing 'rotate' parameter, so that they are as close to the orange spots as possible. Check the **Correct** box.

Click on one of the six HOPG bright orange spots followed by clicking on the nearest blue spot. Repeat this for the remaining five HOPG spots. Right click the mouse. (The

procedure can be repeated by clicking on **Correct** box again or one can start over by clicking on **Reset Image**)

After correction the window should look like Figure **12** and the corrected SAM image will appear as shown in Figure **13**.

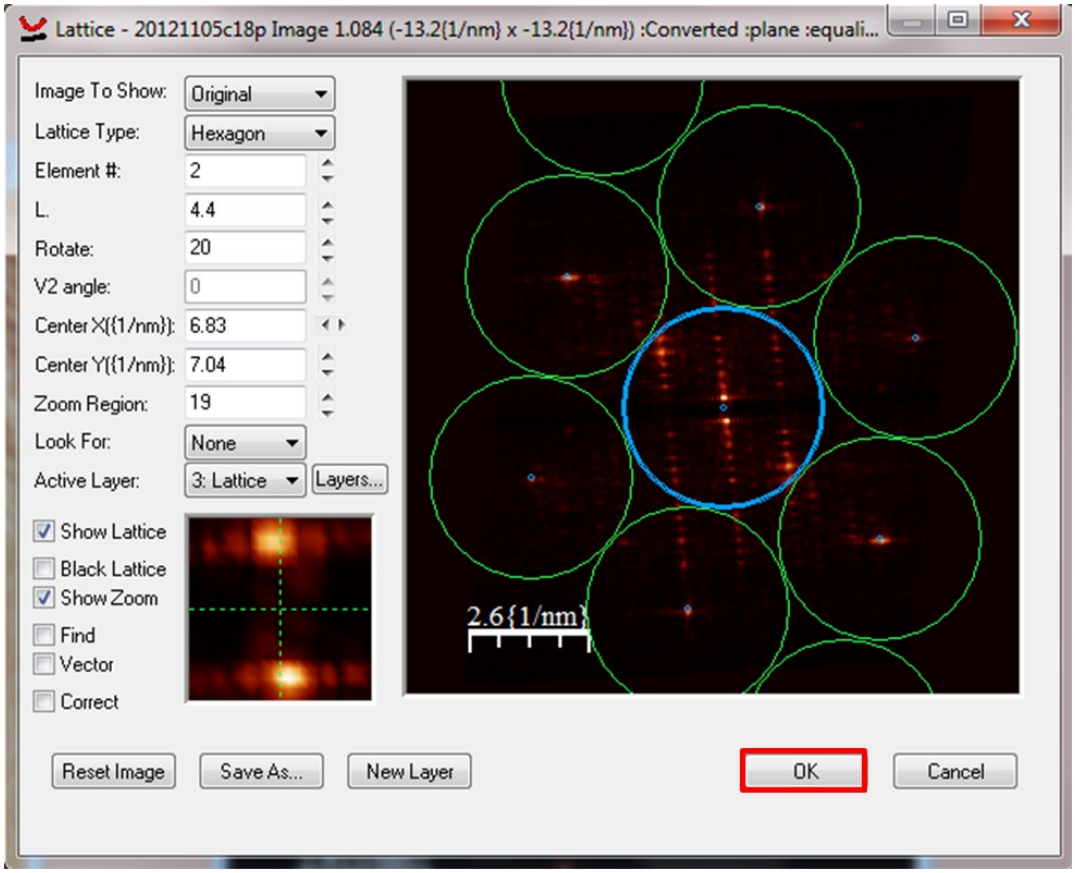

Figure 12. Corrected lattice window

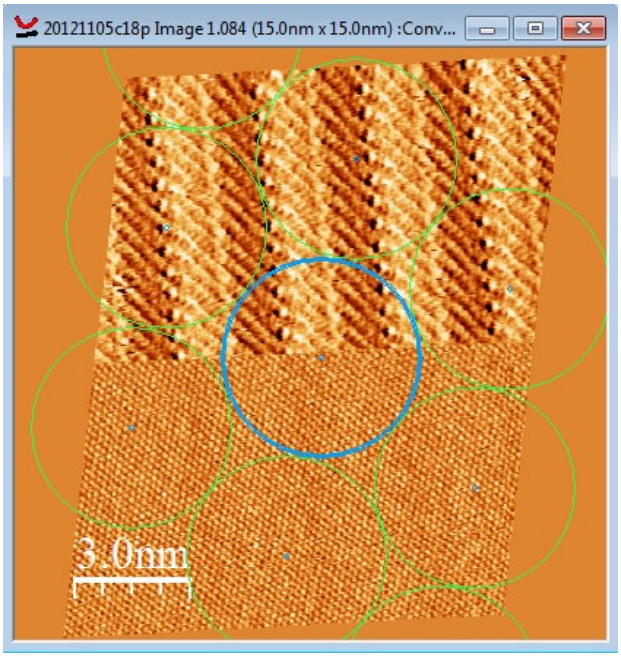

Figure 13. Lattice corrected half-half image

Step 7. 2D FFT the lattice corrected half-half image: 

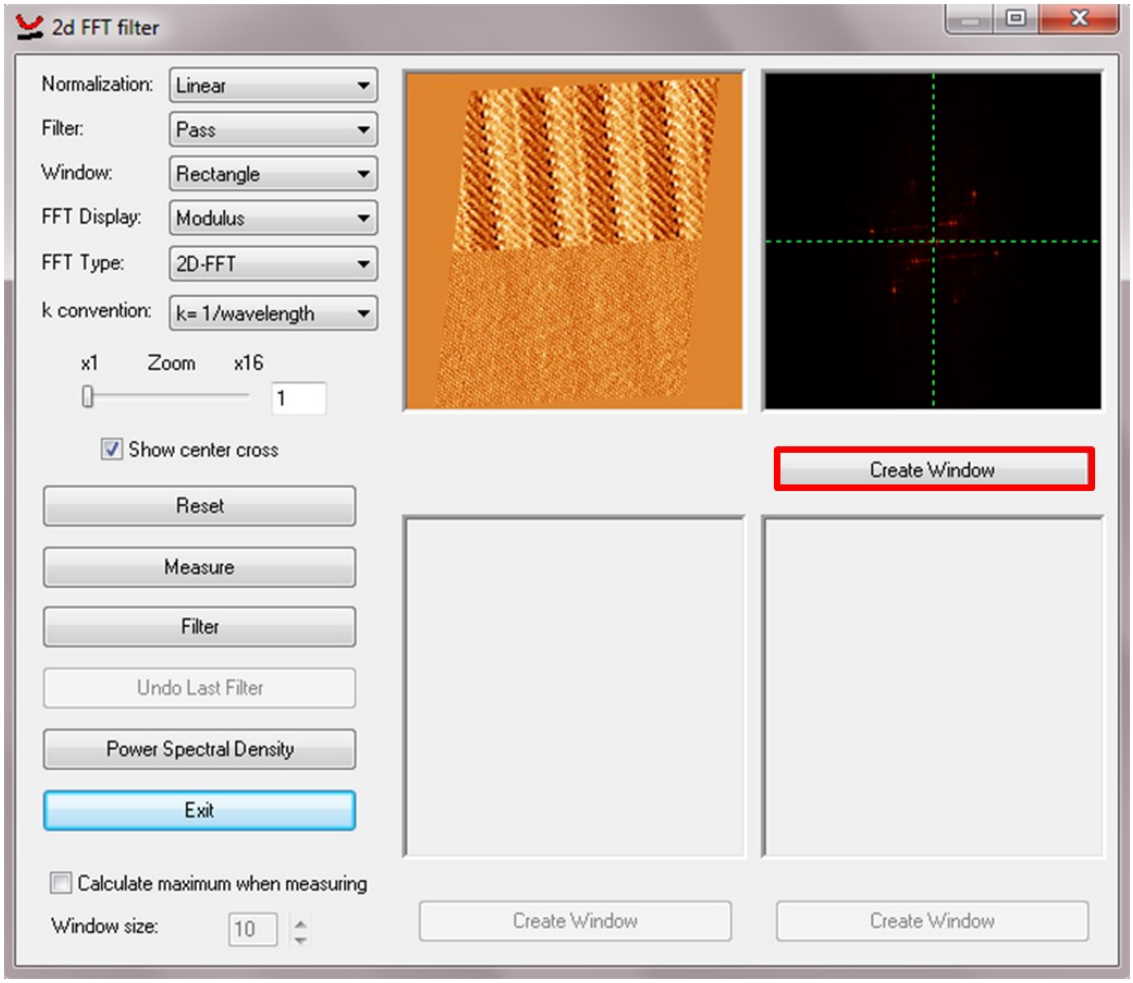

Figure 14. 2D FFT filter window of lattice corrected half-half image.

Click on **Create Window** in Figure **14**. A 2D FFT image of the half-half image should look like Figure **15**.

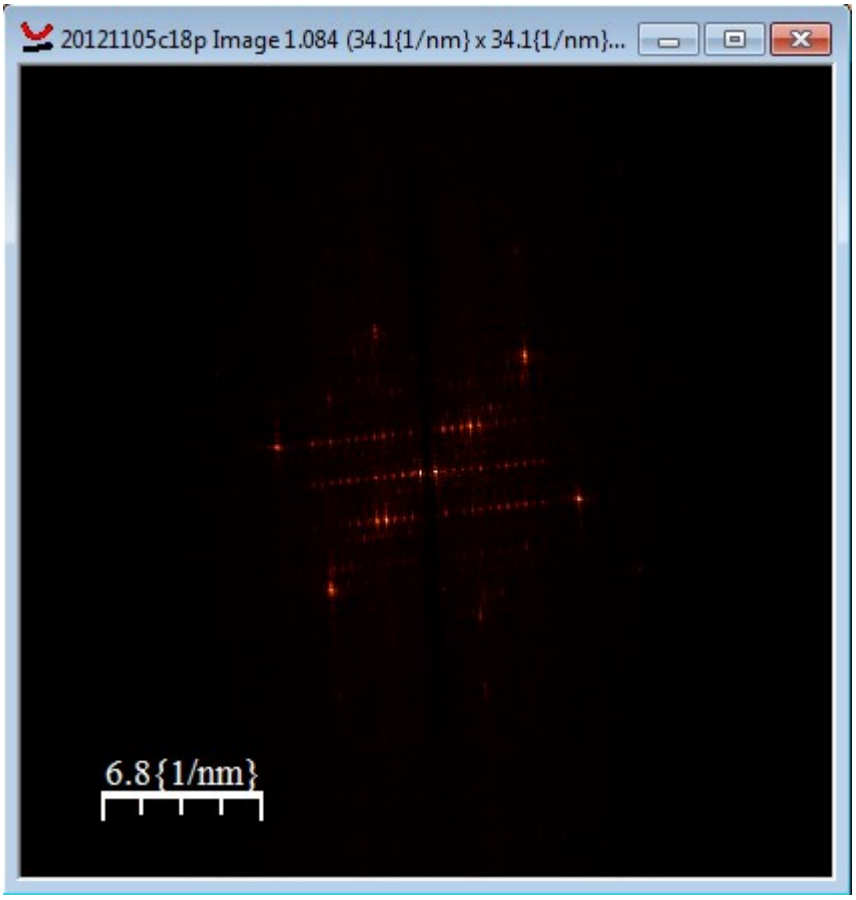

Figure 15. 2D FFT image of lattice corrected half-half image.

Step 8: Calculate correction factor 

At this point, the lattice shape of the image has been corrected. The next step is to correct the lattice parameters.

Make a line profile passing through the two HOPG spots the 2D FFT image of the lattice corrected half-half image as shown in Figure **16**. Right click to finish the drawing. The line can be repositioned afterwards as well.

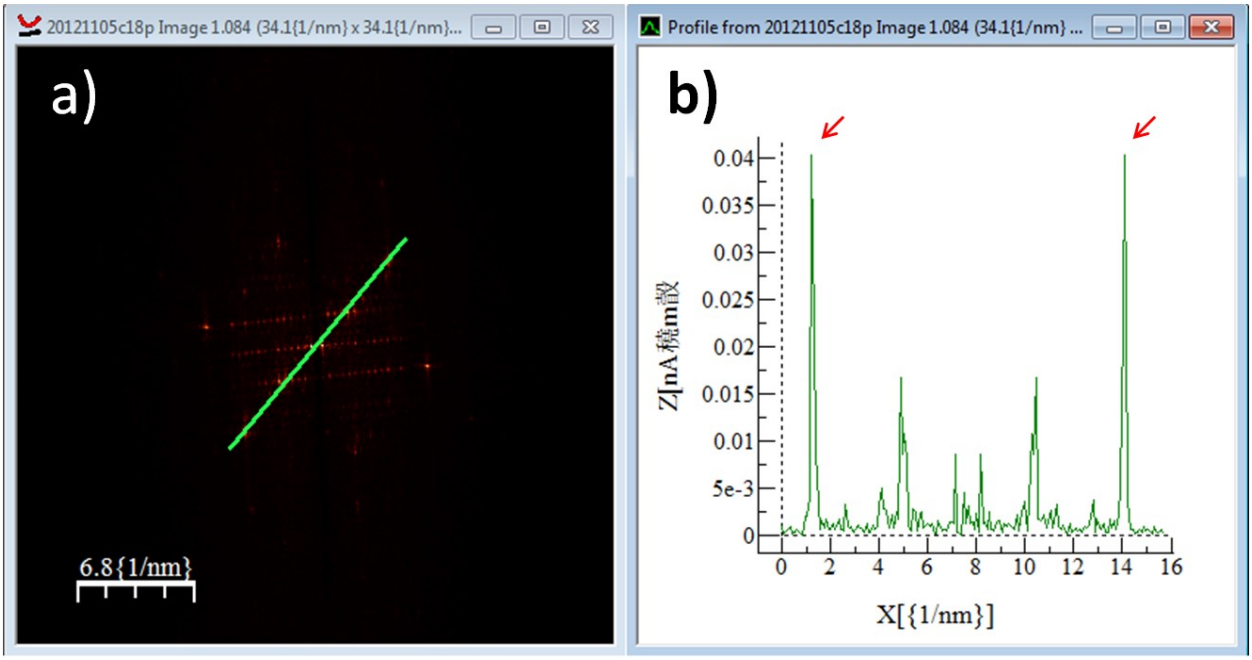

Figure 16. a) Lattices corrected 2D FFT of half-half image, and b) corresponding line profile

Measure the distance between two HOPG spots: 

Place the two square boxes directly on top of the two HOPG peaks (Figure **17**).

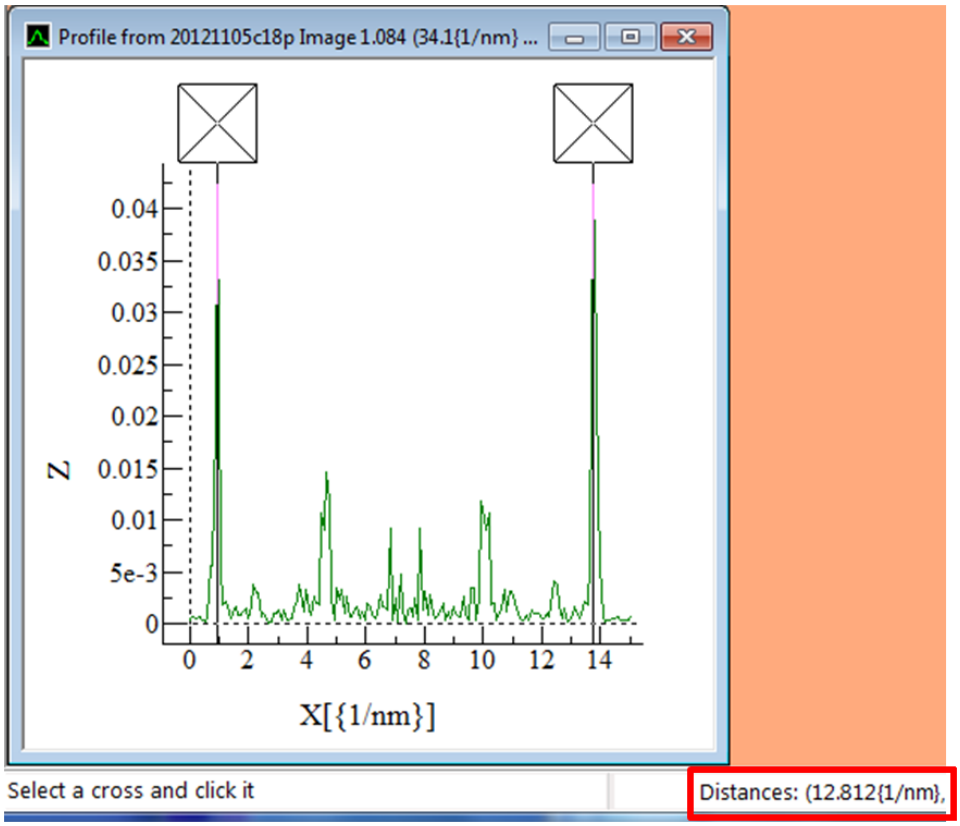

Figure 17. Profile window of 2D FFT image

The distance between the two boxes can be found in the information bar at the bottom of the window (Figure **17**).

Step 9: Resize the image:

Calculate the ratio between actual distance and standard distance of two HOPG spots in FFT image.

$$\text{Ratio} = \frac{12.812}{9.338} = 1.372$$

Type this number into **Factor** box in the Recalibrate Window (Figure **18).**

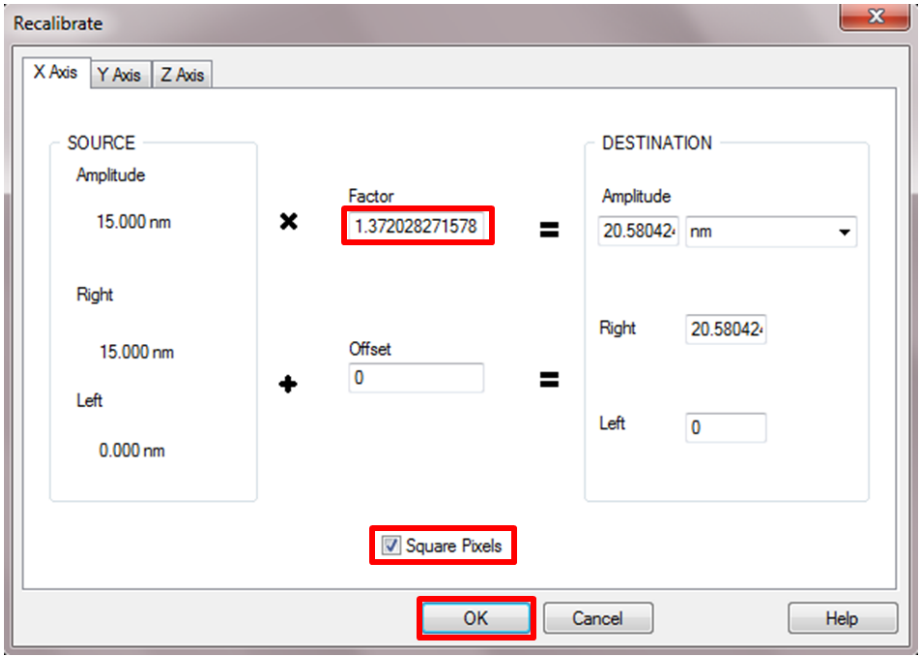

Figure 18. Recalibrate window

In the recalibration window (Figure **18**), click on **Square Pixels** (*i.e.* the y-axis will be multiplied by the same factor as the x-axis). After clicking on OK, a fully calibrated half-half image will look like Figure **19**.

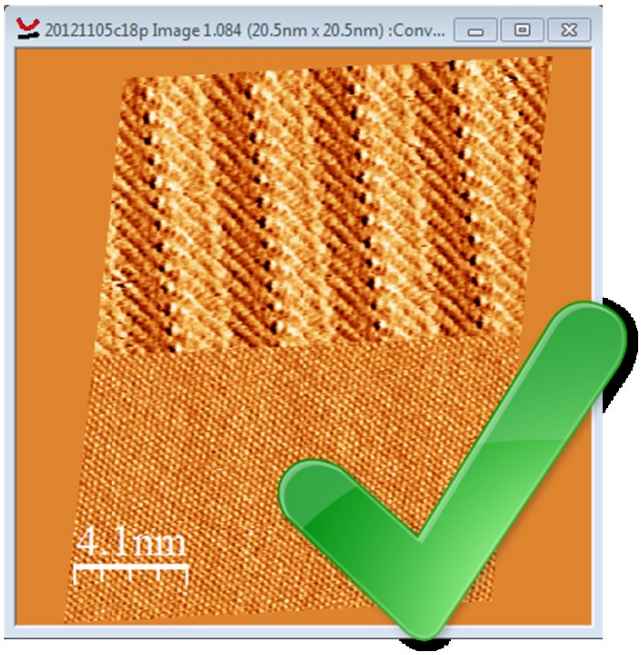

Figure 19. Fully calibrated half-half image.

Method two:

The procedures of method two are very similar to method one. An illustrated procedure of method two is described below. (N.B. refer to method one for detailed repeated steps).

Step 1: Open one HOPG image and one SAM image:

The opened files will look like Figure **20**.

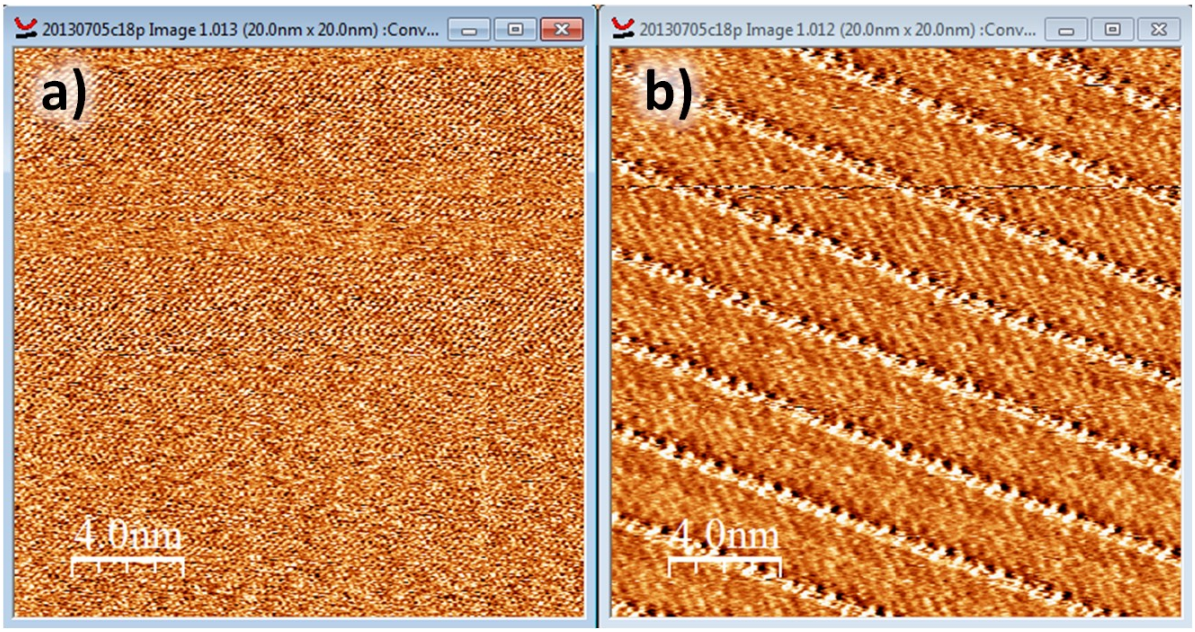

Figure 20. a) HOPG image 20 nm × 20 nm; I_t = 18 pA. V_b = 41 mV. b) STM current image of C18p at the TCB/HOPG interface. 20 nm × 20 nm; I_t = 18 pA. V_b = -300 mV.

Step 2: 2D Fast Fourier transform the HOPG image: 2D FFT 

Only 2D FFT the HOPG image not the SAM image. The 2D FFT image of HOPG should contain 6 bright spots (Figure **21**).

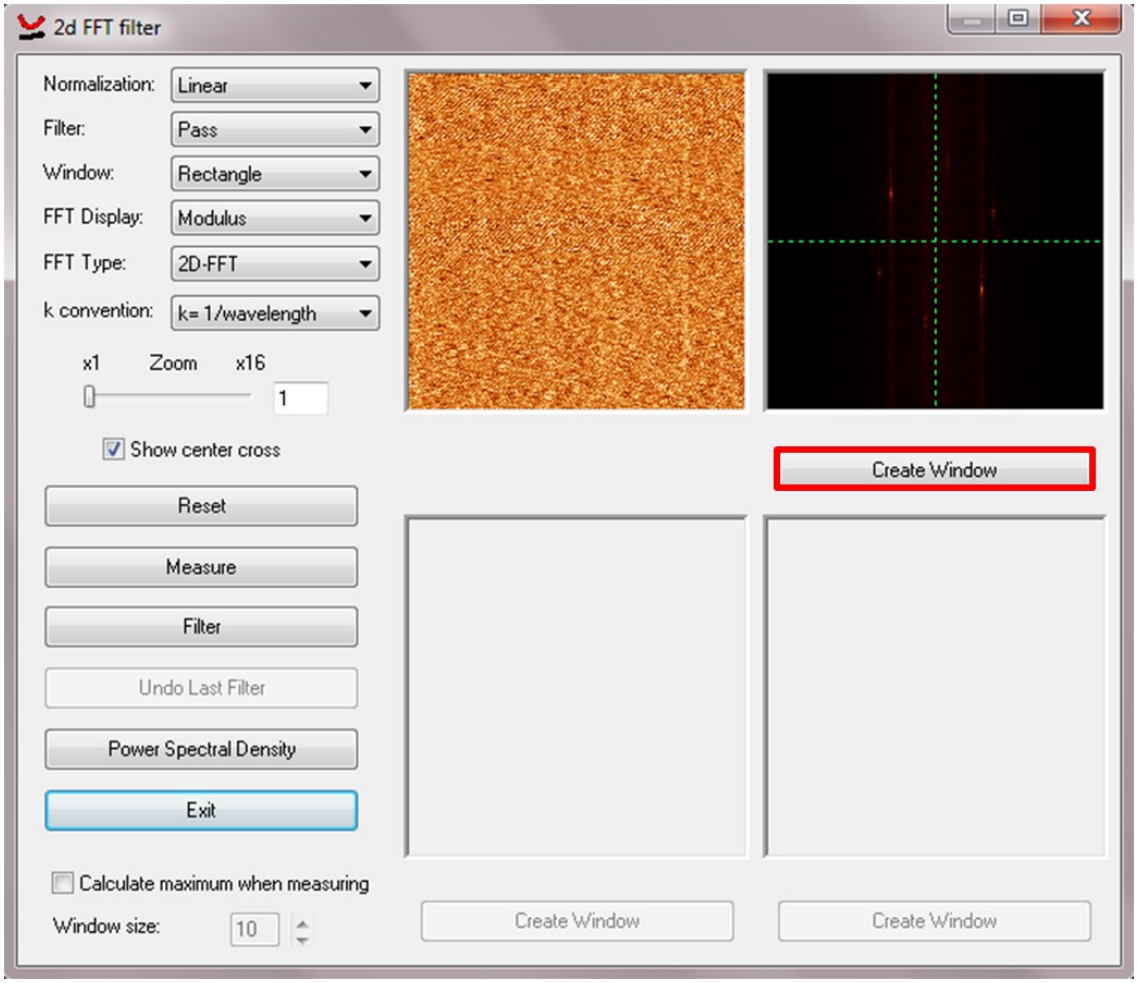

Figure 21. 2D FFT filter window for HOPG image

Step 3: Zoom in: 

Press Shift to draw a square, by holding left mouse key, which just fit the six HOPG spots.

Step 4: Rotate 90°: 

Step 5: Redimension the image: 

If the original image is 512 × 512 by points, redimension the zoomed in imaged to the same resolution.

Step 6: Multiple lattice: 

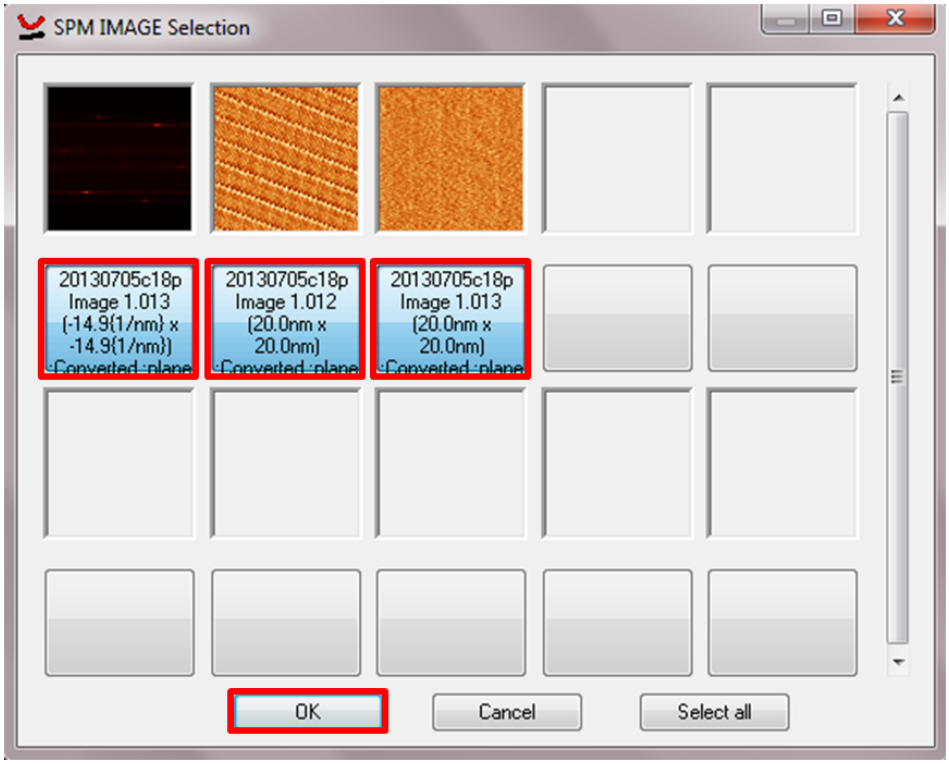

Figure 22. Multiple lattice image selection window

The 2D FFT image of HOPG should appear in the first image window (Figure **22**). Select both the SAM image and the HOPG image.

Calibrate the shape of the six HOPG spots as described in step 6 of method one.

Step 7. 2D FFT the lattice corrected HOPG image: 

Step 8: Calculate correction factor: 

Make a line profile passing through the two HOPG spots the 2D FFT image of the lattice corrected HOPG image.

Place the two square boxes right on top of the two HOPG peaks. 

The distance between the two boxes can be found in the information bar at the bottom of the window.

Step 9: Resize the image: 

Calculate the ratio between actual distance and standard distance of two HOPG spots in FFT image (9.338 nm^{-1}).

Ratio = xxx/9.338 = xxx

In the recalibration window, type the ratio in the factor box. Click on square pixels. Click on OK.

Calibration for method two is complete.